creative commons
COMMONS DEED

저작자표시-비영리-변경금지 2.0 대한민국

이용자는 아래의 조건을 따르는 경우에 한하여 자유롭게

- 이 저작물을 복제, 배포, 전송, 전시, 공연 및 방송할 수 있습니다.

다음과 같은 조건을 따라야 합니다:

저작자표시. 귀하는 원저작자를 표시하여야 합니다.

비영리. 귀하는 이 저작물을 영리 목적으로 이용할 수 없습니다.

변경금지. 귀하는 이 저작물을 개작, 변형 또는 가공할 수 없습니다.

- 귀하는, 이 저작물의 재이용이나 배포의 경우, 이 저작물에 적용된 이용허락조건을 명확하게 나타내어야 합니다.
- 저작권자로부터 별도의 허가를 받으면 이러한 조건들은 적용되지 않습니다.

저작권법에 따른 이용자의 권리는 위의 내용에 의하여 영향을 받지 않습니다.

이것은 이용허락규약(Legal Code)을 이해하기 쉽게 요약한 것입니다.

Disclaimer

dCollection

공학박사 학위논문

Development of a multi-scale friction model in consideration of contact pressure, sliding velocity and lubrication

자동차용 판재성형 해석 적용을 위한 다중 스케일 마찰 모델 개발 및 평가

2022 년 2 월

서울대학교 대학원
재료공학부
이 기 정

Development of a multi-scale friction model in consideration of contact pressure, sliding velocity and lubrication

자동차용 판재성형 해석 적용을 위한 다중 스케일 마찰 모델 개발 및 평가

지도 교수 이 명 규

이 논문을 공학박사 학위논문으로 제출함
2022 년 2 월

서울대학교 대학원
재료공학부
이 기 정

이기정의 공학박사 학위논문을 인준함
2022 년 2 월

위 원 장 _____ 한 흥 남 _____ (인)

부위원장 _____ 이 명 규 _____ (인)

위 원 _____ 최 인 석 _____ (인)

위 원 _____ 송 정 한 _____ (인)

위 원 _____ 이 진 우 _____ (인)

Abstract

Sheet metal forming of advanced high strength steels (AHSS) has drawn significant attentions in automotive industry for their improved fuel efficiency by lightweightness and passenger safety by higher strength. However, the manufacturing of automotive parts with the AHSS accompanies inferior springback and formability compared to the conventional lower strength steels, which results in more time consuming trial and error in the tool design stage.

To overcome this challenges in applying the AHSS to the automotive parts, finite element simulations have been commonly used as a numerical tool for predicting springback and formability of sheet metal parts prior to real try-out. Accurate modeling of finite element simulation in sheet metal forming process requires reliable numerical techniques, constitutive models, realistic boundary conditions, etc. Among these, the friction is one of important factors to determine the accuracy of the simulation, but it has been overlooked in most simulations. The frictional behavior in sheet metal forming is known to be very complex and depend on various parameters such as surface roughness, contact pressure, sliding velocity, lubrication condition, etc. However, it is a common practice to use the simplest Coulomb friction law in the finite element modeling.

In the present study, a microscale asperity based friction model is further

modified by imposing new model parameters for satisfying force equilibrium between contact surfaces. In addition, a geometrical shape model of the tool surface is newly proposed to determine the plowing effect of the friction. The tool geometry is modeled based on primary summits in tool height distribution determined by the measured wavelength, rather than the summits dependent on the resolution of surface measurement instrument.

The friction models are required not only in the preceding boundary lubrication condition, but also in the mixed-boundary lubrication condition where sufficient lubrication exists in non-contacting surface valleys. The hydrodynamic friction model uses a load-sharing concept that considers the lubrication area and metal-to-metal contact separately. In this study, the hydrodynamic friction model is combined with the boundary lubrication friction model to account for the friction in the mixed lubrication domain. The lubricant film thickness, calculated as the volume of non-contacting surface valleys, is used to realize the coupling. The film lubrication behavior is implemented by the finite element coding of the Reynolds equation, which enables the calculation of the hydrodynamic pressure.

To validate the boundary lubrication friction model, the calculated friction coefficient and the measured friction coefficient are compared according to the contact pressure under boundary lubrication conditions. Also, the boundary lubrication friction model is verified by the finite element

simulation that is applied to the U-draw/bending process. Finally, the boundary lubrication friction model and the mixed boundary lubrication friction model are applied to the finite element simulation of the newly developed press-forming process, which represents the influence of various variables such as contact pressure, sliding speed and lubrication. The results of the validations show that the developed multi-scale friction models and their implementation can be efficiently used to the sheet metal forming simulations where the frictional behavior is critical for the quality of the automotive parts.

Keywords: Friction model; Asperity based friction; Boundary lubrication; Mixed-boundary lubrication; Contact pressure; Surface roughness; Hydrodynamic friction; Reynolds equation; Sheet metal forming; Finite element simulation

Student number: 2019-37884

Contents

List of Tables

List of Figures

1. Introduction

1.1. Sheet metal forming and deep drawing process

Sheet metal forming is one of the manufacturing methods in which a piece of metal is reshaped by mechanical deformation of materials without the addition or removal of materials. Metal forming has been widely used as one of the important technologies in many manufacturing industries, especially the automotive industry. Deep drawing, one of the sheet metal forming processes, consists of punch, blank, die and sheet metal as shown in Fig. 1-1. In the deep drawing process, the sheet metal is drawn into the forming die by the movement of the punch under the blank holding, and deformed without changing its weight. The total drawing load is determined by the deformation of the sheet metal and the friction between the sheet metal and other forming tools. The quality of the product is judged by the occurrence of defects such as cracks, scratches, and wrinkles. In order to improve the accuracy and quality of products, it is necessary to optimize the sheet metal material properties, mold design, surface roughness, and friction (lubrication). Therefore, this optimization task requires an experienced knowledge of materials and tribology mechanics.

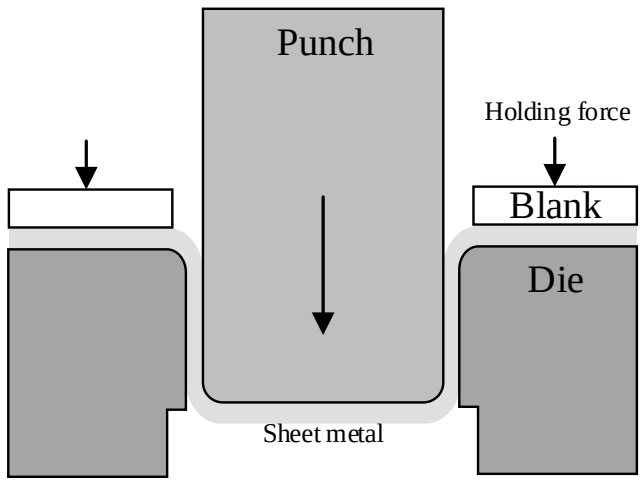

Fig. 1-1. The deep drawing process schematic

1.2. Motivation and objective

Until the 20th century, the manufacturing process was modified through inefficient and expensive trial-and-error to optimize the appropriate product size and to ensure defectless. In recent years, numerical methods such as finite element simulation have been used for efficient optimization of the process. Moreover, the development of algorithms for automatically optimizing new product designs has been proposed [1,2]. To obtain an accurate result from finite element simulation in the metal forming process, the implementation of proper constitutive models and employment of numerical techniques are critical as conducted by numerous researchers [3-6]. In addition, the contact boundary condition such as friction is also an important factor in the finite element simulation of the metal forming process as it changes the stress on the surface of the workpiece [7]. Despite the importance of friction, many

researchers have performed finite element simulation with a constant friction coefficient, based on Coulomb's friction law. However, it is widely known from experimental studies [8-12] that friction coefficient changes with several factors such as surface quality, contact pressure, lubrication condition, temperature, and working environment. Therefore, although a suitable friction coefficient is required in the simulation, it is a challenge to accurately model the friction behavior under complex contact conditions. In addition, the applications of emerging or lightweight materials such as advanced high-strength steels (AHSS), aluminum, and magnesium alloys are known to result in unclear and severe contact conditions due to surface coating and complexity from advanced forming processes [13, 14]. Recently, the importance of friction modeling increases due to the novel stamping and joining processes which utilize the direct frictional behavior [15]. Nevertheless, friction modeling has been implemented in various research areas to consider the frictional behavior that varies depending on the contact conditions in the cold or hot metal forming processes [16, 17]. These studies can be categorized into either experimental studies [18-21] or theoretical studies [22-24] depending on their approaches to construct friction models.

In the experimental studies, the friction coefficients measured by actual friction tests under various contact conditions are analyzed either directly or by constructing an empirical model for finite element simulation. These

approaches not only make it difficult to build the empirical model that covers a full range of contact conditions but also require various friction experiments under different contact conditions [25]. In the theoretical studies, friction models were constructed based on the contact mechanisms between workpieces and tool surfaces. In this approach, friction models could be established with assumptions based on the understanding of the friction and contact mechanism. For the objective of this thesis, to propose a reliable friction model, new assumptions are added to the friction model based on the overview of the previous friction models. In addition to the friction model describing the frictional behavior in boundary lubrication, one of the major lubrication regimes in sheet metal forming, the variation in frictional behavior is considered in the mixed-boundary lubrication conditions when the amount of lubrication is sufficient. The friction model is verified through comparative analysis according to the friction model in the FE simulation of real sheet material forming.

1.3. Literature review

The effect of lubrication on friction reduction is well known historically. To specify this, Stribeck [26] and Hersey [27, 28] experimentally measured the change in friction coefficient according to lubricant viscosity, contact load, and sliding speed, and presented the so-called Stribeck curve. The curves represent three regions of the coefficient of friction according to the lubrication regime, as shown in Fig.1-2. In boundary lubrication conditions in which metal and metal are in direct contact, high friction occurs due to surface contact irregularities. Second, friction occurs due to asperities and lubrication under mixed-boundary lubrication conditions. Finally, in elastohydrodynamic (or hydrodynamic) lubrication regimes where there is no metal-to-metal contact, the hydrodynamic flow of the lubricant primarily contributes to friction. In the actual metal forming process, the main lubrication conditions are known as boundary lubrication and mixed-boundary lubrication, and the friction model of mixed-boundary lubrication requires additional consideration of the lubrication mechanism. Therefore, this section further describes friction models based on boundary and mixed-boundary lubrication conditions.

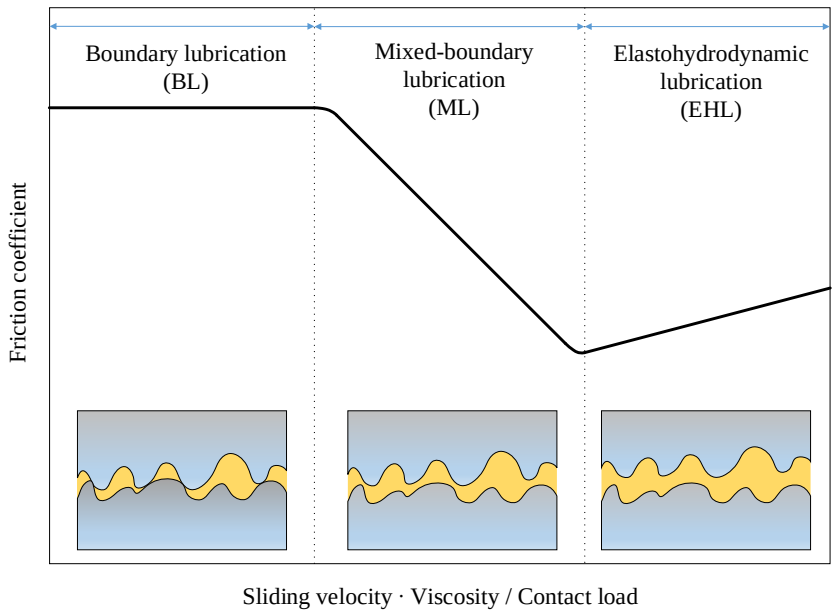

Fig. 1-2. Stribeck curve

1.3.1. Friction modeling on the boundary lubrication condition

Hardy [29], who distinguished the actual contact area from the nominal contact area, suggested adhesion, one of the major friction factors between metals. Since then, adhesion theory has been independently studied by several researchers [30-32]. Bowden and Tabor [33-35] further considered adhesion theory, as well as the plowing (ploughing) in which the roughness of a hard tool penetrates the surface of a soft workpiece due to differences of hardness during sheet metal forming (Fig. 1-3). Assuming that the plowing effect and the adhesion effect are independent, the friction force is independently proposed as the sum of the two effects as follows:

$$F = sA_R + p_0 A' = s \cdot \frac{F_N}{p_0} + p_0 A' \qquad (1.1)$$

Adhesion: $s \cdot \frac{F_N}{p_0}$; Plowing: $p_0 A'$

$$\mu = \frac{F}{F_N} = \frac{s}{p} + \frac{A' p}{F_N} (F_N = pA_R) \qquad (1.2)$$

Adhesion: $\frac{s}{p}$; Plowing: $\frac{A' p}{F_N}$

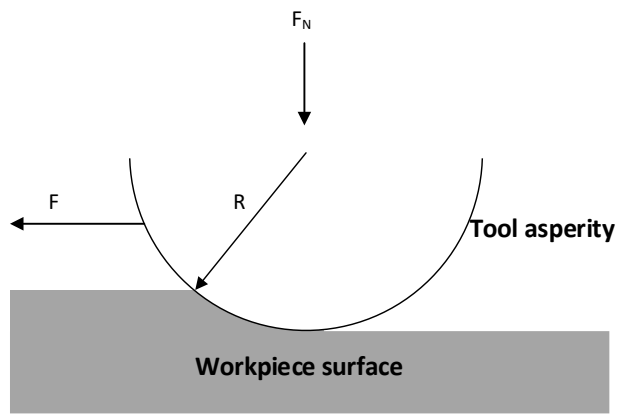

Fig. 1-3. Penetration of hemispherical hard tools while plowing soft workpieces

Since the frictional force can be expressed as the shear stress of an adhesive metal junctions in previous studies [33, 34], Green [36, 37] studied how the deformation and stress field of the junction are determined according to the junction shape. The strength of the junction, the adhesive force, and the relative movement of two metal bodies. Fig. 1-4 shows the slip-line field analysis according to the junction and adhesive force according to the sliding condition.

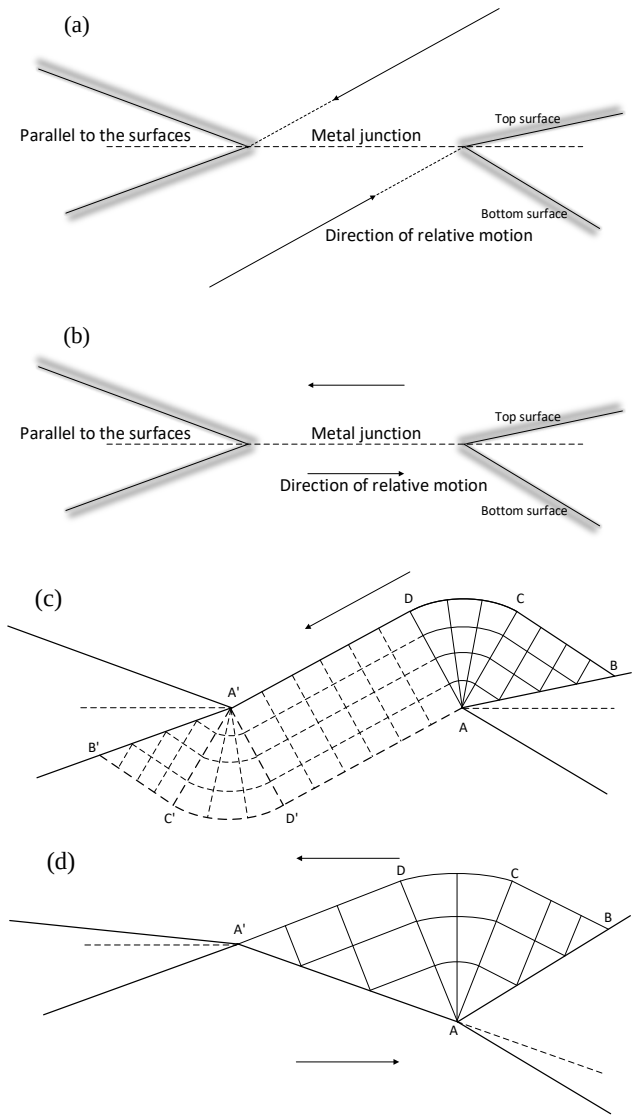

Fig. 1-4. Figures of junctions (a) at the start of sliding, (b) during steady sliding; Slip line fields for (c)a strong junction and (d) a weak junctions

In advanced adhesion models [38], a junction growth theory was proposed that the real contact area increases due to the shear stress on the contact between the asperities during sliding. In this junction growth theory, when additional shear stress is applied to an already plastically deformed contact

asperity, as shown in Fig. 1-5, the actual contact increases with more plastic flow to maintain the von-Mises stress. This junction growth phenomenon was observed on clean surfaces [39-42] as well as in lubricated conditions [43]. As shown in Fig. 1-6, Shaw et al. [44] classified friction and contact behavior into three regions according to the contact pressure and proposed a linear increase in the actual contact area at low pressures and a smooth transition (region 2) between the full contact area at high pressures.

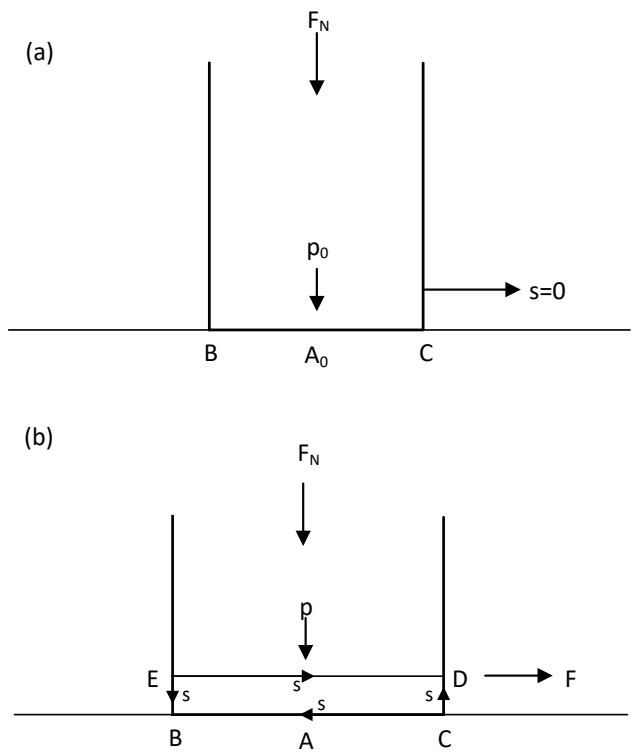

Fig. 1-5. unction growth due to shear stress in a 2D model. Comparison of (a) contact with only normal force W and (b) contact after application of shear force F due to sliding

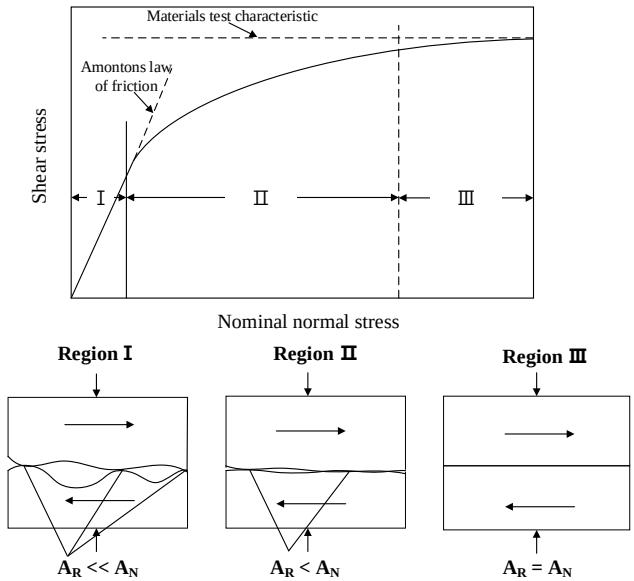

Fig. 1-6. The three regions of friction according to normal contact stress

A new statistical contact model was first proposed to determine the actual contact area, which has a significant impact on friction [11]. In most statistical contact models [45-47], such as Greenwood and Williamson's models, the tool surface is considered a smooth rigid body because it is coarser and smoother than the workpiece. Also, the surface of the work is modeled as a group of spherical asperities with a constant radius, as shown in Fig. 1-7, and follows a Gaussian height distribution function. According to Hertz's law [48, 49], the deformation of spherical asperities during contact is assumed to be elastic, and the actual contact ratio and nominal pressure are proposed in equilibrium.

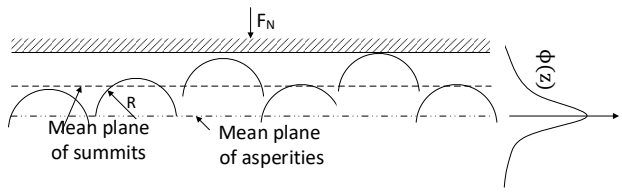

Fig. 1-7. Workpiece surface is modeled by spherical asperities

The Greenwood-Williamson's contact model includes variations of the asperity shape [45], a contact between the two rough surfaces [50], a difference in the radius of curvature of the asperity [51], an ellipsoidal parabolic asperity [52], and an anisotropic surface. [53], and elasto-plastic deformation of asperities [54].

Hisakado [55] modeled friction by determining the conical and pyramidal shapes of asperity, and modeled the plowing effect on friction based on the relative roughness and hardness differences between the two metal surfaces. However, this modeling did not take into account the interaction between the asperities, assuming that each asperity deforms independently.

Nayak [56, 57], who conducted theoretical models of surface roughness, described rough surfaces with surface characteristics such as normal density, normal height, and normal curvature, and improved the accuracy of these surface characteristics. Then, as they approached the two surfaces, the number of contacts that made full plastic contact was investigated [58]. In a previous study [11,52], the contact points are independent of each other, so the number of contact points increases continuously as the two surfaces approach each

other. Therefore, in a third study by Nayak [58], the formation and number of contact patches were studied, taking into account the contact merging.

Pullen and Williamson [59] extended the statistical contact model to explain the interaction between asperities due to plastic deformation and volume conservation. In contrast to the classical approach of plastic contact, where the actual contact area ignores the interaction and is linear with the nominal pressure [32], Pullen experimented with the non-linearity between the actual contact area and the nominal pressure. In addition, the analytical relationship between the actual contact area and the nominal pressure can be derived as follows:

$$\frac{p_{nom}}{H} = \frac{\alpha}{1-\alpha} \tag{1.3}$$

Challen and Oxley [22, 60] considered the integrated effect of the plowing and the adhesion in the friction model, unlike the previous model [34, 38]. As shown in Fig. 1-8, Challen and Oxley [22, 60] suggested a friction mechanism through slip-line analysis in three deformation modes (plowing, wear, and cut) determined by the attack angle θ and the friction coefficient of the interfacial film fc (fc = τ/k, where τ is the shear strength of the boundary film and k is the shear strength of the material, $0 \leq fc \leq 1$). The friction mechanism of the plowing mode occurring at low θ was described only as plastic deformation of the smooth workpiece without surface removal. The friction mechanism

was further considered for the effect of surface removal by chipping and wear at high θ (i.e., cutting and wear mode). Because of the different friction mechanisms, Challen and Oxley [22, 60] derived different friction coefficient in each mode as follows:

$$\mu_{cutting} = \tan\left(\theta - \frac{1}{4}\pi + \frac{1}{2}\arccos\left(f_c\right)\right) \tag{1.4}$$

$$\mu_{plowing} = \frac{A_1 \sin\theta + \cos\left(\arccos\left(f_c - \theta\right)\right)}{A_1 \sin\theta + \sin\left(\arccos\left(f_c - \theta\right)\right)} \tag{1.5}$$

with:

$$A_1 = 1 + \frac{\pi}{2} + \arccos\left(f_c\right) - 2\theta - \arcsin\left(\frac{\sin\theta}{\left(1 - f_c\right)^{1/2}}\right) \tag{1.6}$$

$$\mu_{wear} = \frac{\left\{1 - 2\sin A_2 + \left(1 - f_c^{\,2}\right)^{1/2}\right\}\sin\theta + f_c\cos\theta}{\left\{1 - 2\sin A_2 + \left(1 - f_c^{\,2}\right)^{1/2}\right\}\cos\theta + f_c\sin\theta} \tag{1.7}$$

with:

$$A_2 = 1 - \frac{\pi}{4} + \frac{1}{2}\arccos\left(f_c\right) + \arcsin\left(\frac{\sin\theta}{\left(1 - f_c\right)^{1/2}}\right) \tag{1.8}$$

Fig. 1-9, the so-called wear-mode diagram, shows the friction mode determined by the attack angle θ and the shear modulus fc. This model has been validated by many researchers [22, 61] with measurements of horizontal

and vertical forces by indenting and sliding wedge-shaped tools.

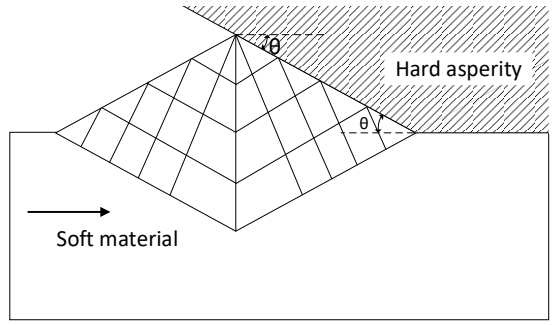

(a) Plowing mode

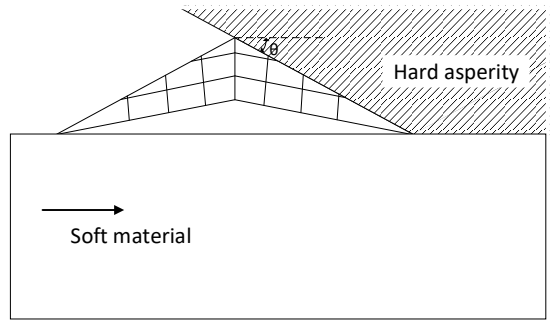

(b) Wear mode

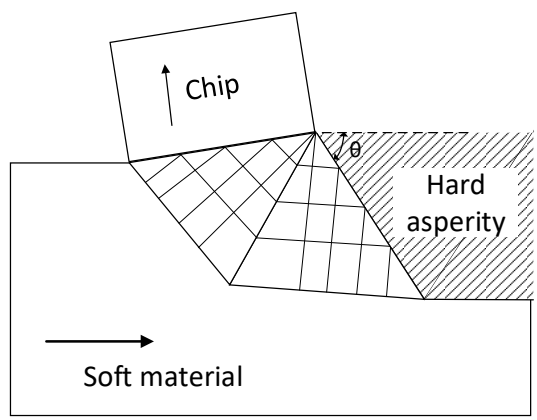

(c) Cutting mode

Fig. 1-8. Different modes of friction mechanism: (a) plowing mode, (b) wear mode, (c) cutting mode.

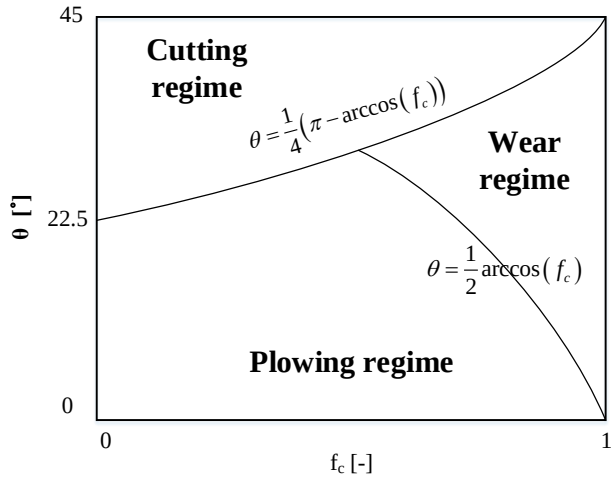

Fig. 1-9. Wear-mode diagram.

Greenwood and Rowe [62] and Fog [63] empirically showed an increase in the actual contact area, a major factor influencing friction, due to the unavoidable bulk deformation in sheet metal forming. The analysis model considering the effect of bulk plasticity was based on the wedge-shaped asperity shape as shown in Fig. 1-10 [64, 65]. Wilson and Shen [64] assumed the plane strain condition in the x-direction(ε_{xx}=0) and the plane stress condition in the z-direction(σ_{zz}=0), and used an upper-bound analysis for asperity flattening in the presence of a unidirectional strain in the z-direction. Contrary to the assumptions of Wilson and Shen [64], Sutcliffe [65] assumed that the asperities were in plane strain mode in the z-direction (ε_{zz}=0) and applied the silp-line theory for surface indentation. They found a decrease in effective hardness during bulk deformation, which explained that the actual contact area increased during bulk deformation.

Wilson and Shen [64] measured the asperity flatness similar to that observed by Atala and Rowe [66] in the rotation experiment and compared it with the prediction by the verification model. In addition, these models were later validated based on finite element analysis by several researchers [67-69]. Based on previous studies [64], Wilson [70] considered the effects of steady and unsteady conditions, surface roughness of workpiece and tool, sliding speed, contact pressure, and strain rate.

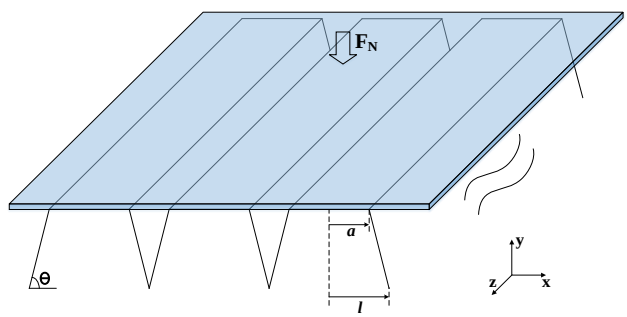

Fig. 1-10. Deformation of wedge-shape asperities for contact and bulk strain conditions.

Zhao et al. [71] compensated for several shortcomings of the elastic–plastic contact model previously proposed by Chang et al. [54]. The first is that, unlike the analysis of Johnson [72], the contact asperity does not transition from elastic deformation to plastic deformation and only one deformation state (elastic or plastic) is possible. Another one due to the above shortcomings is that the contact load is not continuous at the critical point (the initial yielding of the asperity). As a final drawback, unlike the experimental

results [73], the actual contact area is calculated to be smaller in the elastic-plastic contact than in the elastic contact at the same contact pressure. As the contact model that compensates for these shortcomings, the actual contact area is proposed in the plastic transition area between the elastic contact area and the plastic contact area as shown in Fig. 1-11. Later, Zhao et al. [71] The model was extended to the situation of elliptical asperity [74] and guaranteed the best results in real contact area predictions [75, 76].

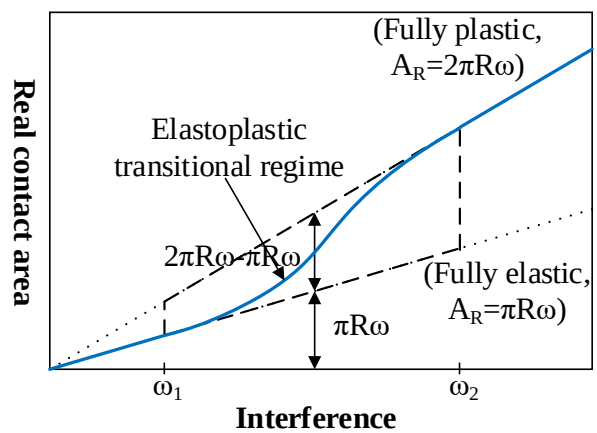

Fig. 1-11. Real contact area in elastoplastic transitional regime

Westeneng [77] presented a multi-scale friction model during the sheet metal forming process under dry conditions, divided into two types: a contact model and a friction model. In contrast to the spherical previous statistical contact model [11], the statistical representation of the rough workpiece surface was modeled as a group of bars as shown in Fig. 1-12. In this contact model, Westeneng proposed a contact mechanism that satisfies both the laws

of conservation of energy and volume to obtain the actual contact area. The law of conservation of energy states that the external energy is equal to the sum of the energy required internally when some of the asperities are pressed and the others are raised. The law of conservation of volume means that the total volume of indented asperities equals the total volume of raised asperities. In the model, the deformation behavior of the workpiece surface was assumed to be plastic. The actual contact area obtained from the contact model was the dominant factor in the friction model. Then, as shown in Fig. 1-13, the total frictional force on the tool surface modeled by spherical asperities with a constant radius was proposed as the sum of each frictional force [60] generated by combining the adhesion effect and the plow effect at each asperity. In addition, the increase in the actual contact area and the change in the friction coefficient due to bulk deformation were modeled by Westeneng.

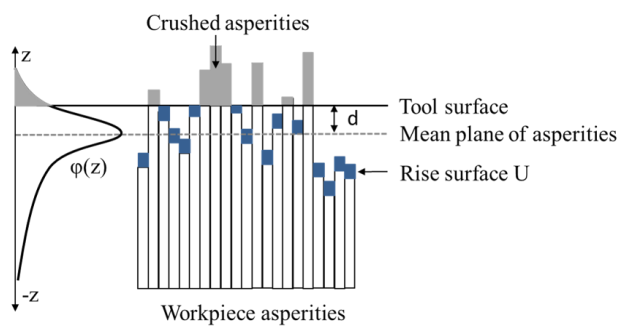

Fig. 1-12. Flattening of rough workpiece surface modeled as group of bars with different height

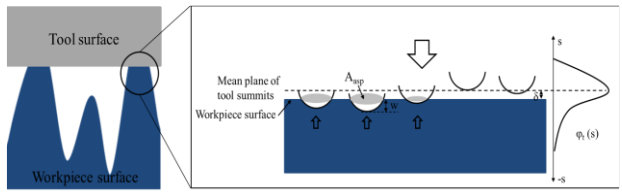

Fig. 1-13. Tool surface modeled as spherical summits of constant radius in friction model by Westeneng [74]

Ma et al. [78] proposed a friction model that considers summits join (contact merging) as shown in Fig. 1-14 in full plastic contact as the contact pressure increases. Because the geometry of the asperities (eg, spherical) changes due to many summits bonding at high contact pressures, the friction was calculated by forming the tool asperity into an elliptical paraboloid with the size and height of the contact patch (Fig. 1-15). The coefficient of friction of the single contact patch followed the Challen and Oxley [60] model.

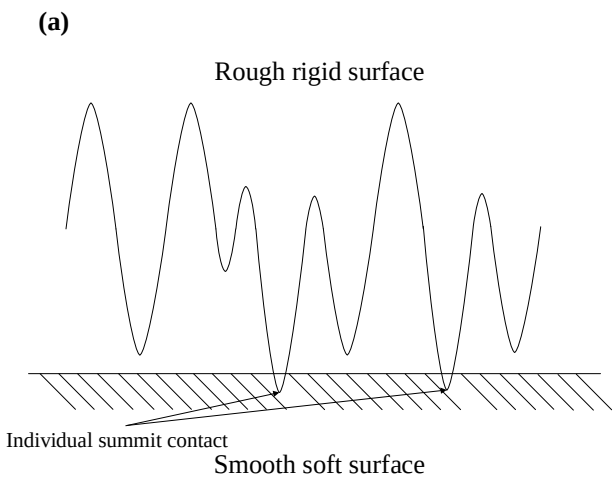

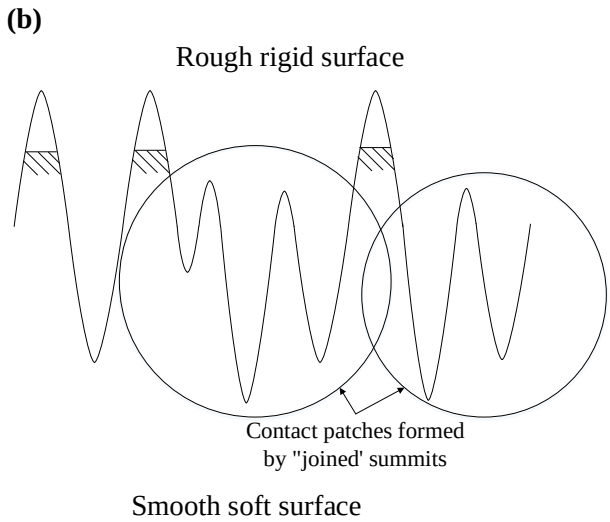

Fig. 1-14. Schematic view of (a) contact summits at low contact pressure and (b) contact patches at high contact pressure

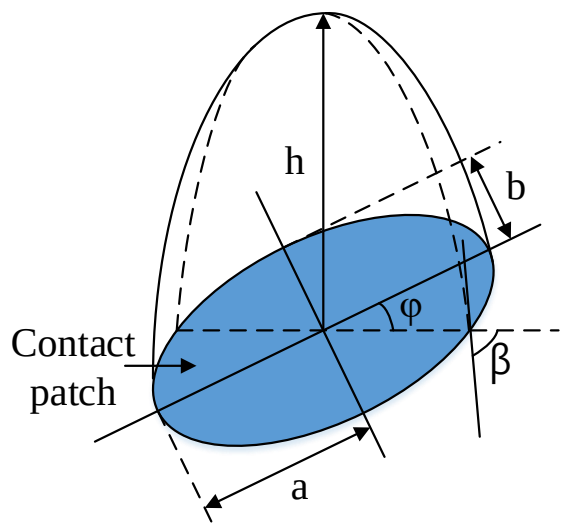

Fig. 1-15. Geometrical parameters of elliptical paraboloid from Ma et al.

Hol et al. [79] provided the numerical framework for validating Westeneng's contact model and applying it to finite element simulations of

sheet metal forming processes. Hol et al. [80] proposed a newly developed multi-scale friction model applying a deterministic approach [78] and contact mechanism [78] that takes into account the increase in the actual contact area due to shear stress between the asperities and growth of the metal joint during sliding [38]. To validate the newly developed friction model, the actual contact area and coefficient of friction were experimentally obtained, and the reaction forces measured during two different sheet metal forming processes (simple U-shape and cross-shape) were also compared to those in finite element simulations. Karupannasamy et al. [81] proposed the deterministic contact model that roughly modeled the surface of a work piece and tool, based on the work of Ma et al. and Masen et al. [82]. After that, the friction model added mixed modes of asperity deformation, and it was verified as results of a rotational friction test under multiple loading conditions [83].

1.3.2. Friction modeling on the mixed-boundary lubrication condition

Lubrication changes the physical or chemical bonds that control the friction between two surfaces in the metal forming process. In addition, the hydrodynamic pressure of the lubricant under the contact pressure and sliding of the workpiece suppresses the actual contact area and the development of metal-to-metal contact. Therefore, lubrication can reduce friction and wear between the contact surfaces during the metal forming process and improve the formability and surface quality of the product.

In mixed boundary lubrication conditions, friction modeling relies heavily on lubrication as well as the friction mechanism between the asperities. Reynolds equation [84], a partial differential equation controlling the hydrodynamic pressure distribution of thin film lubricants, is essential to accommodate the lubrication behavior in friction modeling.

Basic mechanics of fluid film lubrication

The Reynolds equation was derived from the Navier-Stoke equation by assuming zero-slip at the fluid-solid interfaces and Newtonian thin-film fluid. The equation can be written as follows:

$$\underbrace{\nabla\bullet\left(\frac{h^3}{12\eta}\nabla p_{\text{lub}}\right)}_{Poiseuille}=\underbrace{\frac{\left(v_1+v_2\right)}{2}\nabla\bullet\left(\rho h\right)}_{Couette}+\underbrace{\frac{\partial h}{\partial t}}_{Squeeze} \tag{1.9}$$

with $\nabla=\left(\frac{\partial}{\partial x},\frac{\partial}{\partial y}\right)$

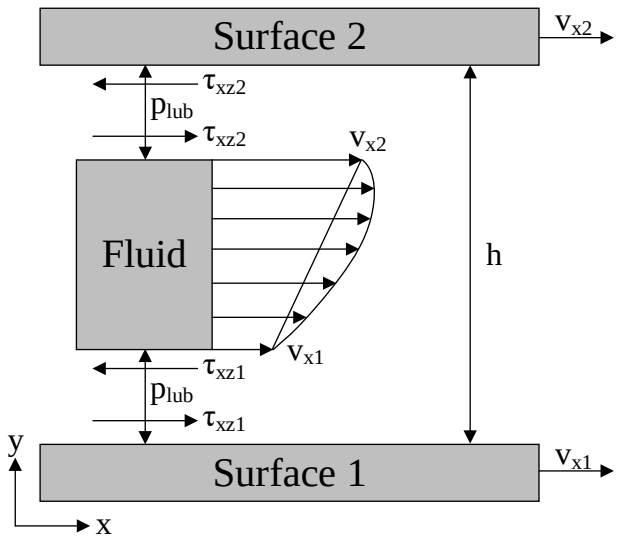

Fig. 1-16. Schematic view of hydrodynamic flow.

Fig. 1-16 shows a schematic view of hydrodynamic equilibrium. The Reynolds equation is represented by describing the Poiseuille flow via a pressure gradient, the Couette flow as the sliding velocity of surfaces, and the squeeze flow due to the change in film thickness. Patir and Cheng [85, 86] derived the averaged Reynolds equation by associating flow factors that consider the roughness of the surfaces. The averaged Reynolds equation is shown as follows:

$$\nabla\bullet\left(\frac{h^3}{12\eta}\boldsymbol{\Phi}_{\mathbf{P}}\nabla p_{\text{lub}}\right)=\frac{(v_1+v_2)}{2}\nabla\bullet\left((\rho h)+\frac{S_q}{2}(v_1-v_2)\bullet\boldsymbol{\Phi}_{\mathbf{S}}\right)+\frac{\partial h}{\partial t} \tag{1.10}$$

Where $\boldsymbol{\Phi}_{\mathbf{P}}$ compensates for Poiseuille flow due to surface roughness, and $\boldsymbol{\Phi}_{\mathbf{S}}$ represents additional flow due to surface roughness. The flow factors are

calculated by numerical analysis of a flow model problem which can be described as the one-directional flow between rough surfaces as shown in Fig. 1-17. In smooth surfaces condition, $\mathbf{\Phi_P}$ converges to $\mathbf{I}$ and $\mathbf{\Phi_S}$ equals 0, thus the average Reynolds equation is converted to the standard Reynolds equation. In addition, Patir and Cheng [85, 86] investigated the variation of fluid flow due to the directional characteristics of the surface roughness. The surface orientation characteristic was represented as γ, which is the ratio of x and y correction lengths as shown:

$$\gamma = \frac{\lambda_{0.5x}}{\lambda_{0.5y}} \tag{1.11}$$

where $\lambda_{0.5x}$ and $\lambda_{0.5y}$ is 0.5 correction length of surface profile in x and y direction, respectively (Fig. 1-18, $\gamma = 1$, $\gamma > 1$, and $\gamma < 1$ correspond to isotropic, longitudinal, and transverse roughness, respectively). In Fig. 1-19 (a), as the film thickness h increases toward the isotropic roughness, the influence of the surface roughness on the fluid flow decreases, and the pressure flow factor converges to 1. Since the longitudinally oriented contact areas resist the pressure flow less, the pressure flow factor is greater than 1. Whereas, the transversely oriented contact areas are highly resistant to pressure flow, and thus the pressure flow factor is lower than that in the isotropic contact areas (Fig. 1-19 (b)). Many researchers [87-89] designed and proposed numerical flow simulations to obtain the flow factors applicable to

the mixed-boundary lubrication regime.

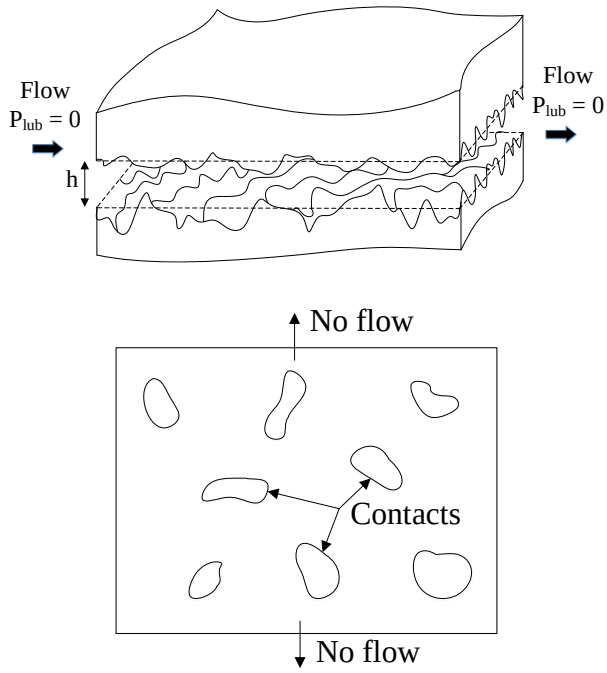

Fig. 1-17. Flow model problem for numerical simulation describing one-directional flow between rough surfaces.

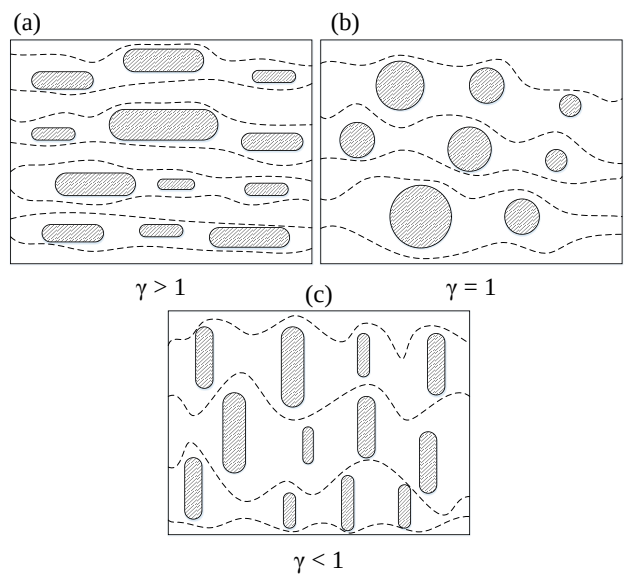

Fig. 1-18. Fluid flow accordant with the roughness orientation characteristics: (a) longitudinally oriented, (b) isotropic, and (c) transversely oriented.

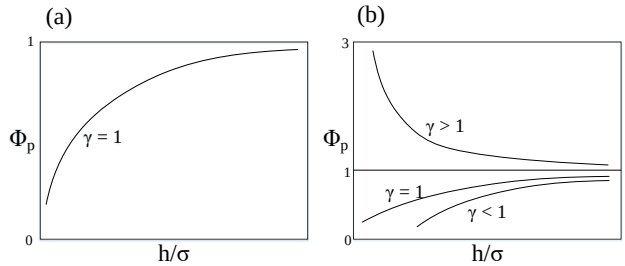

Fig. 1-19. (a) The pressure flow factor variation according to the ratio of film thickness and surface roughness, (b) the pressure flow factor variation accounting orientational characteristics of roughness.

In the mixed-boundary and hydrodynamic lubrication, most friction models assume the Newtonian fluid, and the viscous shear stress is given as follows [87].

$$\tau = \eta \frac{\partial \mathbf{v}}{\partial z} = \frac{\eta\left(\mathbf{v}_2 - \mathbf{v}_1\right)}{h} + \frac{\left(2z - h\right)}{2} \nabla p_{\text{lub}} \tag{1.12}$$

The load-sharing concept, first proposed by Johnson et al. [88], has been used as a general approach for friction modeling in mixed-boundary lubrication. The load-sharing concept, which is advantageous because of its robustness and simple methodology, simplifies friction conditions by separately modeling smooth surface lubrication and dry rough surfaces as in Fig. 1-20. The friction model under mixed-boundary lubrication conditions can be constructed by the proportion of the ratio of separately calculated

hydrodynamic force and asperity contact force.

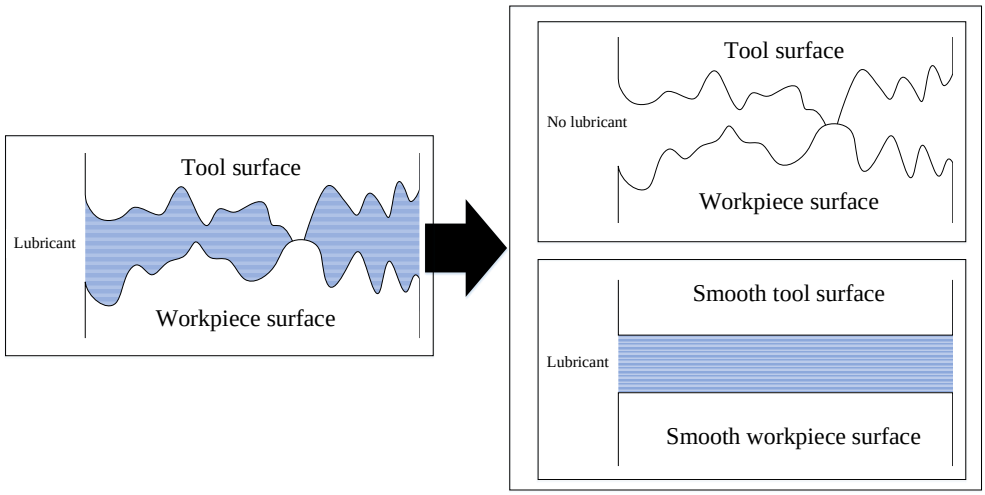

Fig. 1-20. Load-sharing concept for friction modeling in mixed-boundary condition.

Friction model on mixed-boundary lubrication condition since the 19th century

Early models were proposed to solve the Reynolds equation in mixed-boundary and hydrodynamic lubrication associated with the particular metal forming processes. In these models, the lubrication flow is generally analyzed by dividing the area into two separate regions: the inlet zone where the lubricant flows into, and the work zone where the deformation of the workpiece occurs (Fig. 1-21). In addition, various assumptions are applied for the analytical calculation of the Reynolds equation. First, the hydrodynamic pressure is generated due to the reduction of film thickness in the inlet zone and it does not affect the workpiece deformation in the work zone. Secondly,

the pressure gradient in the work zone does not affect the lubrication flow. Lastly, the lubricant is an incompressible and Newtonian fluid.

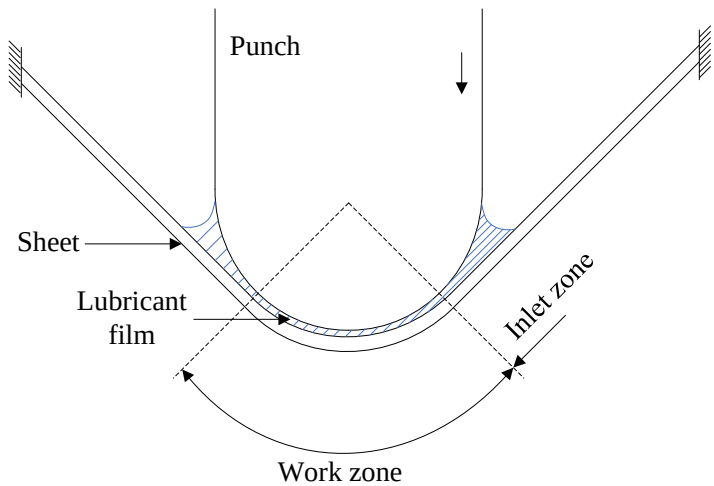

Fig. 1-21. Schematic view of the inlet and work zone in the lubricated sheet metal forming process

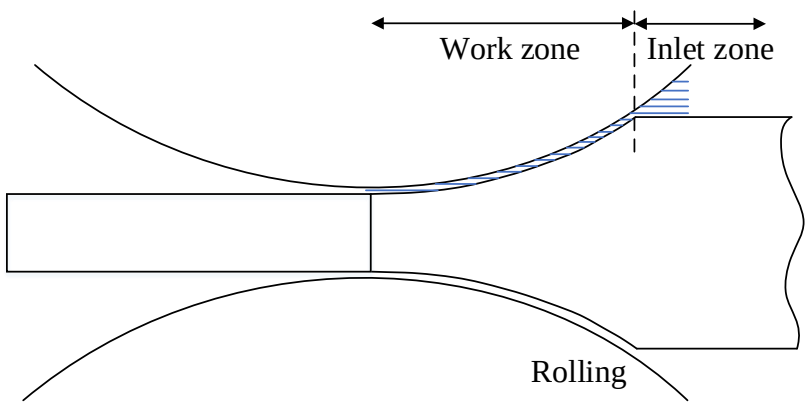

Fig. 1-22. Schematic view of the inlet and work zone in the lubricated strip rolling process

This approach was first proposed by Wilson [92, 93] in hydrodynamically lubricated bulk forming process (Fig. 1-22), and also introduced by Wilson and Wang [94] in hydrodynamically lubricated simple stretch forming process

(Fig. 1-21). Wilson and Wang analytically calculated the Reynolds equation using various assumptions in the 2D axisymmetric forming process, so that it was possible to represent the film thickness and friction stress as process variables (material properties, sheet thickness, and width, punch radius, punch speed, etc.).

Chen and Sun [95] and Sun et al. [96] combined the hydrodynamic lubrication model [94] and finite element plasticity analysis for the axisymmetric stretch forming problem. Wilson and Wang's approach extended the work by Wilson and Hector [97] by introducing a squeeze effect in the inlet zone. Moreover, they combined an elastoplastic finite element analysis with the work by Hsu and Wilson [98]. With the same approach, Sheu and Wilson [99] analyzed the effects of surface roughness and bulk deformation on the lubrication flow on the mixed-boundary lubrication condition. The bulk deformation effect was comprised of the friction model based on previous studies [64] describing effective hardness reduction with bulk deformation. In addition, the average Reynolds equation and load-sharing concept were applied to account for direct metal-to-metal contact due to surface roughness in mixed-boundary lubrication. In the strip rolling process of aluminum utilizing mineral oil as a lubricant, the film thickness was experimentally measured and compared with the results of the model. Wilson et al. [100] proposed the friction model in the sheet metal forming

process with mixed-boundary lubrication, as in the analysis of Shen and Wilson [99]. They calculated the strain distribution through plasticity finite element simulation combined with the friction model, which agreed well with the experimental results. Fig. 1-23 shows the flow chart of the coupling between the finite element solution and the friction model. Karupannasamy et al. [101] calculated the average film thickness by estimating the space under the tool surface. They evaluated the volume of lubricant based on the Westeneng contact model and proposed the friction model for the axisymmetric deep drawing processes on the mixed-boundary lubrication condition.

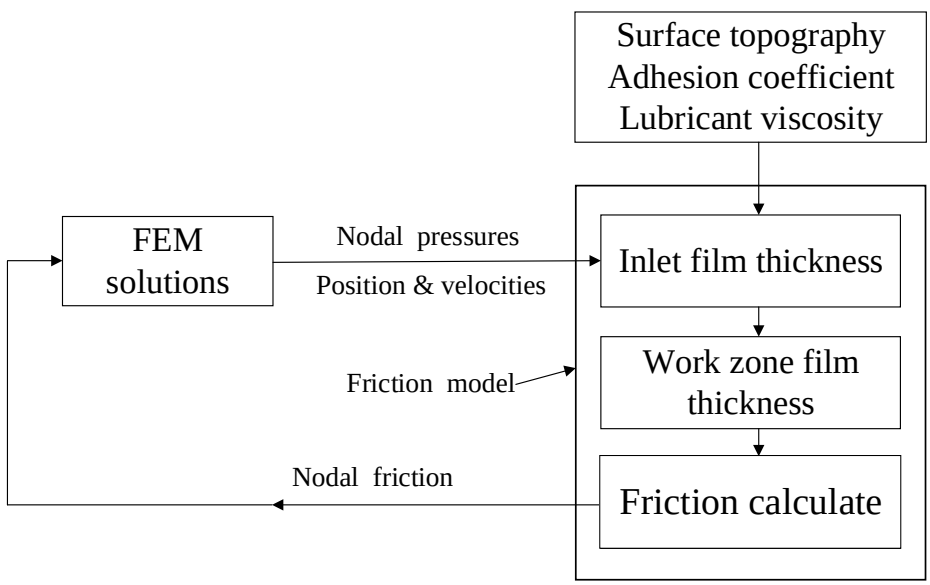

Fig. 1-23. Flow diagram of coupling between finite element solution and friction model

The finite element method is another approach to lubrication flow analysis

by solving the Reynolds equation. Initially, the application of the finite element method was used to describe the lubrication flow of the bearing and gear, and Brooker and Huebner [102] described the detailed finite element methodology for a novice. Hu and Liu [103] first applied this coupled finite element approach and arbitrary Lagrangian-Eulerian (ALE) formulation to the mixed-boundary lubrication in the steady-state strip rolling process. Yang and Lo [104] employed the finite element approach on the full film lubricated axisymmetric cup stretching process. In addition, the mixed-boundary lubrication condition, which is a multi-physical problem where deformation of metal and lubrication flow are combined, can be solved with finite element analysis as shown in Fig. 1-24. To verify the result of finite element analysis for the lubricated forming process, the calculated film thickness based on the Yang and Lo [104] was compared with both experimental measurements of Wilson and Hector [97] and the theoretical results of Hsu and Wilson [95]. Boman and Ponthot [105] proposed the finite element analysis combined with the Streamline Upwind Petrov-Galerkin (SUPG) method to eliminate numerical errors (e.g. oscillations) which often occur due to the large non-linearity of the lubrication viscosity. Hol [106] proposed a new mixed-boundary lubrication friction model by combining the boundary lubrication friction model [80] and the hydrodynamic model. Hol implemented the finite element approach by configuring the interface element and degrees of freedom for the lubrication flow analysis. To verify this friction model, the

experimentally measured punch force-displacement was compared with the result of the finite element forming simulations.

Based on the previous studies of Hol [80], TriboForm was developed that provides a friction model that can be applied according to lubrication and contact conditions in various sheet metal forming process. The TriboForm not only provides a friction model for the user's selection, including a database of various lubricants, material properties and surface information, but also provides a friction model under user input conditions. TriboForm software includes FEM plug-in function that provides sheet metal forming simulation with advanced tribology, friction and lubrication models applied to the FEM software AutoForm. Sigvant [107] used the FEM plug-in function of TriboForm software to determine the influence of tribology in the sheet metal forming process simulation for an inner door of a vehicle. In this study, it was verified that the simulation result using the TriboForm was more accurate than the simulation result using a constant friction coefficient by comparing the edge shape and the presence of wrinkles of the actual inner door.

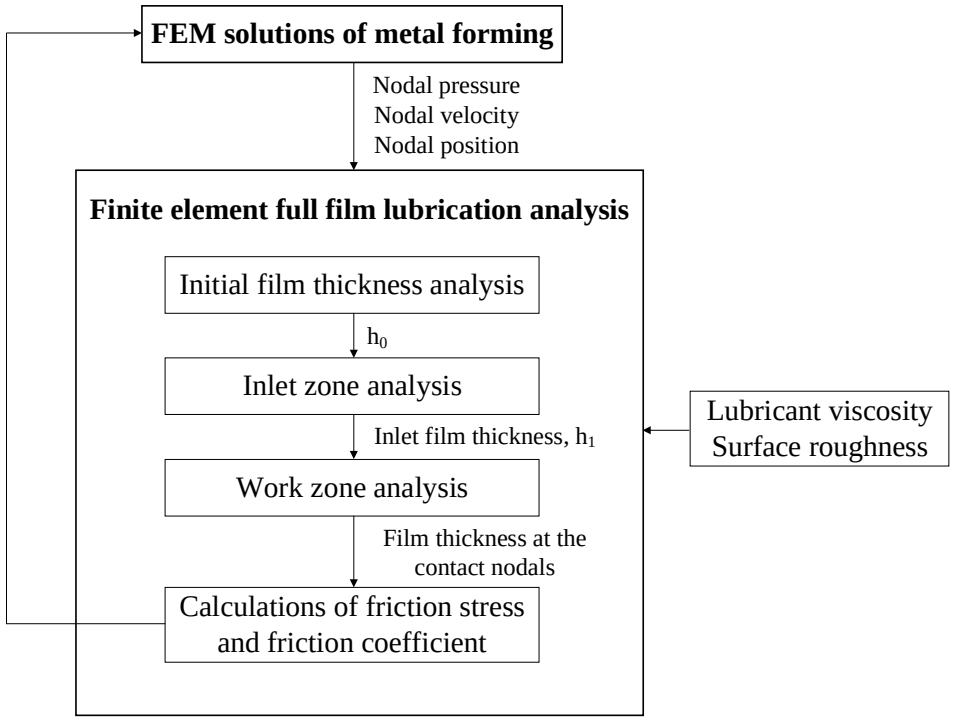

Fig. 1-24. Flow diagram describing simultaneous analysis of film lubrication and metal forming process through finite element method.

2. Friction model in boundary lubrication

Boundary lubrication has minor lubrication effect between contacts, and it results in direct contact of surface asperities. The surfaces of workpiece and tool have rough roughness at micro-scale, and contacts occur locally, unlike a nominal contact. The friction in the boundary lubrication is highly dependent on the real contact area. The plowing (or ploughing) and adhesion effects between the real contacts are the main causes of the friction. In this chapter, a new approach is introduced to accurately describe these frictional behaviors, and is based on the friction model under the boundary lubrication.

The framework of the friction coefficient prediction model in the boundary lubrication is described in Section 2.1. In Section 2.2, the real contact area variation as functions of of normal loading, bulk strain, and sliding state is derived along with a theoretical explanation of the statistical contact model developed in this thesis. Section 2.3 introduces a new approach for tool shape modeling that determines the frictional force due to the plowing effect.

2.1. Framework of friction model in boundary lubrication

The overall framework of the boundary lubrication friction model constructed in this thesis is introduced. The framework of friction modeling in the boundary lubrication mainly consists of three steps, as shown in Fig. 2-1. The

first step is to configure the input parameters such as the boundary layer shear strength, workpiece material properties, and microscale 3D surface profile data of the tool and the workpiece, which are required by the friction model in boundary lubrication. In the second step, the contact model proposed by Hol [80] is emplolyed to obtain the real contact area ratio due to the deformation of the workpiece asperity caused by the contact between the tool and the workpiece. In the contact model, the variations of contact area as functions of the normal loading, bulk strain, and sliding are considered. A detailed description of contact modeling is described in Section 2.2. The final step is the process of calculating the friction coefficient by the friction modeling that takes into account the adhesion and plowing effects. In the friction model, the total friction coefficient is the sum of the friction forces due to adhesion and plowing at each asperity of the tool, and each friction force depends on the indentation depth of the tool and the geometric shape. The indented depth of each tool asperity is determined by the real contact area obtained in the second step and the equilibrium position of the tool mean plane that satisfies the newly proposed force balance equation. In addition, the shape of each tool asperity is determined as a reference point that identifies the periodic characteristics of the tool surface and distinguishes individual asperities. This new approach for friction modeling is detailed in Section 2.3.

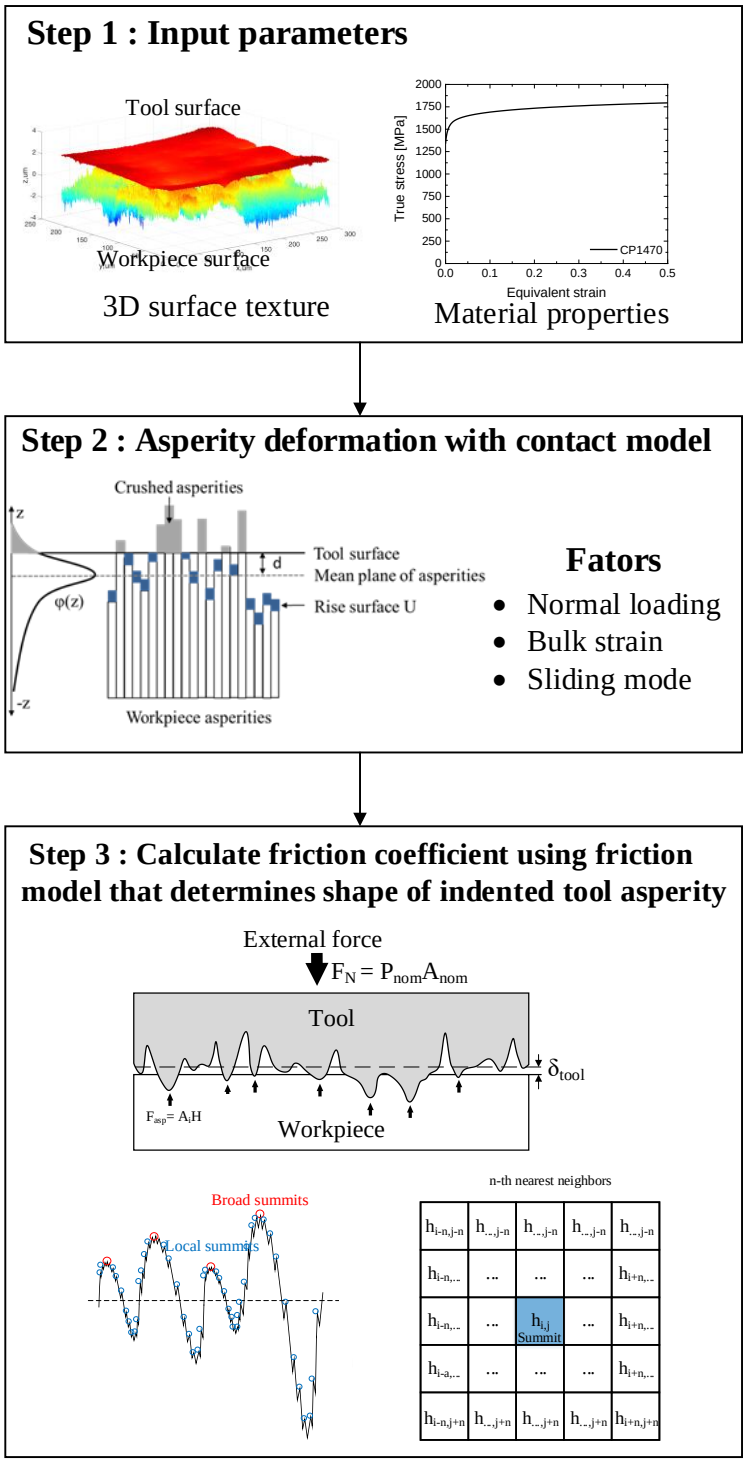

Fig. 2-1. Overall flow and method of boundary lubrication friction modeling

2.2. Statistical contact model for describing surface deformation

In the statistical contact model originally proposed by Greenwood and Wiliamson [11], the workpiece surface is modeled as a spherical asperity group with a constant radius. It follows a Gaussian summit height distribution function. The summit is determined by its the nearest neighbor, thus it depends on the resolution of the surface scanning equipment. Due to the fractal nature, high-resolution scanning measurement increases the number of summits and decreases the spherical radius. In this study, the deformation of the spherical asperities during contact was assumed to be an elastic according to Hertz's law [48, 49]. Westeneng [77] proposed a rough surface modeling as a group of bar-shaped asperities with different heights instead of a statistical contact model based on the summit height. Unlike the summit height distribution, the height distribution of the model proposed by Westeneng converges beyond a certain resolution. Also, the deformation of asperities was assumed to be an ideal plastic. After the contact model described by Westeneng, Hol [80] proposed a newly developed contact model by considering the shear stress between asperities and the work hardening of the workpiece asperities. This section describes overall derivation of the contact model proposed by Hol [80] for real contact area prediction.

2.2.1. Assumptions for modeling

Like most statistical contact models, the tool surface was assumed to be a smooth rigid surface because it is much harder than the workpiece. In the contact model by Westeneng [77], the workpiece surface was modeled as a group of bars, and the width of the bar was determined by the resolution of the measuring instrument. The height of the bars is expressed as a Gaussian distribution function whose height distribution is determined by the standard deviation as follows:

$$\varphi_w(z) = \frac{1}{\sigma_w\sqrt{2\pi}} \exp\left(\frac{-z^2}{2\left(\sigma_w{}^2\right)}\right) \tag{2.1}$$

where z is the height of the bar, σ_w is the standard deviation of the workpiece surface, and $\varphi_w(z)$ is the workpiece surface distribution function. Since the height distribution of the workpiece is represented only by the standard deviation, the height information has no relation to the position (x, y) and only depends on a probability according to the height. Three variables are introduced for modeling the deformation of workpiece asperities. The first is the rising length of the non-contact asperity U_L, the second is the distance between the mean plane of the workpiece asperity and the tool surface d_L, and the last is the previously mentioned workpiece surface distribution function $\varphi_w(z)$, which are shown in Fig. 2-2. These variables enable the

transformation of the modeling of workpiece surface deformation behavior from the micro-scale to the macro-scale.

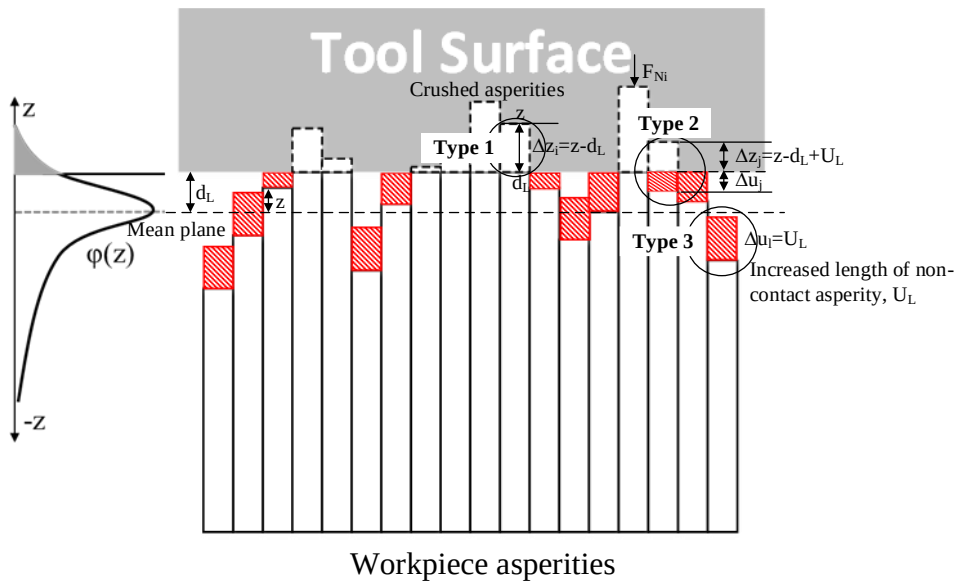

Fig. 2-2. Flattening of rough workpiece surface modeled as a group of bars with different heights

Assuming that neighboring (other) asperities are not affected by the deformation of each asperity, the strain of each workpiece asperity according to the contact condition is expressed as the following equations.

$$\varepsilon = \begin{cases} \ln\left(\dfrac{z+\lambda}{d_L+\lambda}\right) & \text{for } z \geq d_L - U_L \text{ (Contact)} \\ \ln\left(\dfrac{d_L+\lambda}{z+\lambda}\right) & \text{for } z < d_L - U_L \text{ (No contact)} \end{cases} \tag{2.2}$$

where ε is the equivalent strain, λ is the reference height.

The maximum stress of the bar asperity is assumed to be the hardness of the material, and approximated as follows (Tabor [38]):

$$H = 2.8\sigma(\varepsilon) \tag{2.3}$$

where H is the hardness of workpiece, σ is the true stress.

The hardening behavior model of the workpiece asperity is described as the Swift-Voce hardening law.

$$\sigma(\bar{\varepsilon}) = R \cdot K\left(\varepsilon_0 + \bar{\varepsilon}\right)^n + (1-R)\left[\sigma_s - (\sigma_s - \sigma_y)\exp\left(\frac{-\bar{\varepsilon}}{C}\right)\right] \tag{2.4}$$

The hardening parameters are listed in Table 4-1.

2.2.2. Flattening of workpiece asperity due to normal load

The real contact area ratio α_L, which indicates the contact ratio of the workpiece asperities, is expressed as a function of d_L and U_L as shown in the following equation.

$$\alpha_L = \int_{d_L - U_L}^{\infty} \varphi_w(z)\, dz \tag{2.5}$$

In Eq. (2.5), the minimum height of asperity for contact is $d_L - U_L$, because the height becomes d_L as it rises by U_L through contact. Therefore, d_L and

U_L are variables that represent the equilibrium state of contact, and they are determined through two assumptions that describe the deformation behavior of asperities. Under this scheme, it is noted that the energy conservation law and volume conservation law should be satisfied.

In order to satisfy the energy conservation, the amount of energy exerted by the external force should be equal to the magnitude of the internal energy. The direction of the external force is the same as the direction in which the workpiece asperity is pressed. Therefore, the energy required to indent the asperities is equal to the external energy. The workpiece asperities are divided into three types according to their deformation mode: the pressed asperities (type 1), asperities pressed due to rise (type 2), and rising asperities (type 3). Here, the following notations are introduced. That is, N is the number of pressed asperities, $N*$ is the number of pressed asperities due to rise, $N**$ is the number of rising asperities, and the total number of asperities is N_{total} (ie, $N_{total} = N + N* + N**$). The pressed asperities and asperities pressed due to rise make contacts with tool, but the remaining rising asperities do not contact with the tool. As shown in Fig. 2-2, the variable Δz is the pressed length of asperity, and variable Δu is the rising length of asperity. The external energy $W_{external}$ depends on the number of asperities in contact with the tool and is given by the following equation.

$$W_{external} = \underbrace{\sum_{i=1}^{N} F_{N,i}\Delta z_i}_{\text{pressed asperities}} + \underbrace{\sum_{j=1}^{N^*} F_{N,j}\Delta z_j}_{\text{pressed asperities due to rise}} = \sum_{k=1}^{N+N^*} F_{N,k}\Delta z_k \tag{2.6}$$

where ΔA is the contact area of a single asperity, and $F_{N,k}$ is the force acting on the asperity in contact with $F_{N,k} = H_k \Delta A$. The calculation of Eq. (2.6) is valid when the heights of all asperities are known, which is not flausible because the workpiece asperities are expressed as a probability distribution function. Then, it is converted into a stochastic form as follows:

$$W_{external} = F_N \omega \tag{2.7}$$

with

$$\begin{aligned}\omega &= \frac{\sum_{k=1}^{N+N^*} F_{N,k}\Delta z_k}{F_N} = \frac{\sum_{i=1}^{N} F_{N,i}\Delta z_i + \sum_{j=1}^{N^*} F_{N,j}\Delta z_j}{F_N} \\ &= \frac{\int_{d_L}^{\infty} \sigma_y(z)(z-d_L)\varphi_w(z)dz + \int_{d_L-U_L}^{d_L} \sigma_y(z)(z-d_L+U_L)\varphi_w(z)dz}{\int_{d_L-U_L}^{\infty} \sigma_y(z)\varphi_w(z)dz}\end{aligned} \tag{2.8}$$

where F_N is the total external force and ω is the external energy factor.

$$\Delta z_i = z - d_L \tag{2.9}$$

$$\Delta z_j = z - d_L + U_L \tag{2.10}$$

The height of the pressed asperity (type 1) before contact is z, and it changes to height d_L in the equilibrium state after contact, which is expressed by Eq. (2.9) (Fig. 2-2). The asperity pressed due to rise (type 2) should be

changed from height z to $z+U_L$ by the rise, but it is pressed to height d_L by contact, which is expressed by Eq. (2.10) (Fig. 2-2).

The total internal energy ($W_{\text{int}ernal}$) is the sum of the energy absorbed by the contacting asperities ($W_{\text{int},ab}$), the energy consumed for the rise of asperities ($W_{\text{int},ri}$), and the energy lost due to the shear stress occurring between each asperity ($W_{\text{int},sh}$).

$$W_{\text{int}ernal} = W_{\text{int},ab} + W_{\text{int},ri} + W_{\text{int},sh} \tag{2.11}$$

Since the $N+N^*$ asperities are deformed, the energy absorbed by the contacting asperities $W_{\text{int},ab}$ is written as:

$$W_{\text{int},ab} = \sum_{k=1}^{N+N^*} H\Delta A\Delta z_k = 2.8\Delta A\sum_{k=1}^{N+N^*} \sigma_{y,k}\left(\varepsilon\right)\Delta z_k = 2.8\gamma \tag{2.12}$$

with

$$\gamma = \Delta A\sum_{k=1}^{N+N^*} \sigma_{y,k}\left(\varepsilon\right)\Delta z_k \tag{2.13}$$

where ΔA is the area of single asperity, and γ is the first internal energy factor among the three terms of internal energy. From Eq. (2.2) and Eq. (2.4), the true stress $\sigma_{y,k}\left(\varepsilon\right)$ of the workpiece asperity is determined differently by the equivalent strain of each asperity considering the effect of hardening behavior.

The energy due to the rise of asperities $W_{\text{int},ri}$, which is the second term of internal energy, is consumed in N^*+N^{**} number of rise asperities excluding the N pressed asperities. Then,

$$\begin{aligned} W_{\text{int},ri} &= \eta\left(\sum_{j=1}^{N^*} H\Delta A\Delta u_j + \sum_{l=1}^{N^{**}} H\Delta A\Delta u_l\right) \\ &= 2.8\eta\Delta A\left(\sum_{j=1}^{N^*}\sigma_{y,j}\Delta u_j + \sum_{l=1}^{N^{**}}\sigma_{y,l}\Delta u_l\right) \\ &= 2.8\eta\beta \end{aligned} \tag{2.14}$$

with

$$\beta = \Delta A\left(\sum_{j=1}^{N^*}\sigma_{y,j}\Delta u_j + \sum_{l=1}^{N^{**}}\sigma_{y,l}\Delta u_l\right) \tag{2.15}$$

where β is the second internal energy factor, namely, the asperity persistence parameter. η is a value expressed as the ratio of the energy required to press the asperity to the energy required for the asperity to rise. In this study, η is set to 0 [80].

The last term of internal energy $W_{\text{int},sh}$ is derived as follows.

$$\begin{aligned} W_{\text{int},sh} &= \left(1-\frac{A_{real}}{A_{nom}}\right) n_s \sum_{j=1}^{N+N^*} \tau_{sh,k} A_{sh,j}\Delta s_k \\ &= \frac{1}{\sqrt{3}}\left(1-\frac{A_{real}}{A_{nom}}\right) n_s w \sum_{j=1}^{N+N^*} \sigma_{y,k}\Delta s_k^2 \\ &= \frac{1}{\sqrt{3}}\psi \end{aligned} \tag{2.16}$$

with

$$\psi = \left(1 - \frac{A_{real}}{A_{nom}}\right) n_s w \sum_{j=1}^{N+N^*} \sigma_{y,k} \Delta s_k^2 \tag{2.17}$$

where A_{real} is the real contact area, A_{nom} is the nominal area, n_s is half of the number of surrounding asperities, τ_{sh} is the shear strength, A_{sh} is the area of shearing, and Δs is the distance of shear. Asperity in contact with the tool moves differently from its surrounding asperties to satisfy the volume conservation, which generates the shear energy. The shear distance Δs is equal to $z - d_L + U_L$ by adding the pressing distance $z - d_L$ of the asperity and the rising distance U_L of the surrounding asperities. Also, the area of shearing A_{sh} is the product of the width w of the asperity and the shear distance Δs (or $w\Delta s$). The workpiece was assumed to follow isotropic plasticty and can be modeled by the von-Mises yield criterion. Then, the shear strength τ_{sh} can be approximated as $\frac{\sigma_y}{\sqrt{3}}$. The value $\left(1 - \frac{A_{real}}{A_{nom}}\right)$ represents the probability of non-contacting neighboring asperity of the pressed asperity, which is introduced because the information of the neighboring asperity cannot be known in the probabilistic form. As the external energy factor is converted into a stochastic form as in Eq. (2.8), the internal energy factors are expressed in a stochastic form as follows:

$$\begin{aligned}\gamma &= \Delta A \sum_{k=1}^{N+N^*} \sigma_{y,k}(\varepsilon)\Delta z_k \\ &= A_{nom}\left(\int_{d_L}^{\infty} \sigma_y(z)(z-d_L)\varphi_w(z)dz + \int_{d_L-U_L}^{d_L} \sigma_y(z)(z-d_L+U_L)\varphi_w(z)dz\right)\end{aligned} \tag{2.18}$$

$$\begin{aligned}\beta &= \Delta A\left(\sum_{j=1}^{N^*} \sigma_{y,j}\Delta u_j + \sum_{l=1}^{N^{**}} \sigma_{y,l}\Delta u_l\right) \\ &= A_{nom}\left(\int_{d_L-U_{L:}}^{d_L} \sigma_y(z)(d_L-z)\varphi_w(z)dz + \int_{-\infty}^{d_L-U_L} \sigma_y(z)U_L\varphi_w(z)dz\right)\end{aligned} \tag{2.19}$$

$$\begin{aligned}\psi &= \left(1-\frac{A_{real}}{A_{nom}}\right)n_s w \sum_{j=1}^{N+N^*} \sigma_{y,k}\Delta s_k^2 \\ &= N_{total} n_s w \int_{-\infty}^{d_L-U} \varphi_w(z)dz\left(\int_{d_L-U_{L:}}^{\infty} \sigma_y(z)(z-d_L+U_L)^2\varphi_w(z)dz\right)\end{aligned} \tag{2.20}$$

All energy factors ($\omega, \gamma, \beta, and\ \psi$) are determined by the stochastic parameters d_L and U_L , and the energy conservation law is expressed as follows:

$$p_{nom} = \frac{2.8}{A_{nom}}\left(\frac{\gamma}{\omega} + \eta\frac{\beta}{\omega}\right) + \frac{1}{A_{nom}\sqrt{3}}\frac{\psi}{\omega} \tag{2.21}$$

where p_{nom} is the nominal pressure, defined as $p_{nom} = \frac{F_N}{A_{nom}}$.

The second assumption, or the volume conservation law, satisfies that the sum of the volume changes of all asperities is zero because the deformation behavior of the workpiece surface is assumed to be plastic. As shown in the following equation, the volume variation of the asperities compressed by contact is same as the volume variation due to the rise of other asperities.

$$\sum_{i=1}^{N} \Delta z_i \Delta A = \sum_{j=1}^{N^*} \Delta u_j \Delta A + \sum_{l=1}^{N^{**}} \Delta u_l \Delta A \tag{2.22}$$

The stochastic form of Eq. (2.22) determined by d_L and U_L can be written as follows:

$$U_L\left(1-\alpha_L\right) = \int_{d_L-U_L}^{\infty} \left(z-d_L\right)\phi_w\left(z\right)dz \tag{2.23}$$

The three variables α_L , d_L , and U_L are calculated by applying the Newton-Raphson method to Eqs. (2.5), (2.21), and (2.23).

2.2.3. Flattening of workpiece asperity due to normal load and sliding

The real contact area increases during sliding of workpiece, and Hol [80] explained the effect of sliding on friction by suggesting the following two mechanisms. First, the flat tool surface assumed in Section 2.2.2 has tool roughness at smaller scale, and the tool is much harder than the workpiece. Therefore, it penetrates the workpiece as shown in Fig. 2-3. When sliding starts, the contact area of the tool asperity is roughly halved as shown in Fig. 2-4, and more penetration into the workpiece occurs in order to balance the force. It is assumed that the real contact area is increased by approximately 2 times to satisfy the force equilibrium as follows:

$$\alpha_S = 2\alpha_L \tag{2.24}$$

where α_S is the real contact area ratio considering the sliding effect, and the subscript S denotes the sliding effect.

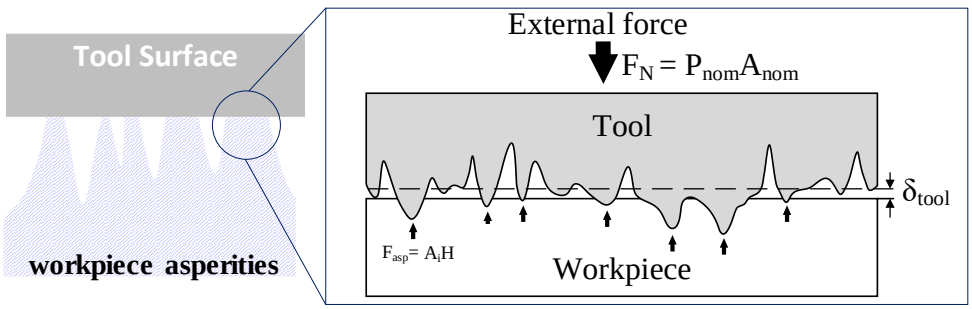

Fig. 2-3. Schematic view on force equilibrium between the external force and total indented force by tool summit asperities

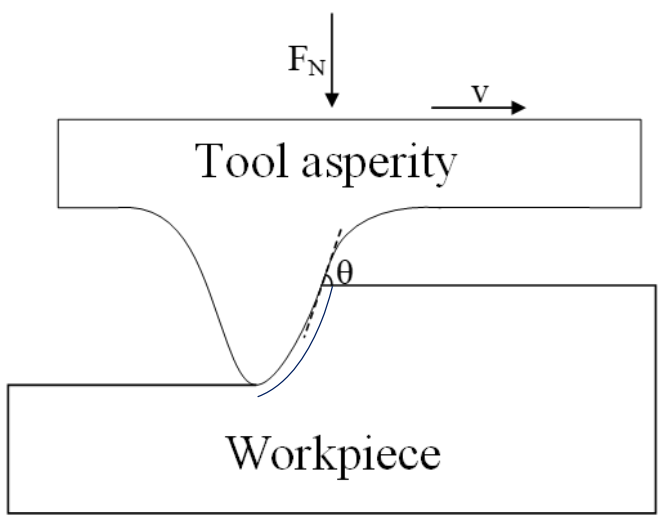

Fig. 2-4. Schematic view of contact area of single tool asperity during sliding

As the second mechanism, the sliding effect was considered by applying the junction growth theory proposed by Tabor [38], which was introduced in Section 1.3. In the junction growth theory, the increase of the real contact area

is written as follows:

$$\alpha_S^{n+1} = \sqrt{1+3\mu\left(\alpha_S^n\right)} \cdot \alpha_S^n \tag{2.25}$$

Since the above equation is non-linear, the real contact area ratio α_S is determined iteratively. Using the initial value from Eq. (2.24), Eq. (2.25) iterates until the absolute value of the difference between α_S^{n+1} and α_S^n becomes less than a predefined tolerance. When it is converged with the value α_S^{n+1}, d_S and U_S are calculated uisng Eqs. (2.5) and (2.23) (the subscript L is converted to s).

2.2.4. Flattening of workpiece asperity due to normal load and bulk strain

The sheet workpiece is subjected to the bulk strain in the forming process. Then, the bulk strain changes the surface topology and increases the real contact area under normal load. Westeneng [77] derived an analytical contact model by assuming the bulk strain as an ideal plastic deformation of the 2-dimensional workpiece asperity. In this section, the subscript ε refers to variables taking into account the effect of bulk strain.

$$\frac{d\alpha_\varepsilon}{d\varepsilon} = l_m W \frac{d\alpha_\varepsilon}{d\left(U_\varepsilon - d_\varepsilon\right)} = l_m W \frac{d}{d\left(U_\varepsilon - d_\varepsilon\right)}\left(\int_{d_\varepsilon - U_\varepsilon}^{\infty} \varphi_w\left(z\right)dz\right) = l_m W \varphi_w\left(d_\varepsilon - U_\varepsilon\right) \tag{2.26}$$

with

$$\alpha_\varepsilon = \int_{d_\varepsilon - U_\varepsilon}^{\infty} \varphi_w\left(z\right)dz \tag{2.27}$$

In Eq. (2.26), W represents a velocity parameter defined as,

$$W = \frac{v_a + v_b}{\dot{\varepsilon} l_m} \tag{2.28}$$

where v_a is the downward velocity of pressed asperities, v_b is the upward velocity of non-contacting asperities, l_m is the mean half spacing between asperities, and $\dot{\varepsilon}$ is the bulk strain rate. Sutcliffe [65] described the deformation behavior of wedge-shaped asperities under combined normal force and bulk deformation using the slip-line field analysis. For the slip-line analysis, the asperities were assumed to be an ideal plastic material under plane strain condition. Westeneng [77] derived a semi-empirical relationship between the velocity parameter W and the characteristic slip-line angle Ω based on the slip-line field analysis proposed by Sutcliffe as follows:

$$W = -0.184 + 1.21\exp\left(1.47\Omega\right) \tag{2.29}$$

$$\Omega = \frac{H_{eff}}{4\tau_{sh}}\left(1-\alpha_{\varepsilon}\right) \tag{2.30}$$

where the effective hardness of workpiece H_{eff} is defined as $H_{eff} = \frac{p_{nom}}{\alpha_{\varepsilon}}$.

The mean half spacing l_m is defined by:

$$l_m = \frac{1}{2\sqrt{\rho_w \alpha_{\varepsilon}}} \tag{2.31}$$

where ρ_w is the density of workpiece asperities. Hol [80] proposed an asperity density ρ_w of a random surface through surface measurement as a function of nominal pressure P_{nom} with the following relation:

$$\rho_w = c_1 \exp\left(c_2 P_{nom}\right) + c_3 \exp\left(c_4 P_{nom}\right) \tag{2.32}$$

with $c_1 = 1.49\times10^3$, $c_2 = -0.458$, $c_3 = 3.14\times10^2$, and $c_4 = -0.046$.

The value α_{ε} is calculated by integrating its increment $d\alpha_{\varepsilon}$ until the sum of bulk strain increment $d\varepsilon$ becomes the target total bulk strain ε in Eq. (2.26). At the same time, d_{ε} and U_{ε} corresponding to α_{ε} should be updated. Therefore, α_{ε} calculated by the Euler method in Eq. (2.26) is updated and d_{ε} and U_{ε} are determined by Eqs. (2.5) and (2.23) for each iteration. Finally, α_{ε} in consideration of the bulk strain effect can be obtained.

2.3. Friction model through a new approach

The plateau of the workpiece deformed by contact was assumed to be an ideal flat surface in the previous contact model, as shown in Fig. 2-3. This assumption may not be valid because the roughness of the tool is commonly smaller than that of the workpiece. The friction model of Challen and Oxley [22, 60], mentioned in the previous section, was derived from an Eq. (1.5) for determining the friction coefficient of a single asperity, which accounts for the combined effect of the plowing and adhesive between surfaces. The sum of the frictional forces generated by each tool asperity was derived as the total friction force. The friction force of each tool asperity is determined by the following two main factors. The first is the equilibrium position of the tool surface between the contacts, which determines the indentation depth of the tool asperity. The second is the geometric shape of each tool asperity because the friction coefficient depends on the geometry of the tool, even if the indentation depth is the same. This section introduces a newly proposed approach for determining these main factors.

2.3.1. An elliptical paraboloid asperity model

In this study, the shape of the tool asperity is approximated as an elliptical paraboloid, and the geometric parameters shown in Fig. 2-5 include the

lengths of major $2a$ and minor axes $2b$, the orientation angle φ, and the penetration depth w. Since it is assumed as a paraboloid, the penetration depth w is twice the average of penetrated depth w_i of each asperity, which is written as follows:

$$w = \frac{2}{n}\sum_{i=1}^{n} w_i \tag{2.33}$$

In Fig. 2-5, the effective attack angle θ_{eff} is defined by the following equation in the parabolic shape.

$$\theta_{eff} = \arctan\left(\frac{2w}{a_x}\right) \tag{2.34}$$

where a_x is the length from the ellipse center to the boundary of the ellipse on the axis of sliding direction, which can be determined by the size a, b and orientation angle φ of the ellipse.

$$a_x = \frac{ab}{\sqrt{\left(b\cos\varphi\right)^2 + \left(a\sin\varphi\right)^2}} \tag{2.35}$$

θ_{eff} can be rearranged as follows:

$$\theta_{eff} = \arctan\left(\frac{2w\sqrt{\left(b\cos\varphi\right)^2 + \left(a\sin\varphi\right)^2}}{ab}\right) \tag{2.36}$$

Since the model of Challen and Oxley [22, 60] is assumed the 2-

dimensional asperity under the plane strain condition, the effective attack angle θ_{eff} cannot be directly compatible with 3-dimensional asperity. Hokkirigawa and Kato [108] introduced a shape factor χ and modified the θ_{eff} as follows:

$$\theta = \arctan\left(\frac{2w\sqrt{(b\cos\varphi)^2 + (a\sin\varphi)^2}}{\chi ab}\right) \tag{2.37}$$

In this study, χ is used as 0.8 following the experimental value obtained by Hokkirigawa and Kato [108]. Finally, the friction coefficient for the elliptical paraboloid single asperity can be obtained from Eq. (1.5) and Eq. (2.37).

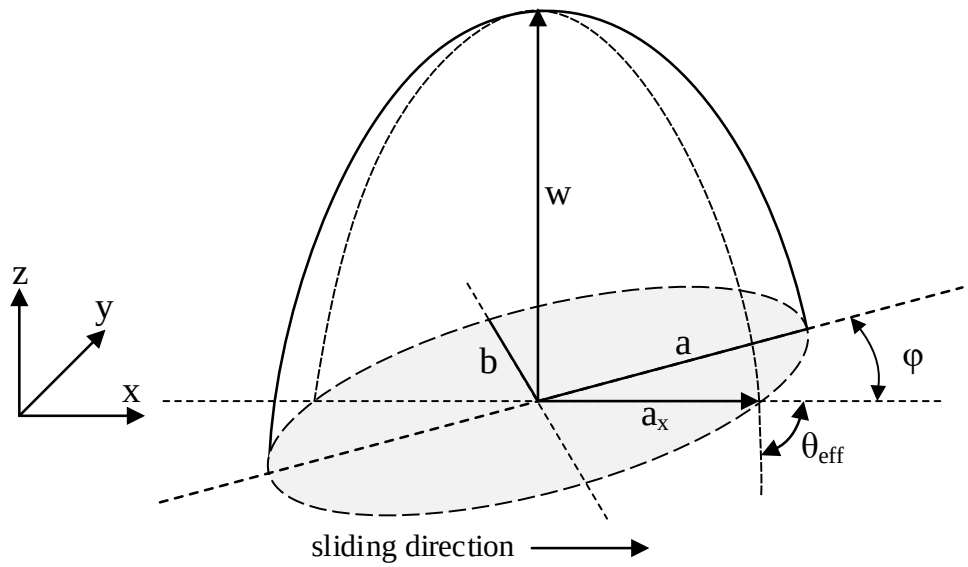

Fig. 2-5. The geometric parameters that determine the elliptical paraboloid

2.3.2. A tool geometry model

The contact equilibrium position of two surfaces in the friction model is expressed as a separation δ_{tool} between the mean plane of tool asperities and the flat workpiece. The surface of the tool is represented by the Gaussian distribution function. In this study, unlike the previous study a new apparoch for determining δ_{tool} is proposed by satisfying the force equilibrium.

The externally applied force can be written as follows.

$$F_N = P_{nom} A_{nom} = H \sum_{i=1}^{n} A_i \tag{2.38}$$

where the total area is,

$$\sum_{i=1}^{n} A_i = \alpha A_{nom} \int_{\delta_{tool}}^{\infty} \varphi_{tool}(s) ds \tag{2.39}$$

Then,

$$P_{nom} A_{nom} = H \alpha A_{nom} \int_{\delta_{tool}}^{\infty} \varphi_{tool}(s) ds \tag{2.40}$$

or

$$P_{nom} A_{nom} = H \left(\frac{\alpha A_{nom} \int_{\delta_{tool}}^{\infty} \varphi_{tool}(s) ds}{2} \right) \tag{2.41}$$

The attack angle depends on the geometry of the tool as well as the indentation depth determined by the force equilibrium, which is described in Fig. 2-6.

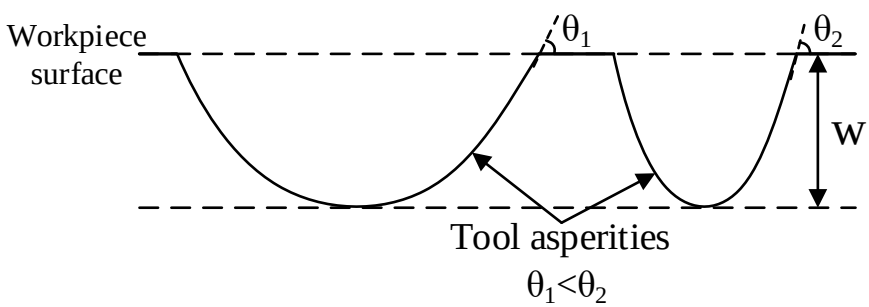

Fig. 2-6. Difference of attack angle due to tool shape difference at the same depth of penetration

The direct modeling of geometrical shape of the indented tool asperities is not plausible because only the Gaussian height distribution function is available. The height distribution (z) with respect to the position (x, y) is

essential and it can be provided from measured surface texture. It is also very challenge to model the shape of each tool asperity from the surface texture data. If the surface roughness of the tool is idealized, different asperities can be intuitively identified as shown in Fig. 2-7(a). However, because the realistic rough surface of the tool is connected to each other as shown in Fig. 2-7(b), it is difficult to distinguish among tool asperities. Therefore, a new procedure that enables the tool shape modeling is proposed by distinguishing different tool asperities.

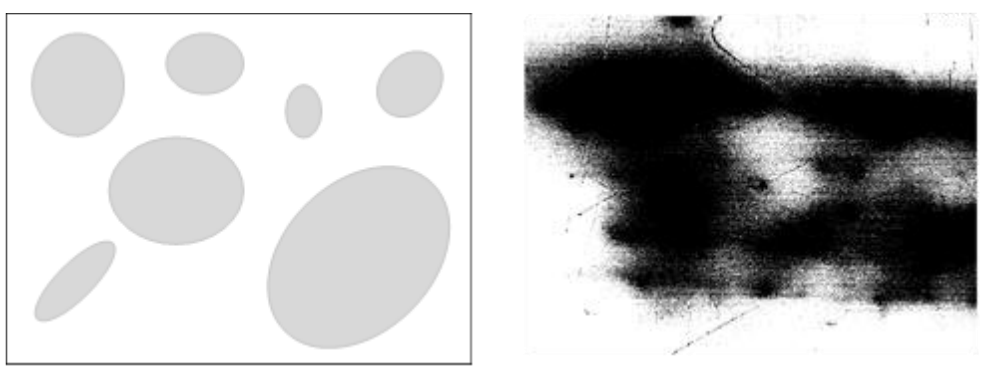

Fig. 2-7. Schematic view representing the contact area of the tool asperities that penetrated into the workpiece

From the two-dimensional profile of the tool roughness shown in Fig. 2-8(a), the rough tool surfac consists of both primary and secondary summits (see definition of the two summits from Fig. 2-8(a)). Since the secondary

summit is determined by comparing the height with its nearest neighbors, it depends on the resolution of the measuring equipment. In contrast, the primary summit is a point having a maximum height within one period of the entire tool surface excluding the smaller secondary periodicity (Fig. 2-8(b)). The position of the primary summit is constant at resolutions sufficiently smaller than the wavelength of the tool surface roughness. The newly proposed procedure enables to distinguish different asperities from a fixed location of only one primary summit within a wavelength.

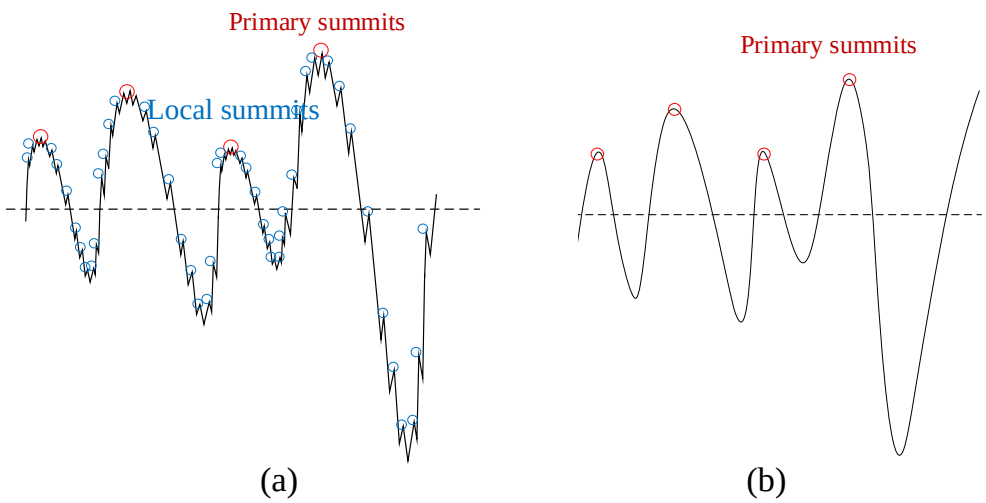

Fig. 2-8. Schematic description of typical summits on the tool surface: (a) realistic tool asperities consisting of primary and secondary summits, and (b) only primary summits.

As shown in Fig. 2-9, the wavelength λ is an average value of the wavelengths determined by the mean plane, and local summits within a range

smaller than this average wavelength λ are ignored in the tool geometry modeling. Instead of determining the local summits located on the nearest neighbors (Fig. 2-10 (a)), the point having the maximum value is determined as the primary summit by comparing all the n-th nearest neighbors (Fig. 2-10 (b).) This number (n) is defined as,

$$n = \frac{\lambda / 2}{a} \tag{2.42}$$

where a is the size of one pixel (or length of resolution).

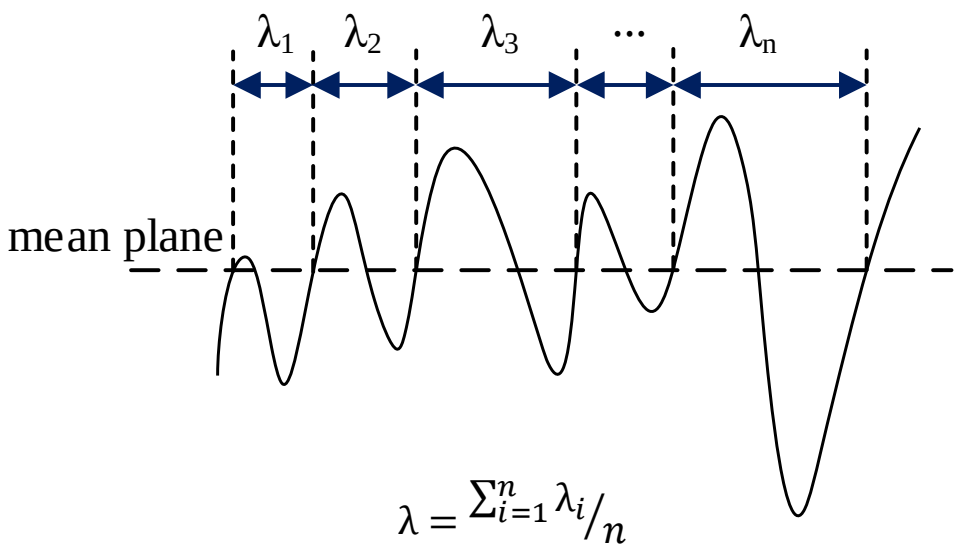

Fig. 2-9. Schematic description of the average wavelength determined from the rough surface

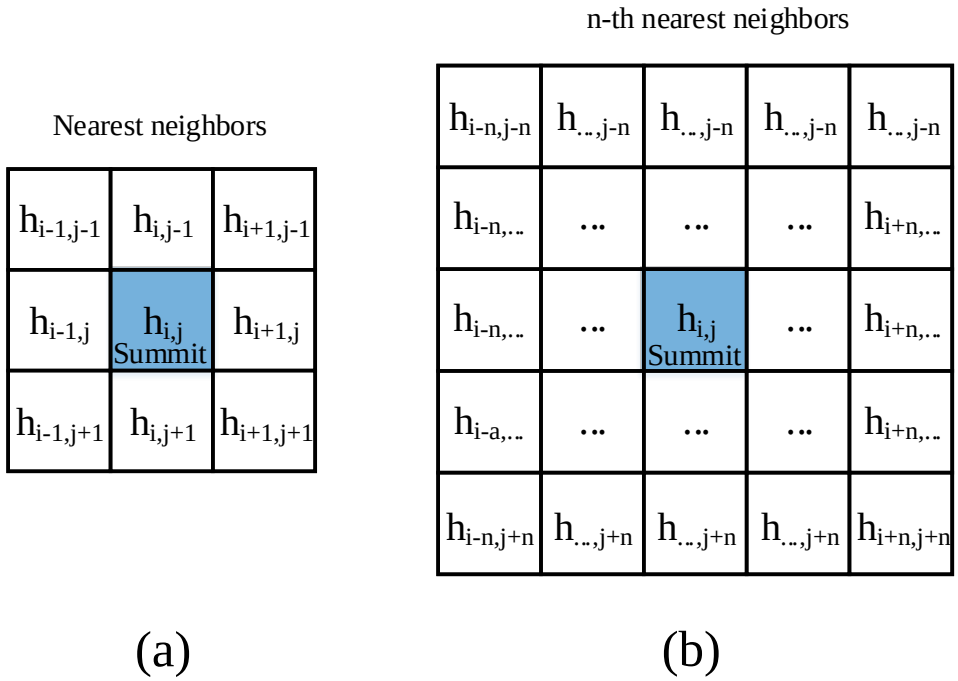

Fig. 2-10. Identification of summits on rough surface: (a) Nearest neighbors, and (b) n-th nearest neighbors

In Fig. 2-11, the white points represent the nearest summits (a), and the primary summits (b) considering the average wavelength of tool surface.

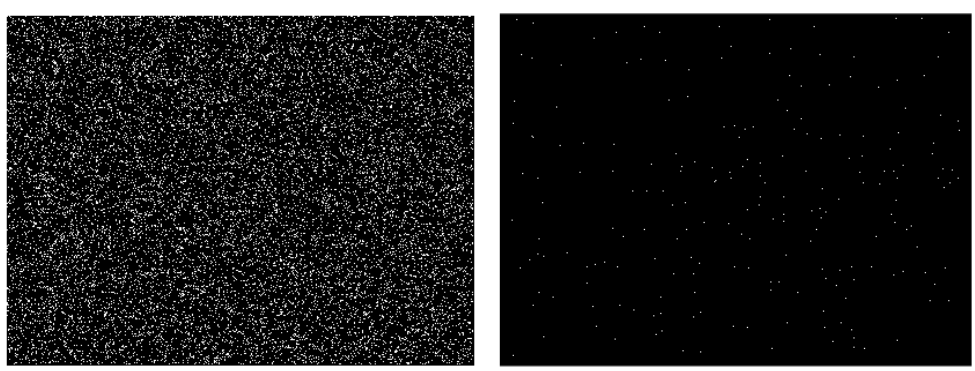

Fig. 2-11. Summit locations shown in white points: (a) summits determined by nearest neighbors, and (b) primary summits determined by average wavelength.

Now, it is possible to model the shape of each tool asperity with the position of primary summit and the contact area (Section 2.3.1) of the tool under the force equilibrium (Fig 2-12). The tool asperities penetrating into the workpiece have heights greater than δ_{tool}, and they are represented by the gray contact areas in Fig. 2-12 (a). The contact area, which shows the bottom of tool asperities penetrating workpiece, does not represent a single asperity, while several asperities are combined as shown in Fig. 2-12 (b). Therefore, multiple primary summits can exist within the contact area. The half of the minimum distances from one primary summit to the other one within the same contact area can be determined as the radius of tool asperity with the primary summit. Then, the area of each tool asperity is divided based on the determined radius, and the penetration height w of one tool asperity is obtained using Eq. (2-33) within this area.

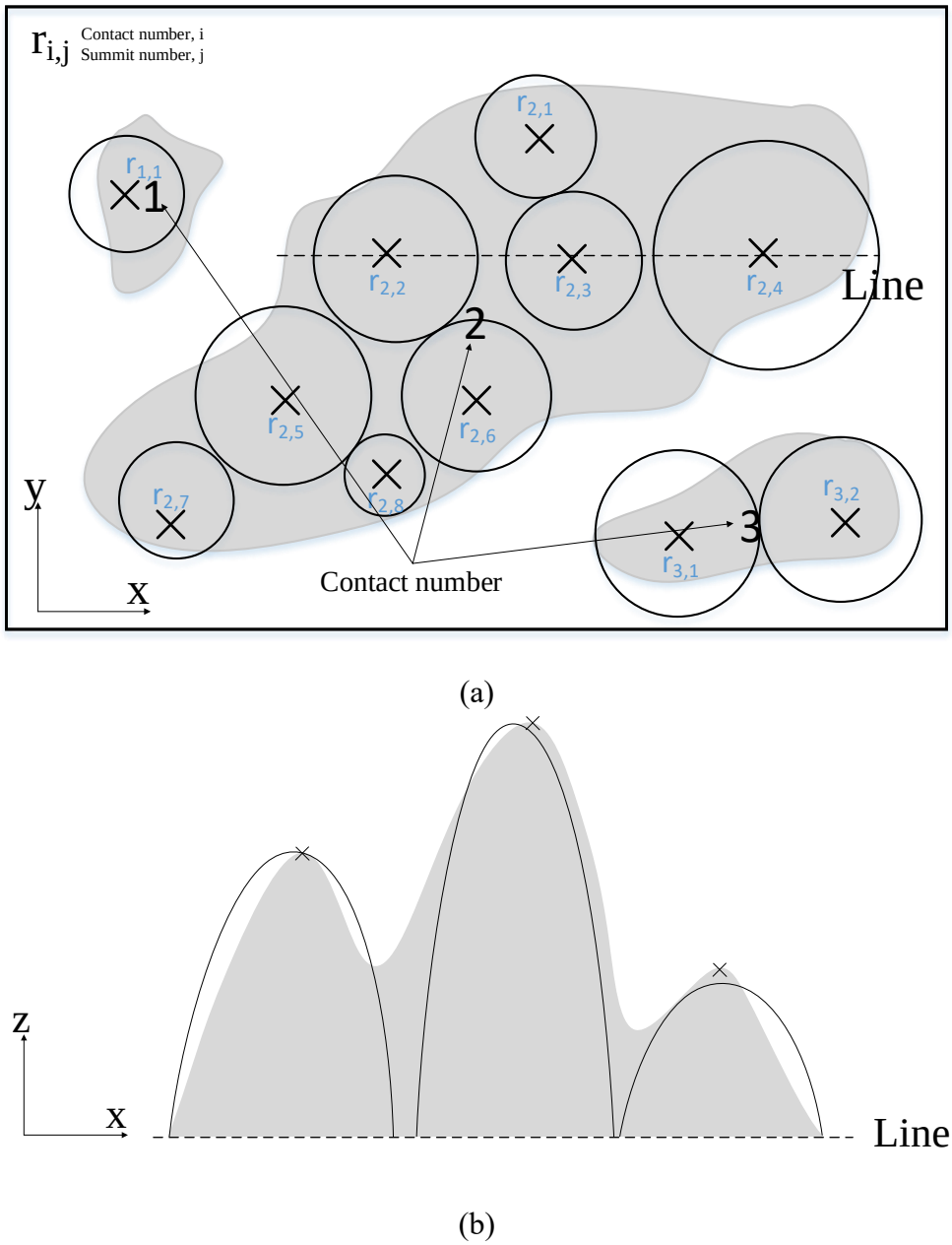

Fig. 2-12. Methodology for modeling each tool asperity: (a) different asperity identification methods inside one contact area in the xy plane, and (b) xz plane view based on the line shown in (a).

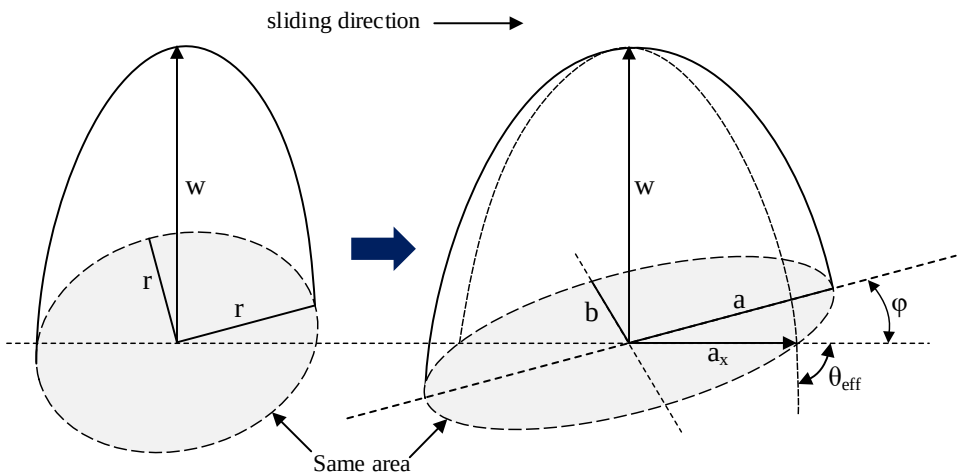

Fig. 2-13. Schematic view of transformation from a circular paraboloid to an elliptical paraboloid with the same contact area through image processing

By using image processing [109], the circular paraboloid can be transformed to an elliptical paraboloid with equal area (Fig. 2-13). In the figure, a_x is determined from Eq. (2.35). The friction coefficient of a single asperity can be calculated from Eq. (2.37) and Eq. (1.5). Since the total friction force is the sum of the friction forces exerted by all tool asperities, the friction coefficient can be finally obtained from the following equation.

$$\mu = \frac{F_w}{F_N} = \frac{\sum_{i=1}^{m} \mu_i(\theta_i) A_i H}{P_{nom} A_{nom}} \tag{2.43}$$

where m is the number of tool asperities, and μ_i is the friction coefficient of a single tool asperity.

3. Friction model in mixed-boundary lubrication

The mixed-boundary lubrication, which is also frequently employed lubrication condition in the sheet metal forming process, involves a mixed metal-metal contact and metal-lubricated area as shown in the Fig. 3-1. Unlike the boundary lubrication condition, hydrodynamic pressure is generated from lubricating contact in the opposite direction of the applied normal force, which reduces the metal-to-metal contact, thereby decreases the friction. In this case, a multiphysics approach is required to simultaneously consider the contact pressure due to the metal-metal contact and the hydrodynamic pressure by lubrication at the micro-scale. However, establishing the frictional behavior of mixed boundary lubrication is very challenging because the frictional behavior is complicated and numerically inefficient due to the change of the contact boundary conditions during sliding. In this study, therefore, the friction model for the mixed boundary lubrication is based on the load-sharing concept as aforementioned in Section 1.3.2 is employed. First, in section 3.1 the mixed lubrication friction model proposed by Hol [106] is introduced. Section 3.2 describes the finite element (FE) modeling used to calculate the lubrication pressure of the average Reynolds equation. Section 3.3 calculates the hydrodynamic pressure and film thickness in the elastohydrodynamic lubrication (EHL) and comparison of analysis results with those from the commercial program COMSOL for

verifying the proposed FE modeling.

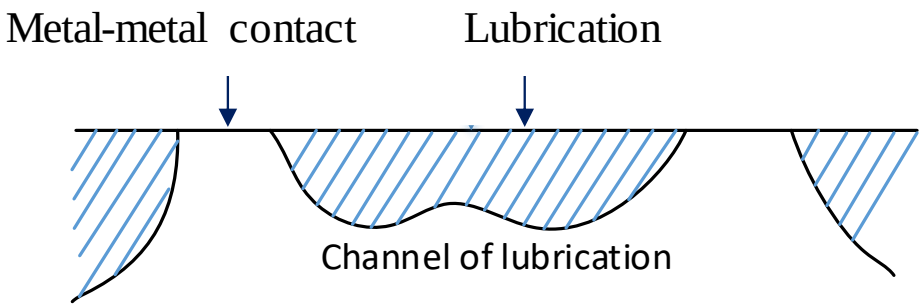

Fig. 3-1. Schematic illustration of microcontact under mixed-boundary lubrication condition

3.1. Overview of the mixed-boundary friction model (Hol [106])

Basic theoretical backgrounds on the fluid film lubrication behavior are essential for developing the friction modeling of mixed boundary lubrication. From Section 1.3.2, the averaged Reynolds equation in Eq. (1.10) and the viscouse shear stress in Eq. (1.12) are used in this study. Hol[106] implemented the hydrodynamic behavior as a lubrication interface element with additional degree of freedom for pressure in the finite element code. And, the friction coefficient was calculated using the new methodology combined with the boundary lubrication friction model as shown in Fig. 3-2.

Since the mixed-boundary lubrication friction model is implemented in FE scheme, all variables (μ , h , v_1 , v_2 , p_{nom} , p_{sol} , p_{lub} , d , U , α , τ_{sol} , τ_{lub} , τ_{total}) except lubrication viscosity η are nodal variables. Among the initial variables, h_{ini} is the initial surface roughness profile, and μ_0 is a constant value. The value h_{ini} is determined from the profile of initial workpiece surface, and μ_0 is a constant value. The nominal contact pressure p_{nom} is calculated within the FE code via a penalty contact algorithm. The hydrodynamic pressure p_{lub} is calculated by solving the average Reynolds equation (Eq. (1.10)) through the film thickness h and velocity v_1, v_2 in the previous increment (Section 3.2). The detailed FE procedure is discussed in section 3.2, which solves the average Reynolds equation. The shear stress of

film lubrication τ_{lub} is calculated using p_{lub} and Eq. (1.12). The solid contact pressure p_{sol} is expressed as $p_{sol} = p_{nom} - p_{\text{lub}}$ by the load sharing concept. The shear stress τ_{sol} and lubrication film thickness h are calculated in the boundary lubrication friction model with p_{sol} and the nodal strain in FE simulation (Section 2).

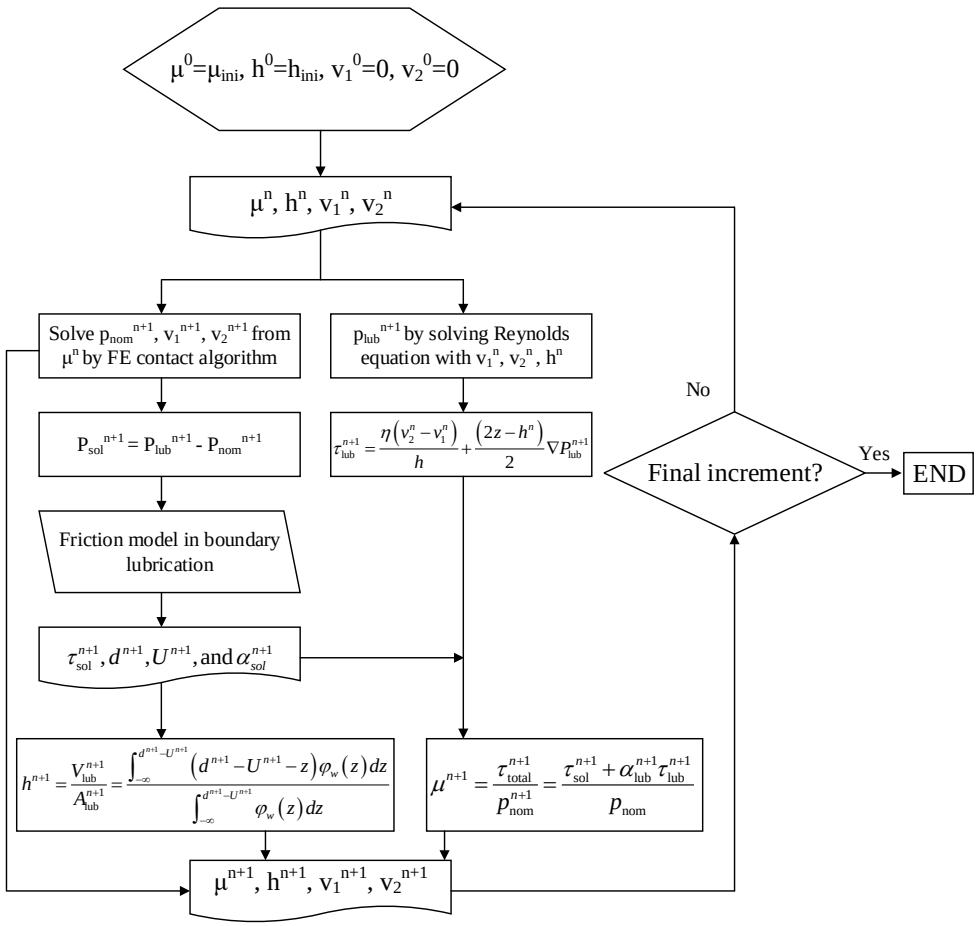

Fig. 3-2. Flow chart of mixed-boundary lubrication friction model proposed by Hol [106]

The lubrication film thickness h is derived from non-contact pockets filled with lubrication, excluding metal-to-metal contact areas. The total lubrication volume is the sum of the values obtained from multiplying the empty length $d-z-U$ of each asperity by the unit area ΔA of single asperity. Here, only the non-contact asperities are considered.

$$V_{\text{lub}} = \Delta A \sum_{i=1}^{N^{**}} \left(d_i - z_i - U_i \right) \tag{3.1}$$

where d is the equilibrium height, and U is height of rise. The d and U values are given from the micromechanical contact model introduced in section 2.2. Eq (3.1) is transformed into a stochastic form as follows:

$$V_{\text{lub}} = A_{nom} \int_{-\infty}^{d-U} \left(d - U - z \right) \varphi_w \left(z \right) dz \tag{3.2}$$

The integral from $-\infty$ to $d-U$ represents the heights of asperities that are not in contact with the tool surface. Since the lubrication film area is the area excluding the real contact area (αA_{nom}) which was obtained in Section 2.2, it is written as follows:

$$A_{\text{lub}} = 1 - \alpha A_{nom} = A_{nom} \int_{-\infty}^{d-U} \varphi_w \left(z \right) dz \tag{3.3}$$

The film thickness h can be calculated by the load sharing concept in Fig. 1-2 along with Eqs (3.2) and (3.3). It is written as follows.

$$h = \frac{V_{\text{lub}}}{A_{\text{lub}}} = \frac{\int_{-\infty}^{d-U} (d - U - z)\varphi_w(z)\,dz}{\int_{-\infty}^{d-U} \varphi_w(z)\,dz} \tag{3.4}$$

The film thickness h as a nodal variable is calculated by p_{sol} determined from the position x, y in the contact area.

The total shear stress τ_{total} is calculated by the shear stress τ_{sol} between the metal-to-metal contact and the hydrodynamic shear stress τ_{lub} of film lubrication.

$$\tau_{total} = \tau_{sol} + \alpha_{\text{lub}}\tau_{\text{lub}} \tag{3.5}$$

The lubricant shear stress is calculated at the global level without taking into account the tool-workpiece contact as shown in Eq. (3.4). Therefore, in Eq. (3.5), α_{lub} is multiplied by τ_{lub} in consideration of the effect by the area of the film lubrication. On the other hand, τ_{sol} has already been considered at the local level (in Section 2). Finally, the total friction coefficient μ_{total} is obtained by dividing the nominal stress by the total shear stress.

$$\mu_{total} = \frac{\tau_{total}}{p_{nom}} \tag{3.6}$$

The calculated μ_{total}, h, v_1, v_2 values are updated for the next time increment in the iterative numerical scheme.

3.2. Finite element modeling for film fluid behavior

In order to solve the Reynolds equation describing the lubrication behavior, finite element model is developed in this study. Then, the hydrodynamic pressure p_{lub} can be obtained if the film thickness h is calculated from the boundary lubrication friction model. In the common sheet metal forming process (including the application process that will be introduced in Section 4.3), there is no strong variations in slip rate of the sheet, the influence of the slip rate differential term is neglected as shown in Eq. (1.10). The average Reynold equation (Eq. (1.10)) can be rewritten as a two-dimensional form as follows:

$$\begin{aligned}&\frac{\partial}{\partial x}\bullet\left(\frac{\rho h^3}{12\eta}\mathbf{\Phi}_{\mathbf{P}}\frac{\partial p_{\text{lub}}}{\partial x}\right)+\frac{\partial}{\partial y}\bullet\left(\frac{\rho h^3}{12\eta}\mathbf{\Phi}_{\mathbf{P}}\frac{\partial p_{\text{lub}}}{\partial y}\right)\\&=\frac{\left(v_1+v_2\right)}{2}\left(\frac{\partial\rho h}{\partial x}+\frac{S_q}{2}\left(v_1-v_2\right)\bullet\frac{\partial\mathbf{\Phi}_{\mathbf{S}}}{\partial x}\right)\end{aligned}\tag{3.7}$$

The squeeze term $\frac{\partial h}{\partial t}$ is not considered in the quation because it has minor effect in the sheet metal forming process [106]. The solution of the average Reynolds equation in a partial differential equation can be obtained using the standard finite element procedure. Then, the average Reynolds equation is first transformed to the following weak form by multiplying the trial function w_p.

$$\int_{\Omega_h}\left[\begin{array}{l}\dfrac{\partial w_p}{\partial x}\bullet\left(\dfrac{\rho h^3}{12\eta}\boldsymbol{\Phi}_{\mathbf{P}}\dfrac{\partial p_{\text{lub}}}{\partial x}\right)+\dfrac{\partial w_p}{\partial y}\bullet\left(\dfrac{\rho h^3}{12\eta}\boldsymbol{\Phi}_{\mathbf{P}}\dfrac{\partial p_{\text{lub}}}{\partial y}\right)\\ -\dfrac{(v_1+v_2)}{2}\left(\rho h\dfrac{\partial w_p}{\partial x}+\dfrac{S_q}{2}(v_1-v_2)\bullet\boldsymbol{\Phi}_{\mathbf{S}}\dfrac{\partial w_p}{\partial x}\right)\end{array}\right]d\Omega=0 \tag{3.8}$$

where Ω_h is the entire domain in which film lubrication exists.

The boundary integral term below

$$-\int_{\partial\Omega_h}\left[\left(\frac{\rho h^3}{12\eta}\boldsymbol{\Phi}_{\mathbf{P}}\frac{\partial p_{\text{lub}}}{\partial x}n_x+\frac{\rho h^3}{12\eta}\boldsymbol{\Phi}_{\mathbf{P}}\frac{\partial p_{\text{lub}}}{\partial y}n_y-\frac{(v_1+v_2)}{2}\left(\rho h+\frac{S_q}{2}(v_1-v_2)\bullet\boldsymbol{\Phi}_{\mathbf{S}}\right)n_x\right)w_p\right]d\Omega \tag{3.9}$$

is omitted by replacing the essential boundary condition (p_{lub} =0 at the boundary) with the equation representing the Dirichlet boundary condition. And, for the FE analysis the field variables h and p_{lub} are discretized using the second-order piecewise polynomial approximations.

$$\begin{cases} p_{\text{lub}}=\sum_{i=1}^{6}P_i^e N_{p,i} \\ h=\sum_{i=1}^{6}h_i^e N_{p,i}\end{cases} \tag{3.10}$$

where $N_{p,i}$ is the 2D second-order Lagrange shape function corresponding to a 6-node triangular element. In Eq. (3.8), the Galerkin method is used by replacing the trial function w_p with the shape function $N_{p,i}$. Since the Reynolds equation is non-linear, it requires numerical iterations by applying the Newton-Raphson method. The following equation represents the overall

assembled matrix system at Newton iteration n of the Reynolds equation.

$$\left[K_p\right]^{(n-1)}\left[dp_{\text{lub}}\right]^n = -\left[R_p\right]^{(n-1)} \tag{3.11}$$

with

$$\begin{aligned} &K_p\left(B_h(e,i), B_h(e,j)\right) += K_p^e(i,j) \\ &= \int_{\partial\Omega_e} \left[\begin{array}{l} \dfrac{\rho\left(h_i^e N_{p,i}\right)^3}{12\eta}\dfrac{\partial N_{p,i}}{\partial x}\dfrac{\partial N_{p,j}}{\partial x}\mathbf{\Phi_P} \\ +\dfrac{\rho\left(h_i^e N_{p,i}\right)^3}{12\eta}\dfrac{\partial N_{p,i}}{\partial y}\dfrac{\partial N_{p,j}}{\partial y}\mathbf{\Phi_P} \end{array} \right] d\Omega \end{aligned} \tag{3.12}$$

$$\begin{aligned} &R_p\left(B_{h(e,i)}\right) += R_p^e(i) \\ &= \int_{\partial\Omega_e} \left[\begin{array}{l} \dfrac{\rho\left(h_i^e N_{p,i}\right)^3}{12\eta}\dfrac{\partial p_{\text{lub}}}{\partial x}\dfrac{\partial N_{p,i}}{\partial x}\mathbf{\Phi_P} \\ +\dfrac{\rho\left(h_i^e N_{p,i}\right)^3}{12\eta}\dfrac{\partial p_{\text{lub}}}{\partial y}\dfrac{\partial N_{p,i}}{\partial y}\mathbf{\Phi_P} \\ -\dfrac{(v_1+v_2)}{2}\left(\rho\left(h_i^e N_{p,i}\right)\dfrac{\partial N_{p,i}}{\partial x}+\dfrac{S_q}{2}(v_1-v_2)\bullet\mathbf{\Phi_S}\dfrac{\partial N_{p,i}}{\partial x}\right) \end{array} \right] d\Omega \end{aligned} \tag{3.13}$$

$\mathbf{B_h}$ is the connectivity matrix in a triangular element composed of 6 nodes as follows:

$$
\begin{array}{c}
\qquad\qquad P\,dof\,\# \\
\qquad 1 \quad 2 \quad 3 \quad 4 \quad 5 \quad 6 \\
\qquad \downarrow \quad \downarrow \quad \downarrow \quad \downarrow \quad \downarrow \quad \downarrow \\
\left[B_h\right] = \begin{bmatrix}
\times & \times & \times & \times & \times & \times \\
\times & \times & \times & \times & \times & \times \\
\vdots & \vdots & \vdots & \vdots & \vdots & \vdots \\
\times & \times & \times & \times & \times & \times \\
\vdots & \vdots & \vdots & \vdots & \vdots & \vdots \\
\times & \times & \times & \times & \times & \times
\end{bmatrix}
\begin{array}{l}
\leftarrow Element\,1 \\
\leftarrow Element\,2 \\
\vdots \\
\leftarrow Element\,i \\
\vdots \\
\leftarrow Element\,n_e
\end{array}
\end{array}
\tag{3.14}
$$

$$
\int_{\Omega_e} \begin{bmatrix}
\dfrac{\partial N_{p,i}}{\partial x} \bullet \left(\dfrac{\rho \left(h_i^e N_{p,i} \right)^3}{12\eta} \boldsymbol{\Phi}_{\mathbf{P}} \dfrac{\partial p_{\mathrm{lub}}}{\partial x} \right) + \dfrac{\partial N_{p,i}}{\partial y} \bullet \left(\dfrac{\rho \left(h_i^e N_{p,i} \right)^3}{12\eta} \boldsymbol{\Phi}_{\mathbf{P}} \dfrac{\partial p_{\mathrm{lub}}}{\partial y} \right) \\
-\dfrac{\left(v_1 + v_2 \right)}{2} \left(\rho h_i^e N_{p,i} \dfrac{\partial N_{p,i}}{\partial x} + \dfrac{S_q}{2} \left(v_1 - v_2 \right) \bullet \boldsymbol{\Phi}_{\mathbf{S}} \dfrac{\partial N_{p,i}}{\partial x} \right)
\end{bmatrix} d\Omega = 0
$$

In this thesis, the overall FE procedure such as linearization using the shape function, assembling of element, and solution procedure to derive the overall assembled matrix, is omitted.

3.3. Verification of the developed finite element modeling

The implementation of the FE modeling shown in Section 3.2 is verified by two methods. First, the hydrodynamic pressures are compared with the results from the commercial FE program COMSOL describing fluid behavior. The software can not only describe the behavior of fluids, but also perform the multiphysics analysis. Fig. 3-3(a) and (c) show the two different film thickness profiels, and Fig. 3-3 (b) and (d) compare the hydrodynamic contact pressures when the fluid flows in the positive x direction. As for the boundary conditions, the pressure at the inlet and outlet is the same as atmospheric pressure, and there is no change in the film thickness. Also, the same lubrication viscosity and flow rate are applied to each analysis method. Note that the contact pressure profiles in Fig. 3-3 (b) and (d) are identitical between the two software, which successfully validates the robust implementation of the developed FE modeling in this study.

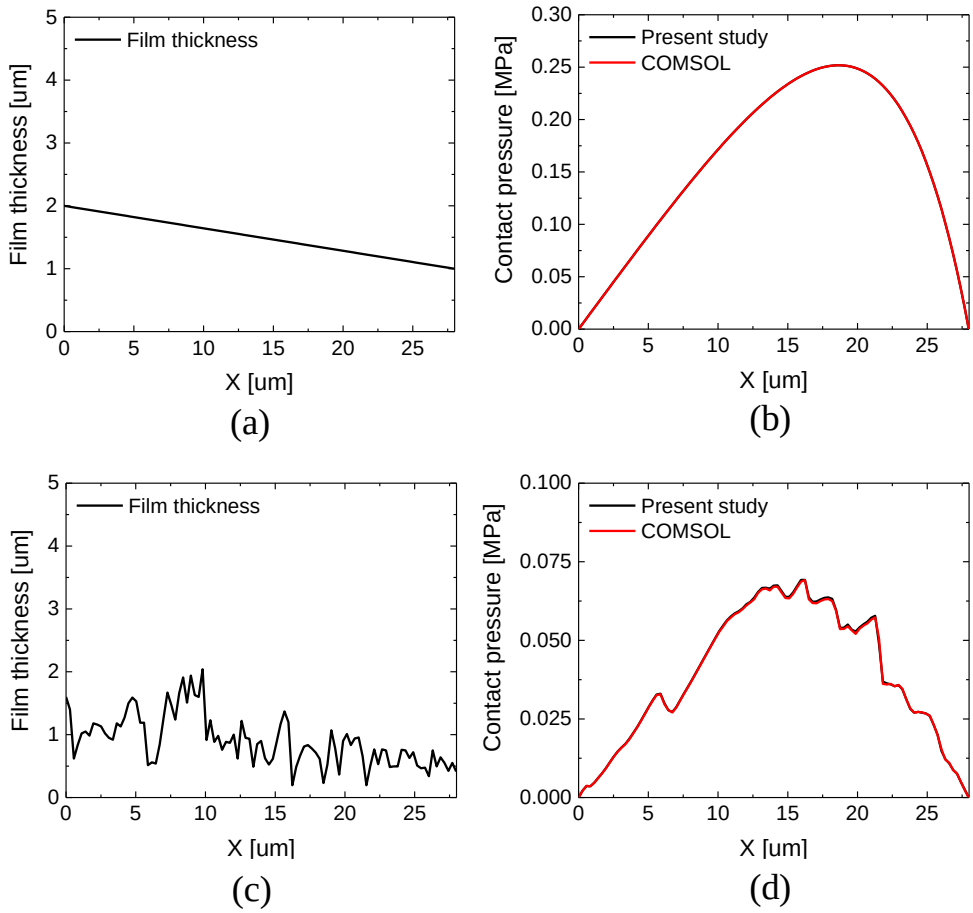

Fig. 3-3. Comparison of hydrodynamic pressures (b,d) calculated by the FE code developed in the present study and the commercial software COMSOL for two different film thickness profiles (a,c)

As a second validation, the hydrodynamic pressure and film thickness are calculated in the EHL region where the effect of lubrication is most dominant in the Stribeck curve (Fig. 1-2). High viscosity lubricant is used to prevent the metal-to-metal contact between gears and bearings, and the lubrication conditions satisfy the EHL condition. The high hydrodynamic pressure generated by the flow of high-viscosity lubrication elastically deforms the

metal surface as shown in Fig. 3-4. In addition, the elastically deformed surface in turn affects the film thickness and hydrodynamic pressure. To solve this EHL problem, the multiphysics analysis, which combines the elastic deformation behavior, fluid equation (or Reynolds equation), and force equilibrium equation, is required. Habachi [110] solved the EHL problem with a fully coupled multiphysics FE approach. The dimensionless Reynolds equation, the linear elasticity constitutive equation, and the force equilibrium equation are:

$$\frac{\partial}{\partial X}\left(\varepsilon\frac{\partial P}{\partial X}\right)-\frac{\partial\left(\bar{\rho}H\right)}{\partial X}=0 \tag{3.15}$$

$$\nabla\bullet\left(\mathbf{C}\nabla\mathbf{U}\right)=0 \tag{3.16}$$

$$\int_{\Omega_C} P d\Omega=\frac{\pi}{2} \tag{3.17}$$

with dimensionless hydrodynamic pressure P, dimensionless film thickness H, the stiffness tensor $\mathbf{C}$, dimensionless displacement tensor $\mathbf{U}$, and dimensionless variables and parameters:

$$\begin{aligned}&\varepsilon=\frac{\bar{\rho}H^3}{\bar{\mu}\lambda},\lambda=\frac{12U_m\mu_0R^2}{a^3p_h},U_m=\frac{u_1+u_2}{2},R=\frac{r_1r_2}{r_1+r_2}\\&P=\frac{p}{p_h},H=\frac{hR}{a^2},X=\frac{x}{a},\bar{\rho}=\frac{\rho}{\rho_0},\bar{\mu}=\frac{\mu}{\mu_0}\end{aligned} \tag{3.18}$$

where u_1, u_2 are the velocity of each object, r_1, r_2 are the radius of each

object, p_h is a Hertzian pressure, a is the contact length, ρ is the density of the fluid, and μ is the lubrication viscosity. The mesh geometry required for the FE approach is shown in Fig. 3-5, where the elastic deformation behavior is calculated in the domain Ω and the hydrodynamic pressure and film thickness are calculated in the domain Ω_C. For fully coupling and improved computational convenience, the two domains Ω and Ω_C are constructed from the same elements. The following equation is a fully coupled overall assembled matrix:

$$\begin{bmatrix} [T_{hh}] & [T_{he}] & [T_{hl}] \\ [T_{eh}] & [T_{ee}] & \{\Phi\} \\ [T_{lh}] & \{\Phi\} & 0 \end{bmatrix}^{(k-1)} \begin{bmatrix} \{\delta P\} \\ \{\delta H\} \\ \{\delta H_0\} \end{bmatrix}^{(k)} = \begin{bmatrix} \{R_h\} \\ \{R_e\} \\ \{R_l\} \end{bmatrix}^{(k)} \tag{3.19}$$

The detailed formulas are included in Appendix. The hydrodynamic pressure and film thickness calculated through the convergence of Eq. 3.19 are compared according to the lubrication viscosity in Fig. 3-6. The higher the lubrication viscosity, the greater the elastic deformation and the overall film thickness increases. In addition, the film thickness variation near the outlet is large, thus the hydrodynamic pressure spike is higher. The calculated results in Fig. 3-6 by the implemented EHL problem using the developed FE model are in good agreements with other published results. Therefore, it is verified that the lubrication behavior can be successfully simulated using the proposed FE modeling.

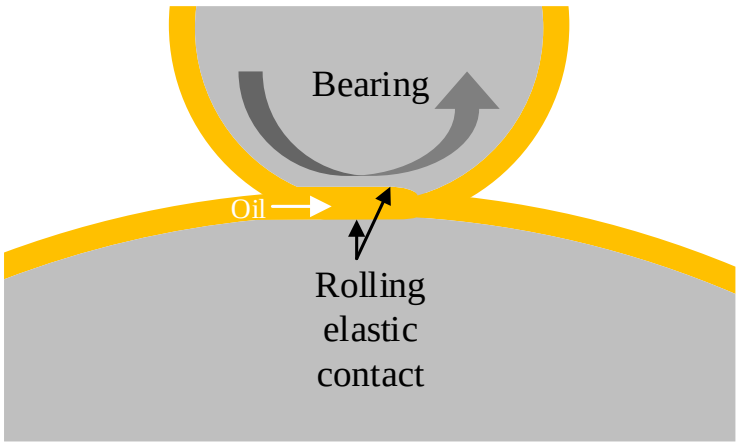

Fig. 3-4. Schematic view of EHL phenomenon caused by rotation of spheres with different radii under high viscosity lubrication between the two contacting objects

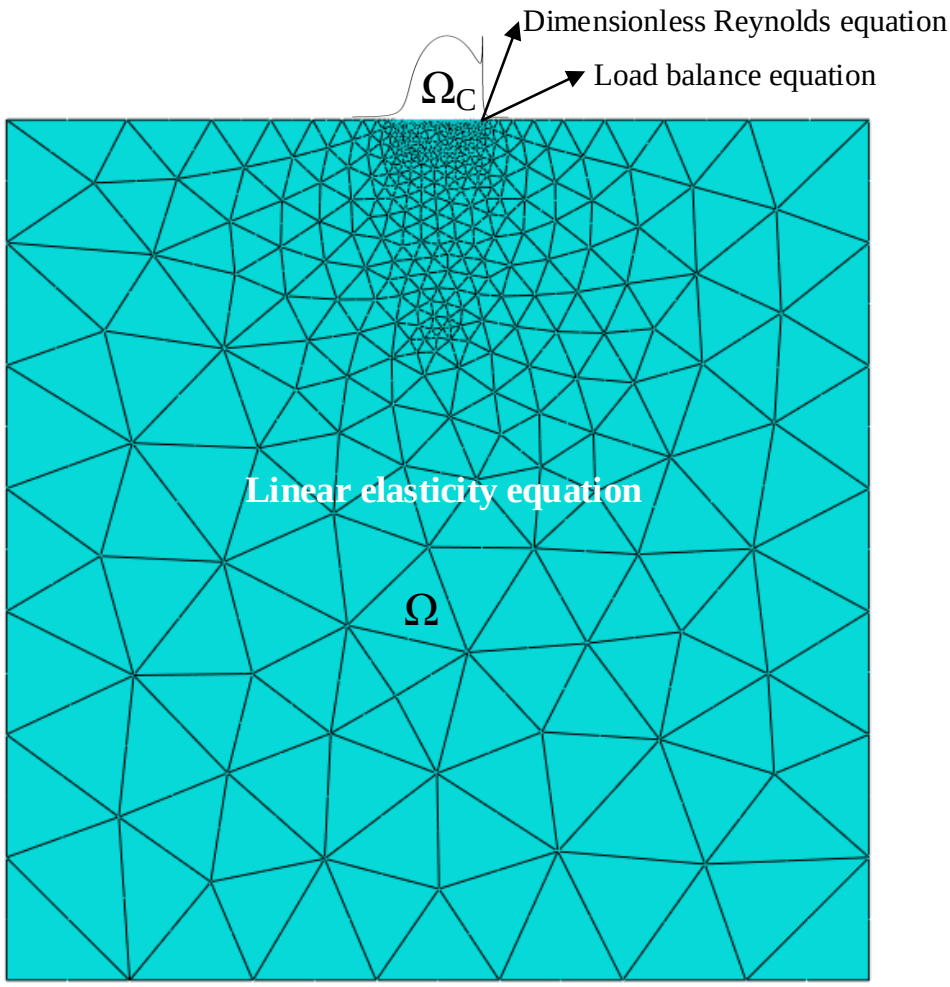

Fig. 3-5. Finite element model used in the EHL problem and the domain where the elastic deformation is calculated, and the domain where the lubrication behavior is calculated

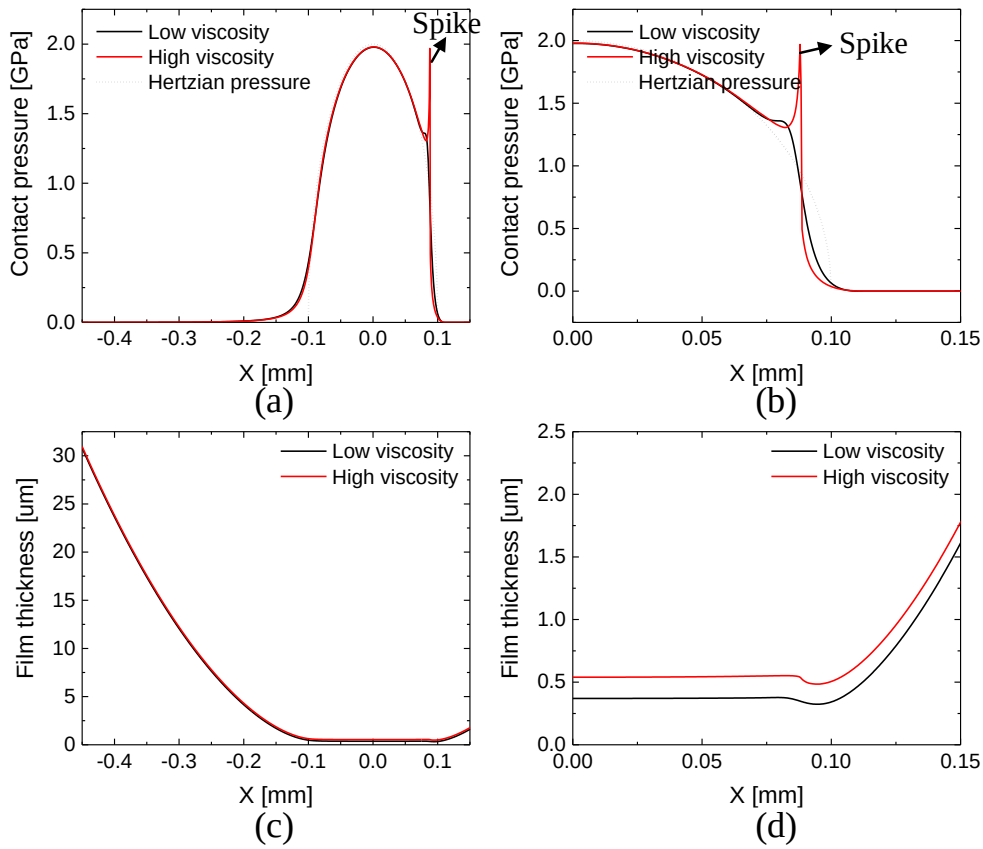

Fig. 3-6. Comparison of hydrodynamic pressure and film thickness for high-viscosity and low-viscosity lubrication conditions: (a) hydrodynamic pressure in the full contact area, (b) hydrodynamic pressure in the enlarged area, (c) film thickness in the full contact area, and (d) film thickness in the enlarged area

4. Application of boundary lubrication and mixed-boundary lubrication friction model to sheet metal forming process

4.1. Friction model parameters

4.1.1. Material properties

In this study, two sheet metals, TRIP780 and CP1470, are selected and applied to the industrial sheet metal forming processes for investigating the validity of the proposed friction modeling. Table 4.1 shows the hardening parameters (Eq. (2.4)) of the workpiece materials for obtaining the real contact area of the contact models in Section 2.2.

Table 4.1. Hardening parameters of Eq. (2.4) for TRIP780 and CP1470

Material	R	K [MPa]	ε_0	n	σ_s [MPa]	σ_y [MPa]	c
TRIP780	0.73	1398	0.013	0.17	908	0	0.05
CP1470	0.6	2000	9.86×10^{-4}	0.059	1605	1363	0.0059

The parameters in Table 4.1 are applied to the friction model for predicting the friction coefficients, and the material model is applied differently in the finite element applications (Section 4.2). The detailed constitutive parameters of the elasticity and plasticity modeling employed in the FE simulations of sheet metal forming processes are provided in Appendix.

4.1.2. Surface data

The surface roughness data of the workpiece and tool were measured with 3D laser scanning microscopy (3D confocal microscopy). Post-processing were required for accurate surface height measurement because abnormal spikes were observed as typical noises included in the height data. These noise data were removed with noise filtering processing. The type of median filter was used in this study by referring to the previous studies [80]. The median filter operation selectively removes the noises with abnormal heights that deviate significantly from the neighboring heights [111]. The parameters of the noise filter are the range of neighbors and the number of executions. In this study, the generally recommended values of 3x3 in size (pixel size) and 2 executions were adopted. Additional possible error in the surface data can be imperfect specimen alignment, which leads to the artificial curvature of the surface. Therefore, the tilted surface needed to be corrected to obtain a flat surface. The measured 3D surfaces of the workpiece and tool after the post-processing are shown in Fig. 4-1 for the investigated materials. The reference measurement size and resolution were chosen based on values recommended in previous study [80]. Table 4.2 lists the root mean square (RMS) height values of each workpiece and tool.

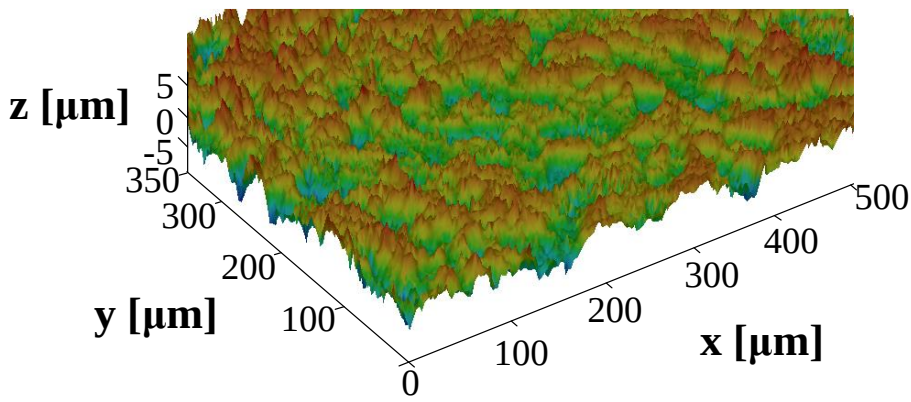
z [µm]
5
0
-5
350
300
200
y [µm]
100
0
100
200
300
400
500
x [µm]

(a)

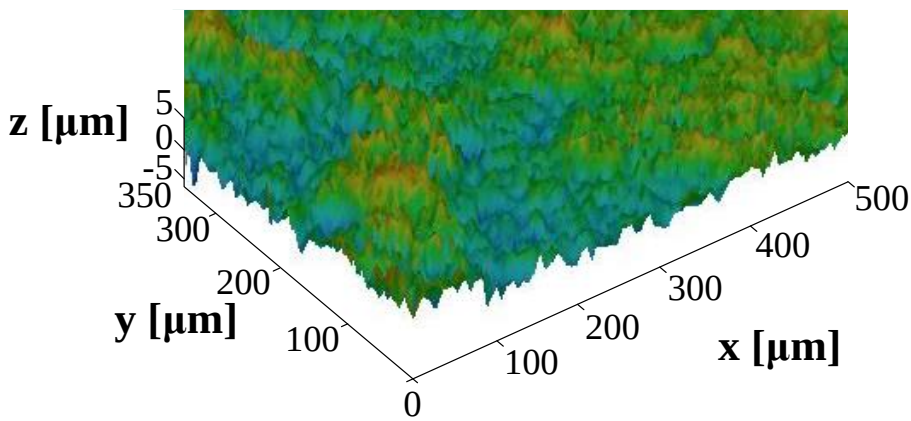
z [µm]
5
0
-5
350
300
200
y [µm]
100
0
100
200
300
400
500
x [µm]

(b)

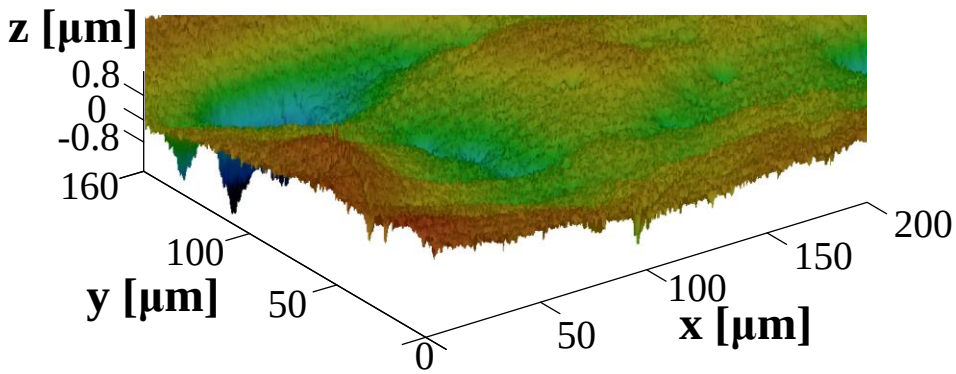
z [µm]
0.8
0
-0.8
160
100
y [µm]
50
0
50
100
150
200
x [µm]

(c)

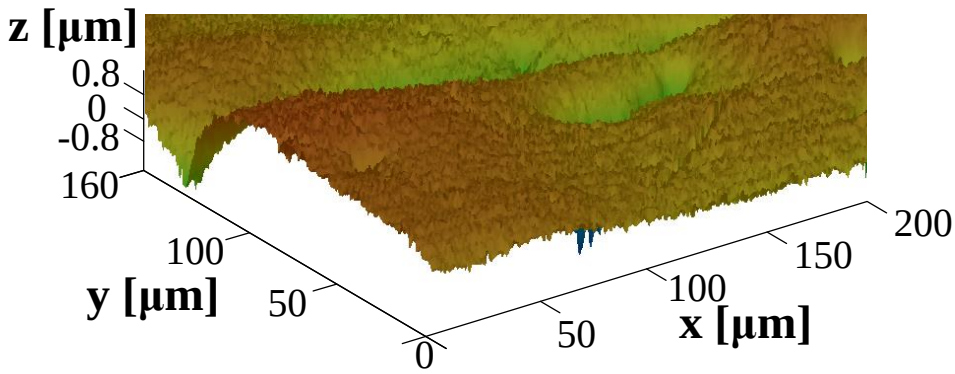

(d)

Fig. 4-1. The measured 3D surface profiles: (a) TRIP780, (b) CP1470, (c) tool surface in contact with TRIP780, and (d) tool surface in contact with CP1470

Table 4.2. Root mean square (RMS) heights from the measured 3D surface profiles

Material	TRIP780	CP1470	Tool 1	Tool 2
Root mean square height [µm]	1.165	0.810	0.104	0.111

4.1.3. Friction experiments

This section presents friction experimental procedure, which will be used to validate the developed friction model by comparing the friction coefficients between experiment and modeling. The friction coefficients were differently obtained for the two investigated materials. The friction coefficient of the TRIP780 material was referred to the reference paper [112]. On the other hand, the friction coefficient of CP1470 sheet was measured with a specially designed friction tester shown in Fig. 4-2. The friction tester consists of hydraulic grip and normal force actuator (a,b), specimen jig (c) etc. And, the specimen used for the test is shown in (d). The horizontal main loading system controls the compressive-tensile deformation of the specimen, while the vertical force system applies a normal force to the jigs placed over the specimen. The jigs and vertical force system are designed to prevent buckling of the specimen during compressive loading. However, due to the friction between the jigs and the specimen caused by the normal force and sliding, accurate material properties are obtained after correcting friction. Since this compression-tension measuring instrument is similar to the friction coefficient measuring system, the new jigs and specimens were designed on the same equipment as in Fig. 4-3 for measuring friction coefficient. The geometry of friction specimen was modified to grip in one direction to avoid material deformation. Localized contact was required to obtain high enough

contact pressure due to the the attainable level of normal force. Therefore, the contact area was reduced by designing a jig same as the specimen width, which allowed the measurement of friction coefficient at the contact pressure up to 200 MPa. As the specimen slides, friction occurs not only on the top surface of the specimen but also on the bottom surface as shown in Fig 4-3 (d). A Teflon™ sheet was used between the specimen and the lower jig to minimize the friction on the bottom surface and to measure the stable friction. The friction coefficient of the Teflon™ sheet can be measured, thus the friction coefficient of the investigated specimen μ is corrected and expressed as:

$$\mu = \frac{F_{Frictional\ force} - \mu_{Teflon} \cdot F_{Normal}}{F_{Normal}} \tag{4.1}$$

where μ_{Teflon} is the friction coefficient of Teflon sheet, F_{Normal} is the normal force, and $F_{Frictional\ force}$ is the measured friction force in the main horizontal load cell.

In Fig. 4-4, the friction coefficient measured through the friction tester and the friction coefficient predicted by the developed friction model are compared for the two materials.

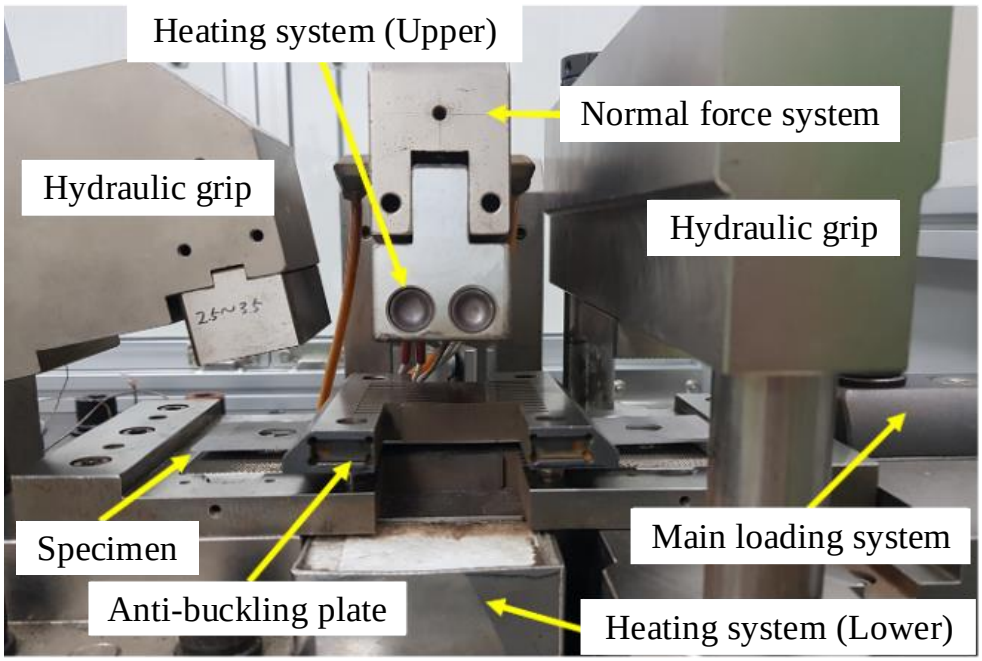

(a)

(b)

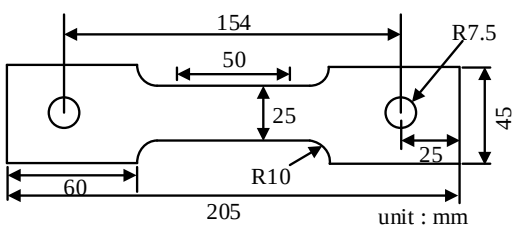

(c)

Fig. 4-2. Figures of the compression-tension test equipment: (a) equipment components, (b) the shape of the jigs, (c) the geometrical information of the specimen

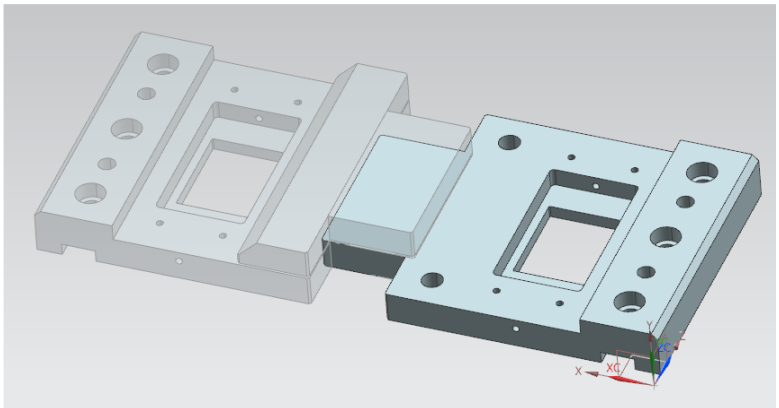

(a)

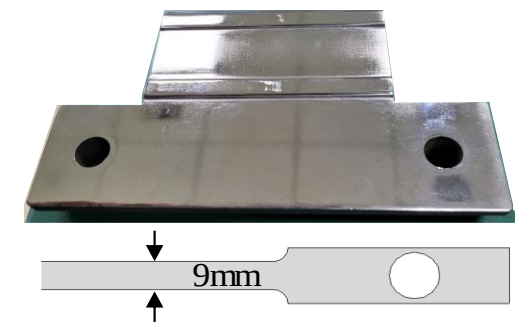

(b)

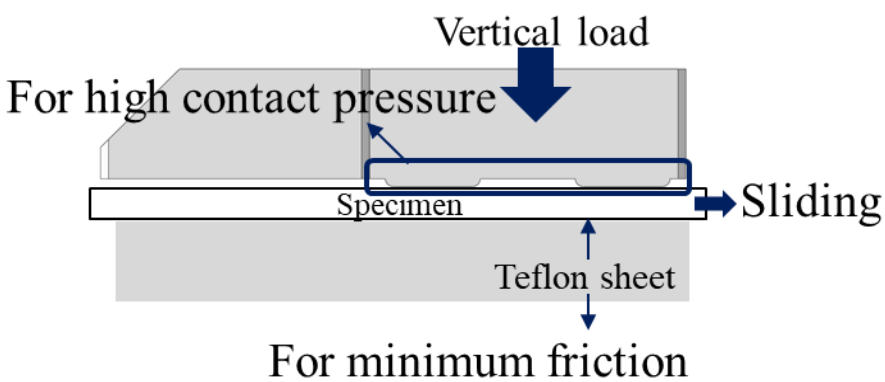

(c)

Fig. 4-3. Friction measurement experiment conducted by designing new jigs in the existing compression-tension test equipment: (a) newly designed jigs shape, (b) contact concentration for large contact pressure, (c) schematic view of friction test

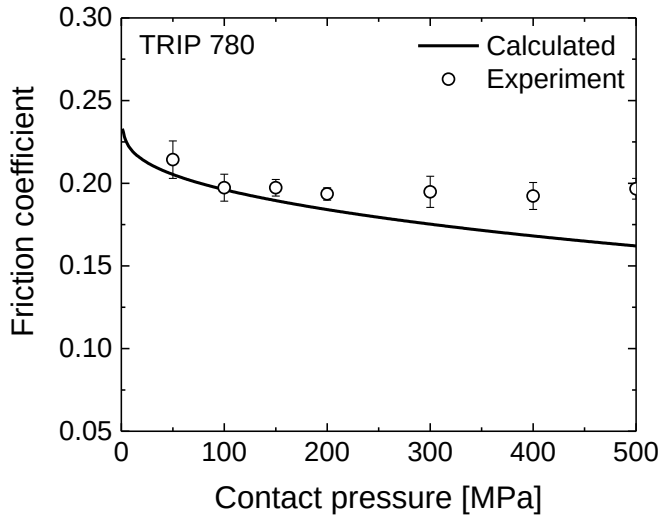

(a)

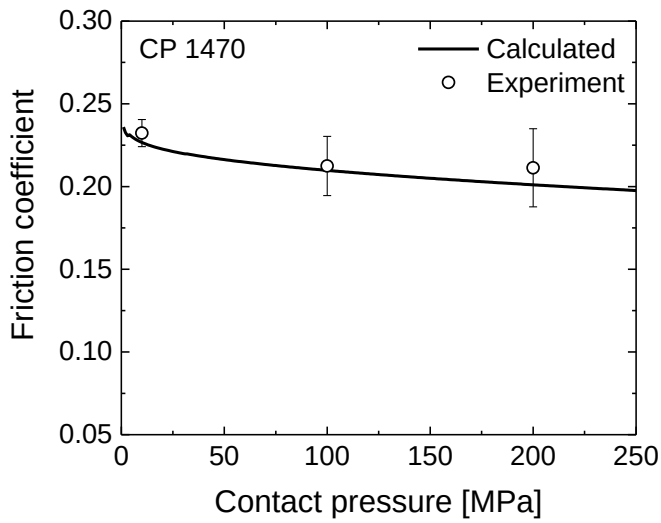

(b)

Fig. 4-4. Comparison of friction coefficient measured in friction test and friction coefficient calculated in boundary lubrication friction model: (a) TRIP780, (b) CP1470

4.2. Application to sheet metal forming processes under non-lubrication conditions

Two sheet metal forming processes, (1) U-drawing bending and (2) a newly developed press-forming (Fig. 4-5), are used to validate the developed friction model and finite element modeling for the boundary lubrication. The newly proposed press forming process consists of three processes: (1) drawing and forming process of the sheet material provided from coiled steel stack, (2) cutting process when the formed sheet reaches the target standard, and (3) dimensional correction process. After cutting, the processes are repeated, which results in a continuous forming process.

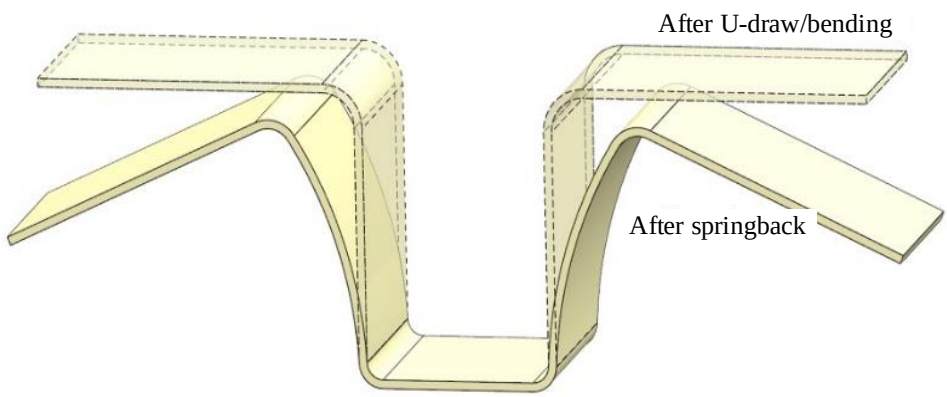

(a)

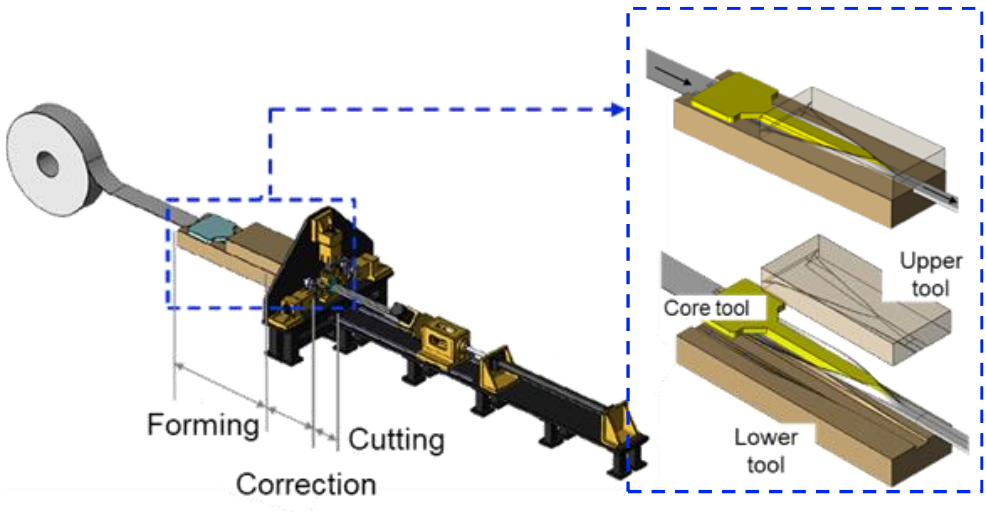

(b)

Fig. 4-5. Schematic figures of sheet metal forming processes for friction model verification: (a) U-draw/bending and springback, (b) newly developed press-forming

The FE models for both sheet metal forming processes were constructed using commercial FE software ABAQUS/Standard. For the friction, the boundary lubrication friction model was applied to the FE simulation using the user subroutine FRIC supplemented in the ABAQUS. The Lagrange multiplier (Fig. 4-6 (a)) and penalty (Fig. 4-6 (b)) methods are commonly used for numerical implementations of friction behavior. By using the Lagrange method, it provides an accurate solution to the slip-stick behavior by strictly judging the bonding boundary condition. The penalty method approximates the stick with elastic stiffness that allows for small elastic slip (typically 0.005). The Lagrange method tends to hinder convergence as well as increase the computational time by reducing the convergence rate in the

Newton's method, especially when slip and stick states are repeated. In contrast, the penalty method approximates the stick with elastic behavior which allows small elastic slip, providing both efficiency and accuracy in typical sheet metal forming processes. Therefore, in this study the penalty method was employed for all FE simulations.

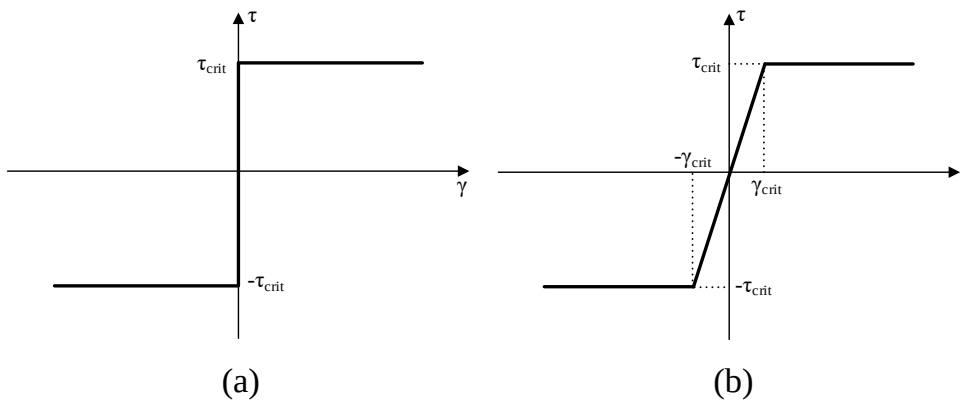

Fig. 4-6. Contact mechanisms: (a) Lagrange and (b) penalty methods

The contact pressure on the specimen surface and the equivalent plastic strain of the specimen vary with time increment in the sheet metal forming simulations. For the FE implementation of the boundary lubrication friction model, an appropriate friction coefficient in consideration of the contact pressure and equivalent plastic strain should be evolved. A fully coupled FE model, which calculates the friction coefficient at every node of the specimen as a function of the contact condition at each time increment, is computationally too much expensive. A more numerically efficient strategy

is to use a friction coefficient matrix constructed according to the uniform spacing of the contact pressure and equivalent plastic strain. By implementing the friction coefficient matrix as input information of the FE model, the friction coefficient can be interpolated as a function of the contact pressure and strain on each node to provide the appropriate friction coefficient to the FE simulation.

4.2.1. Application to U-draw/bending simulation

The geometry of the tools used in the U-drawing/bending tests was provided from the Numisheet'93 benchmark problem (Fig. 4-7). The sheet material is the TRIP780 steel with a thickness of 1.2 mm. The specimen has a size of 350 mm (RD)*45 mm (TD). The tool material is AISI D2 (SKD11), and the tool surface is Cr-plated. As the lubricant, an anti-rust oil with a dynamic viscosity of 2.9 cSt was used, and no additional lubricant was added. Two blank holding force conditions were used - 20kN and 70kN. The total punch movement was 70 mm and with a speed of 1m/s. The springback and punch force of the U-drawing/bending tests can be referred to the referenced paper [112]

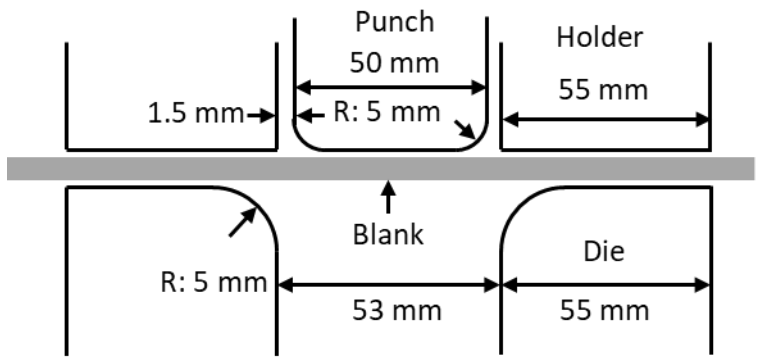

Fig. 4-7. U-draw/bending tool geometrical dimensions

The blank sheet was meshed with 4-node shell elements with a reduced integration (S4R), which is the same as the reference paper. Considering the deformation mode in the referred paper, a plane strain condition was applied in the simulation. The tool was modeled with an analytical rigid surface.

For comparing the effect of friction models in the FE simulation, the same constitutive model of TRIP780 steel was used for all U-drawing/bending simualtions. For elasticity model, the Chord modulus model[113, 114], in which the elastic modulus changes as a function of equivalent plastic strain, was used. For plasticity, the Yld2000-2d [3] for the non-quadratic anisotropic yield function and a homogeneous yield function-based anisotropic hardening (HAH) model [115] for hardening were used.

In the FE simulations of U-drawing/bending, two proposed friction models were applied.

• Friction model 1, which considers the effect of contact pressure only.

• Friction model 2, which considers the effects of both contact pressure and equivalent plastic strain.

Additionally, simulations with constant friction coefficients of 0.2 and 0.15, which are typical values in the sheet metal forming processes, were also compared.

Fig. 4-8 shows the FE predicted and experimentally measured punch force-displacement curves for two different blank holding forces. The figures present that the predicted results by the proposed friction models give more accurate than the those of the constant friction coefficient model. The difference between the two approaches becomes clearer in the case of 70kN blank holding force. Fig. 4-9 shows the FE predicted springback profiles and their comparisons with experimental data. For quantitative analysis of the springback, the two angles theta1, theta2, and sidewall curl as springback parameters are shown in Fig. 4-10. Fig. 4-11 shows the comparisons of the quantitative springback parameters. Note that the friction models 1 and 2 accurately predicted both springback and punch forces, while constant friction models under- or over-estimated dependeing on the constant value. This accuracy is more pronounced for 70 kN blank holding force (15.6 MPa contact pressure at blank holding region) than for the 20 kN holding force (4 MPa contact pressure at blank holding region) due to the magnitude of the

contact pressure. Therefore, the predictive capability of the proposed friction modeling is explained based on the case with 70 kN blank holding force.

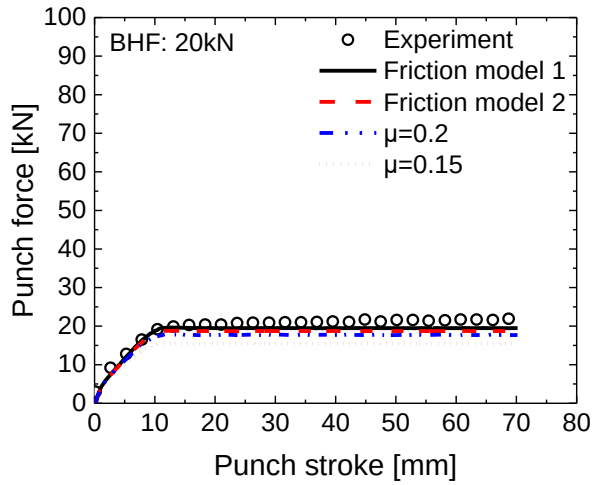

(a)

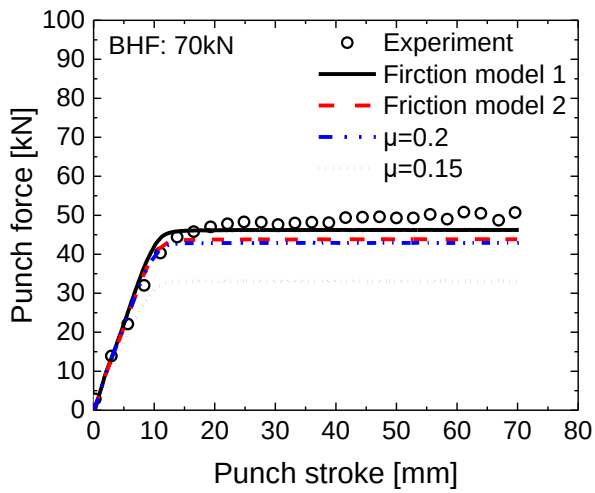

(b)

Fig. 4-8. Comparison of punch force-displacement obtained by experimental datas and FE simulations of friction models at blank holding forces of (a)20 kN and (b)70 kN

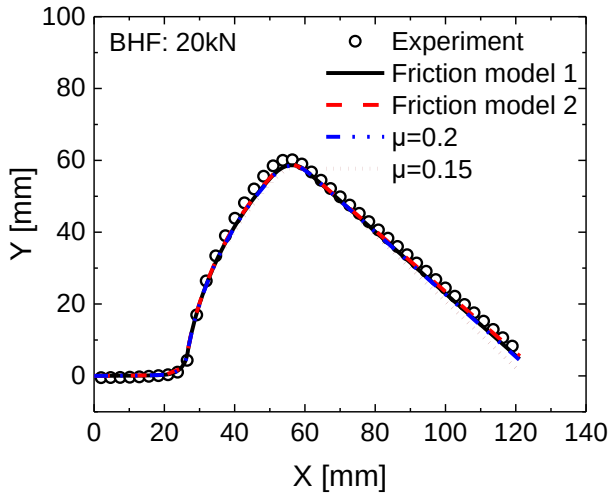

(a)

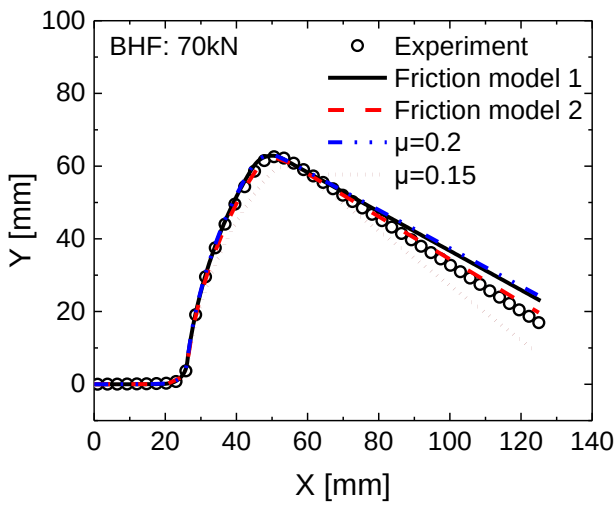

(b)

Fig. 4-9. Comparison of profiles after the springback obtained by experimental datas and FE simulations of friction models at blank holding forces of (a) 20 kN and (b) 70 kN

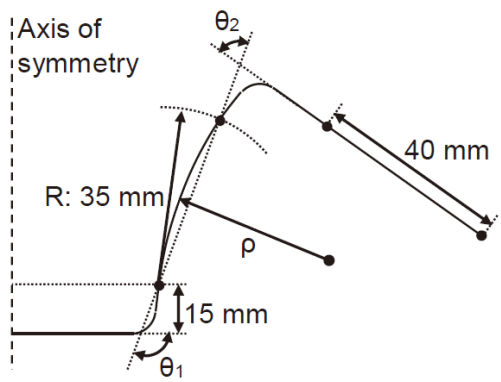

Fig. 4-10. Definition of springback parameters for U-draw/bending

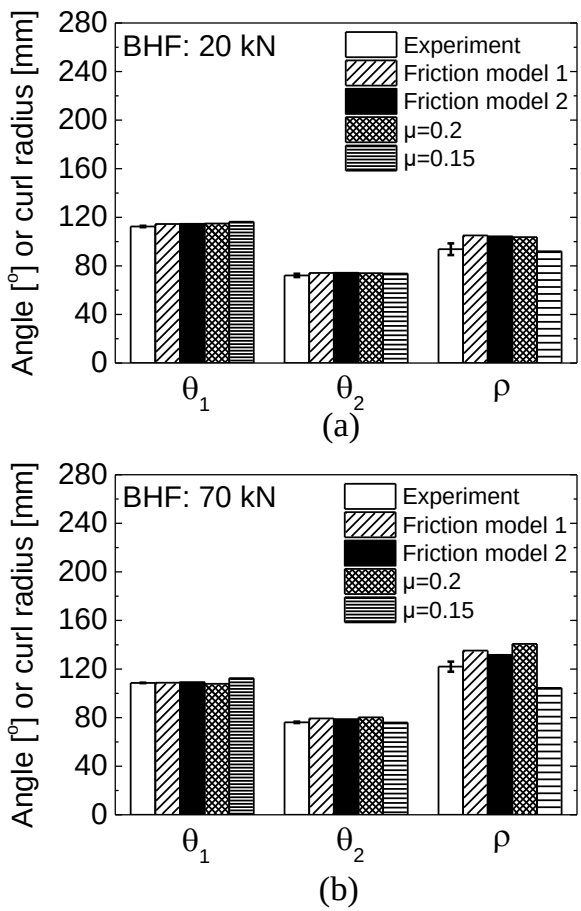

Fig. 4-11. Comparison of springback parameters obtained by experimental datas and FE simulations of friction models at blank holding forces of (a) 20 kN and (b) 70 kN

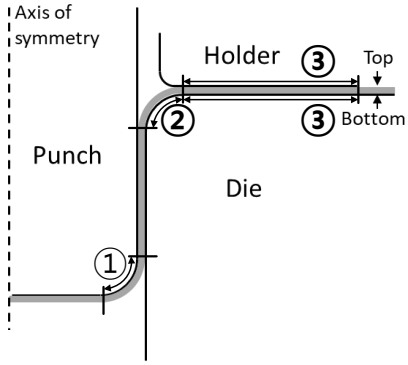

(a)

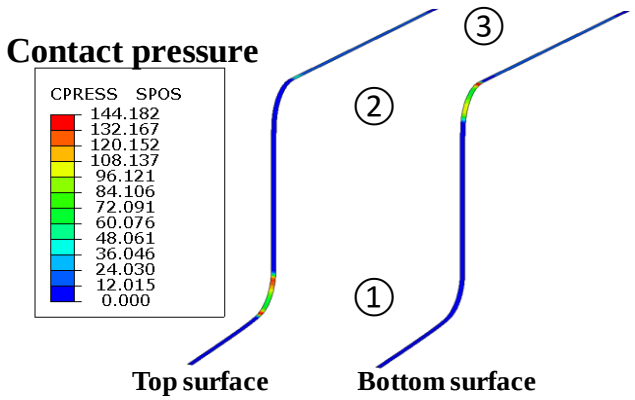

(b)

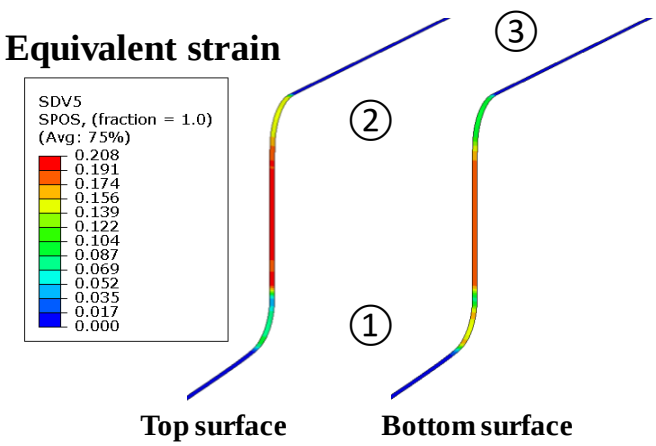

(c)

Fig. 4-12. Contact regions divided into three types (a) in U-draw/bending process, (b) the contact pressure distribution on the top and bottom surfaces, (c) the equivaslent strain distribution on the top and bottom surfaces

In the U-drawing process, the contact is largely divided into 3 contact regions as shown in the Fig 4-12. The first contact region is the zone between the punch and upper surface of the specimen, where the contact pressure is high, but little sliding of the specimen. The second contact region is located between the bottom surface of the specimen and the curved side of the die, where the specimen is bent and unbent. The last contact region represents the contacts between top surface of the specimen and blank, and between the bottom surface of the specimen and die surface.

Fig. 4-13 shows the FE calculated history of contact pressure and equivalent plastic strain on the bottom surface of one workpiece element. The friction coefficients calculated based on the friction models 1 and 2 at this contact pressure and equivalent plastic strain are shown in Fig. 4-13 (b). Since the equivalent plastic strain is zero in the contact region 1, the friction models 1 and 2 in contact region 1 provides the same friction coefficient. In contact region 2, the friction coefficients by friction models 1 and 2 are lower than those of the contact region 1 due to the high contact pressure. In addition, the friction coefficient by the friction model 2 is lower than that by the friction model 1 due to the bulk strain effect caused by the deformation of the sheet. In contact region 2, this difference in friction coefficient has a significant influence on the springback and punch force. The punch force depends on the the deformation hardening of the material and the frictional force generated

in the contact regions 2 and 3. Because only the friction coefficients calculated from the friction models 1 and 2, where the coefficients are variable, are different in the contact area 2, the punch force calculated based on the friction model 2 is lower than that of friction model 1. Similarly, the springback predictions of friction models 1 and 2 differ as shown in Fig. 4-13 (b) due to the difference in the friction coefficients in the contact region 2.

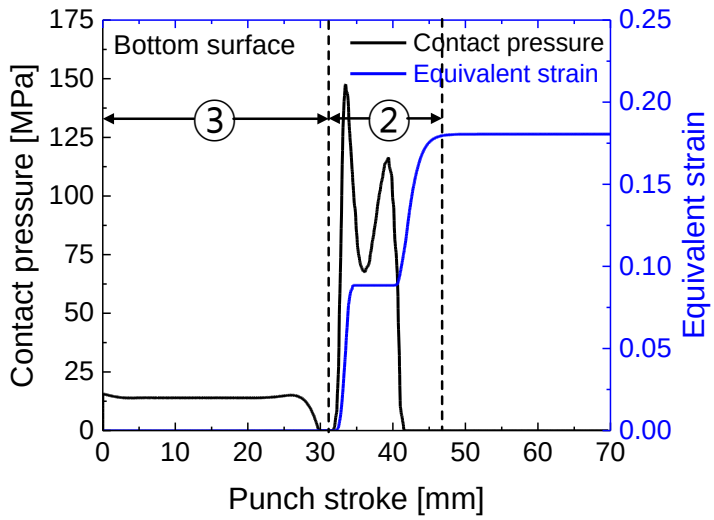

(a)

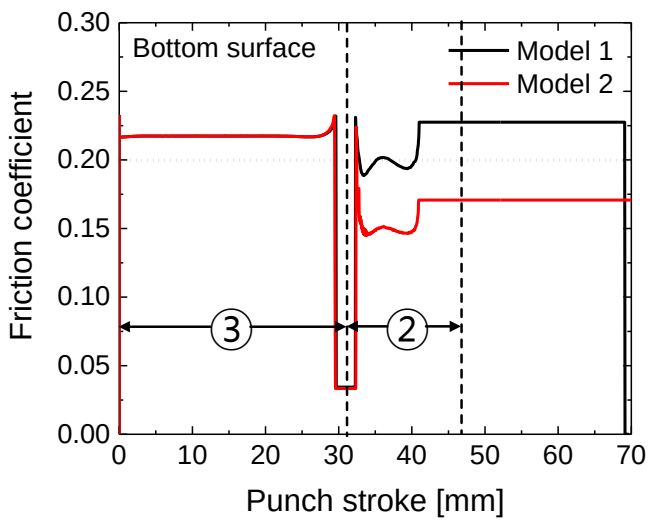

(b)

Fig. 4-13. History of contact pressure and equivalent strain (a) and friction coefficient (b) on the bottom surface of a single element according to U-draw/bending process

4.2.2. Application to prototype press-forming process without lubricant

For verifying the developed boundary lubrication friction model, the finite element simulation with a novel prototype press-forming process (Fig. 4-5(b)) was conducted. Fig. 4-14 shows the graphical illustration of the prototype press-forming equipment. As shown in Fig. 4-14, each tool is fastened with screws, and a sheet metal is deformed by pulling the front part of the sheet in a non-lubricated state. In the FE simulation, the tools were modeled with rigid surfaces as shown in Fig. 4-15(a) for computational efficiency. Fig. 4-15(b) shows the FE model with the tools and sheets assembled before the prototype press-forming process. The tools are fixed in all directions and forming proceeds as the sheet is pulled in the forming direction. Fig. 4-15(c) shows the FE model during the press-forming process and the sheet after cutting and springback. For the reference material, CP1470 with a thickness of 1.2 mm was used. The speed of the forming was 40 mm/s. The workpiece element was modeled with 4-node shell elements with the reduced integration (S4R). Only half of the sheet was used by considering the symmetry of the forming tool (Fig. 4-15 shows the simulation result by applying the mirror symmetry).

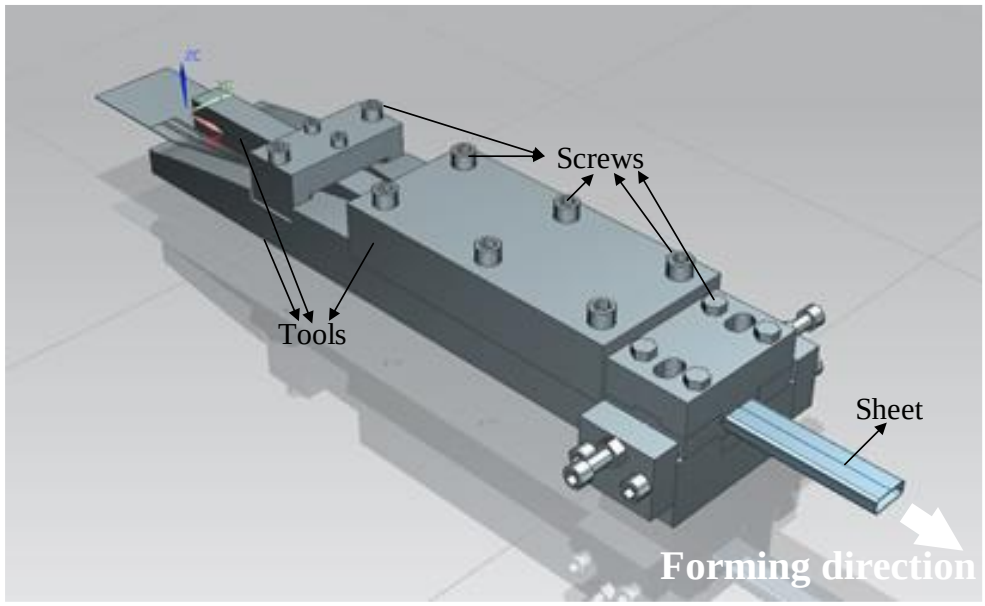

Fig. 4-14. Prototype forming machine which is newly developed under press-forming scheme

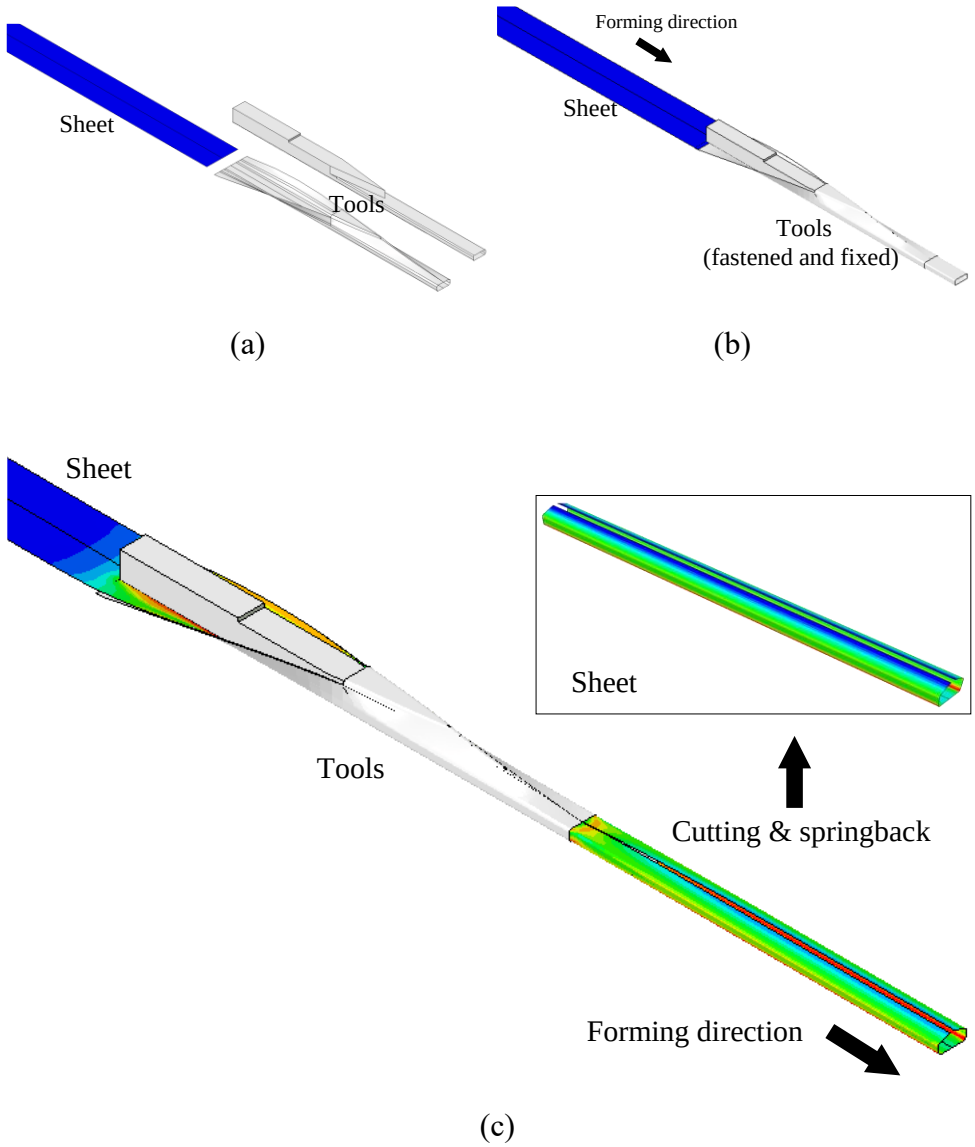

Fig. 4-15. Finite element model of the the prototype press-forming process: (a) Parts composing the FE model (Tools converted to rigid surfaces for numerical efficiency), (b) FE model with all component parts assembled before press-forming, (c) FE model during press-forming process and the sheet after cutting and springback

For measuring the plastic mechanical properties of the CP1470, uniaxial tension test and cyclic uniaxial tension-compression tests were conducted as shown in Fig. 4-16. In particular, the tension-compression test was included to measure the effect of the Bauschinger effect on flow stress of CP1470 sheet. In terms of the hardening model of the CP1470, the isotropic-kinematic hardening was considered in the FE model for representing the Bauschinger effect. Additionally, the classical isotropic hardening was also compared with the kinematic hardening. As for the yield function, the isotropic von Mises yield criterion was assumed for all simulations.

Fig. 4-17 presents the concept of the isotropic hardening and kinematic hardening. For the isotropic-kinematic hardening, the Chaboche type nonlinear kinematic hardening model was used, which is written as follows [116, 117].

$$\begin{cases} \sigma^0 = \sigma_0 + Q_\infty \left(1 - \exp\left(-b\bar{\varepsilon}^{pl}\right)\right) \\ \dot{\boldsymbol{\alpha}}_{\mathbf{k}} = C_k \dot{\bar{\varepsilon}}^{pl} \dfrac{1}{\sigma_0}\left(\boldsymbol{\sigma} - \boldsymbol{\alpha}\right) - \gamma_k \boldsymbol{\alpha}_k \dot{\bar{\varepsilon}}^{pl} \\ \boldsymbol{\alpha} = \sum_{k=1}^{N(=2)} \boldsymbol{\alpha}_k \end{cases} \tag{4.2}$$

The isotropic and kinematic hardening parameters could be identitifed from fitting the cyclic tension-compression curves, which are given in Table. 4-3.

To validate the material hardening model employed in this study, the

geometry of the formed part after press-forming was compared between the two different hardening models. Fig. 4-18 shows almost negligible difference in springback after removing the tools after forming. The result can be explained by investigating the strain path of a single element at the lower corner region in Fig 4-19. Although CP1470 material exhibits the Bauschinger effect, as indicated in Fig 4-16 (b), the variation of strain path during forming is insignificant (Fig 4-19), thus the two hardening by different hardening models gave almost identitical result. Therefore, other simulations were conducted by applying the isotropic hardening due to the small differene from the kinematic hardening.

Table 4.3. Isotropic and kinematic hardening parameters of CP1470 sheet

	σ^0[MPa]	Q_∞[MPa]	b	$C_{k,1}$[MPa]	$\gamma_{k,1}$	$C_{k,2}$[MPa]	$\gamma_{k,2}$
CP 1470	1200	177.6	1137	47282.7	168.5	1902.1	0.2

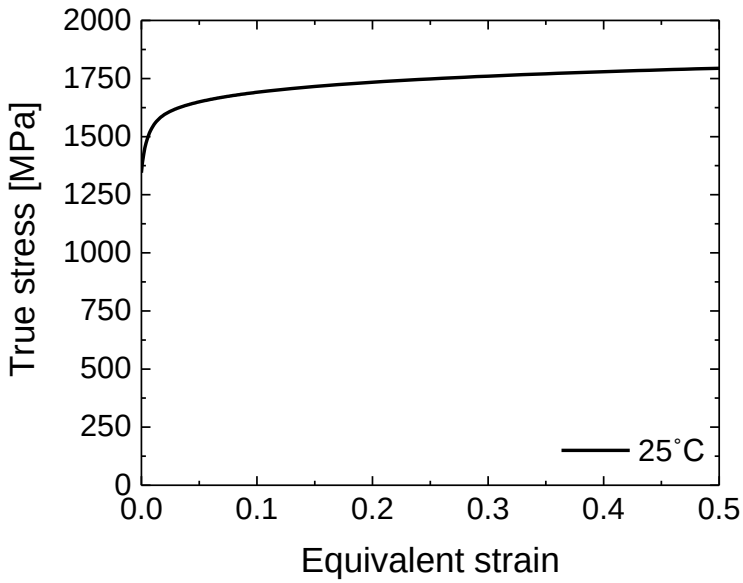

(a)

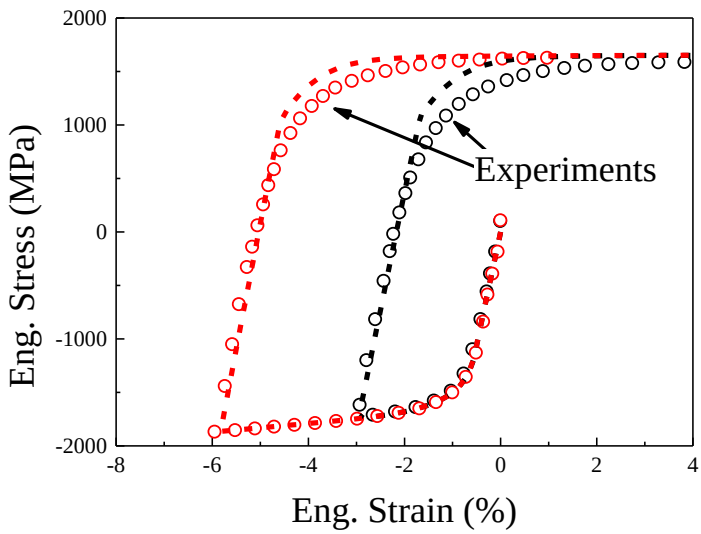

(b)

Fig. 4-16. Uniaxial tension test (a) and compression-tension test (b) of CP 1470

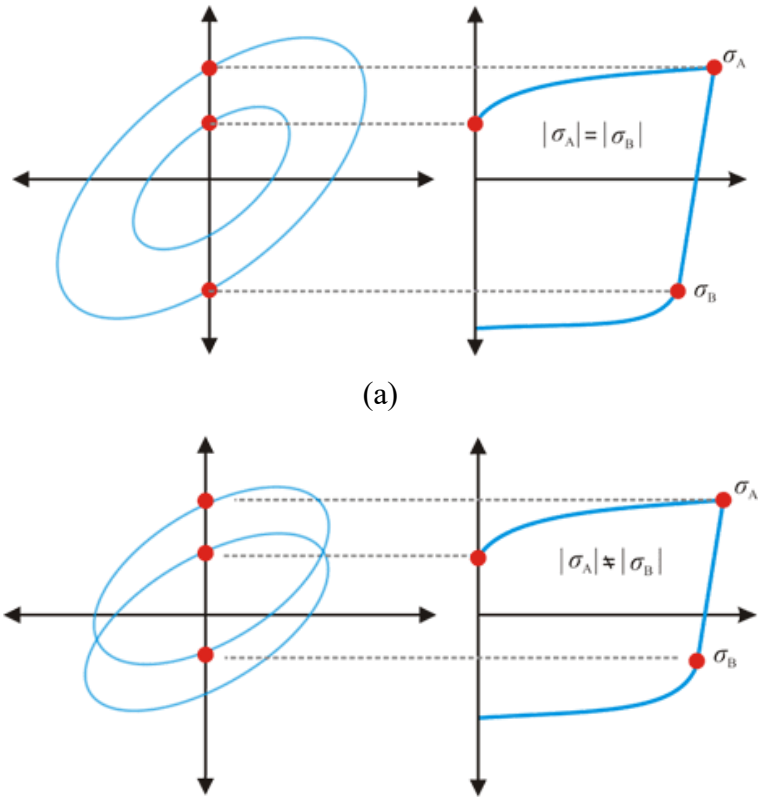

Fig. 4-17. Schematic description of (a) isotropic and (b) kinematic hardening model

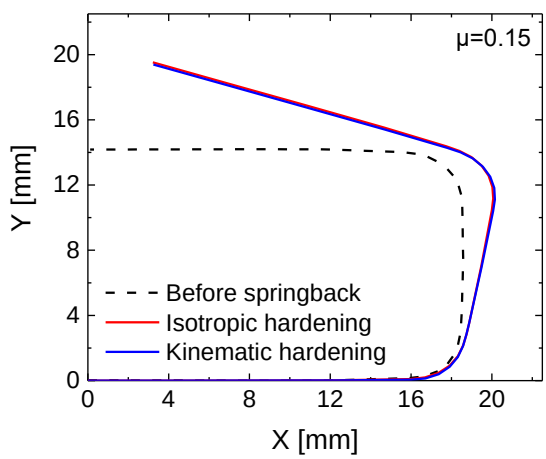

Fig. 4-18. Comparison of FE results between isotropic hardening and kinematic hardening model

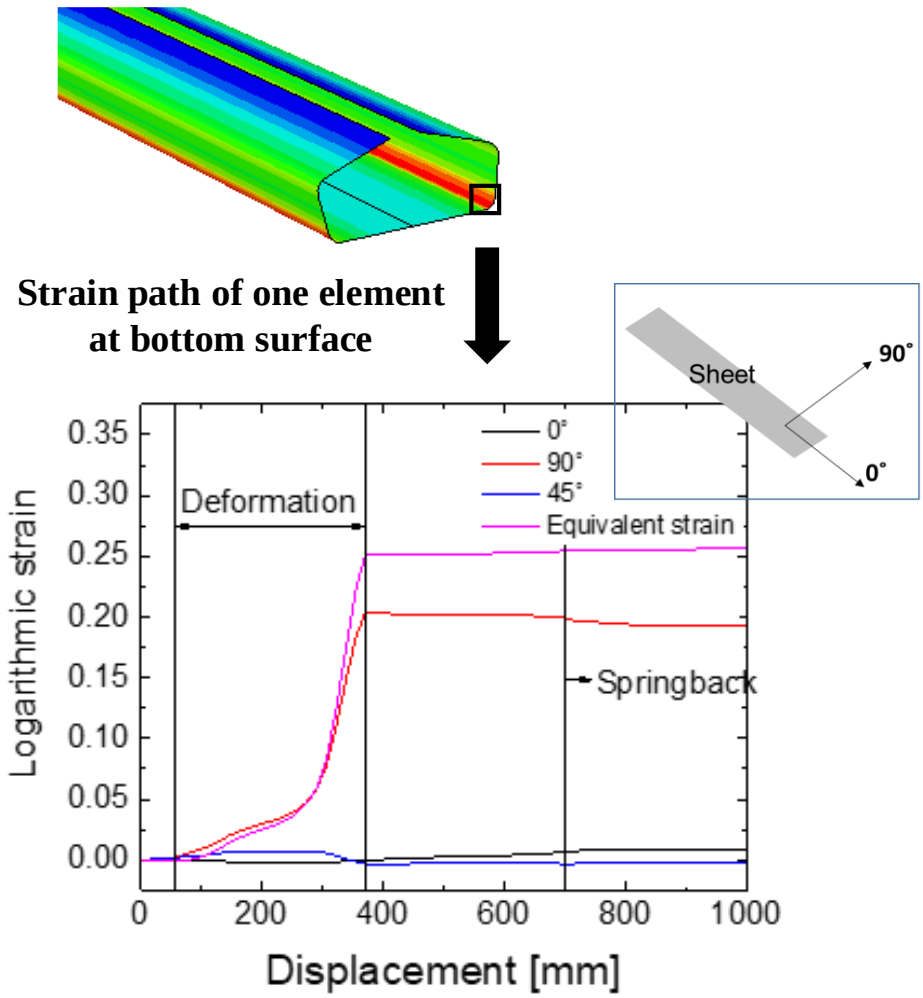

Fig. 4-19. Strain paths along different three directions in an element located tool coner region

In the following, the detailed analyses on the frictional behaviour during the press-forming are provided. In Fig. 4-20, the variation of the friction coefficient under different contact conditions are shown through the FE modeling. In this analysis, the friction model 2, which depends on both contact pressure and bulk strain, was employed. The figure also presents the contact pressure on top surface of the workpiece during forming. The contact

area is divided into three regions: (1) the area contact with the tool which exhibits relatively low contact pressure, (2) the area with maximum contact pressure, and (3) the area with maximum equivalent plastic strain (Figs. 4-20 and 4-21). The contact pressure on the top surface of the workpiece increases away from the location of the maximum equivalent plastic strain (base line) and decreases again as it leaves the tool corner. The equivalent plastic strain decreases as the distance from the base line increases.

In the area (1), which is relatively far from the tool corner, higher friction coefficient ($\mu \approx 0.2186$) was predicted, which attributes to the lower contact pressure and equivalent plastic strain than other regions. This result is directly related to the friction coefficient calculated from the friction model described in Section 4.1.3. The equivalent plastic strain in the region (2) was around 0.1, but the lowest friction coefficient ($\mu \approx 0.1633$) was applied because of the maximum contact pressure. The contact pressure in the area (3) was around 21 MPa, which is relatively low. But, the friction coefficient was lowered according to the equivalent plastic strain, which led to the friction coefficient almost similar to the value in the area (2) ($\mu \approx 0.1645$).

For the validation of the developed friction model, the reaction force was calculated from the FE simulation for different friction coefficient models. In Fig. 4-22, the reaction forces from FE simualtions are compared to the measured value. Note that the experimentally obtained reaction force was

only available at the steady state of forming, thus it is indicated as a constant value. For comparison purpose, simulations with three different constant friction models are also presented. The resuls shows that the simulated reaction force with variable friction model, developed in this study, agreed very well with experimental value. On the other hand, the constant friction model predicted either under- or over-estimated reaction force depending on its value. For example, the friction coefficient of 0.1, which is typical value in the benchmark simulation of sheet metal forming, quite under-estimated the reaction force.

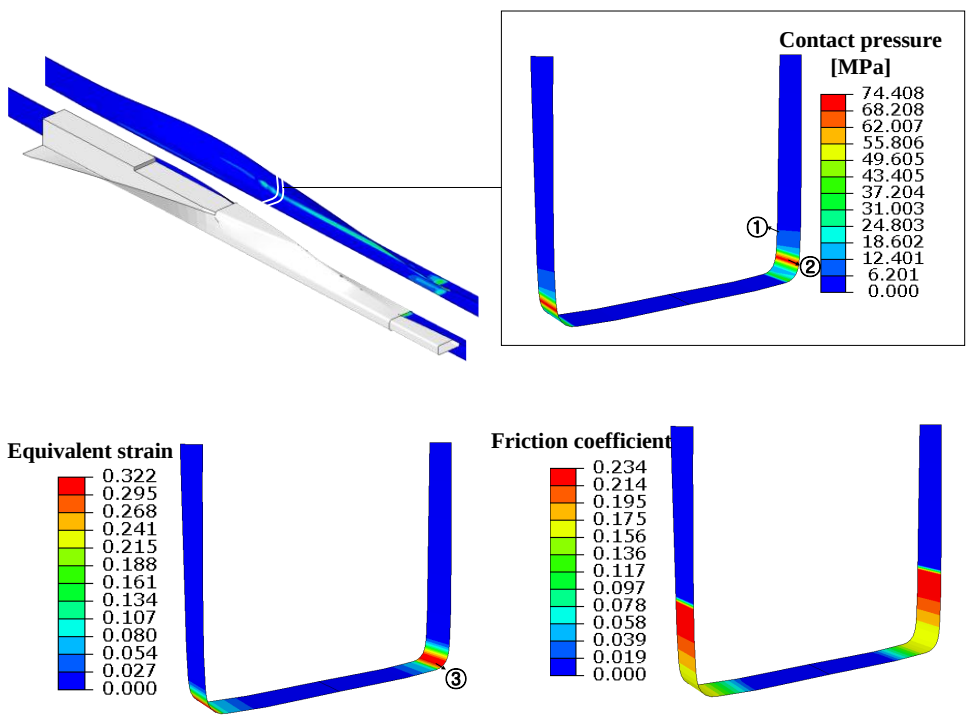

Fig. 4-20. Distribution of contact pressure, equivalent plastic strain and friction coefficient on the workpiece during the press-forming process. Three different contact regions are indicated in the figure

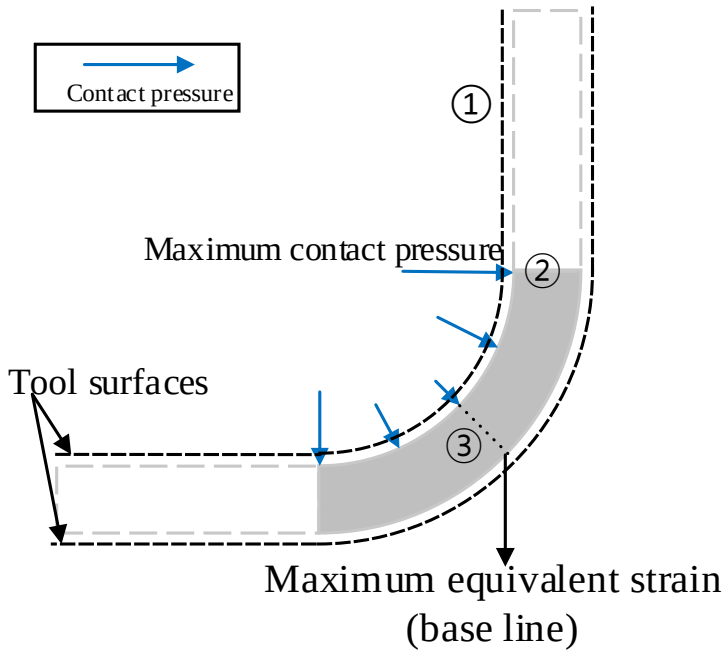

Fig. 4-21. Schematic view showing the three different contact areas in the curved part of workpiece

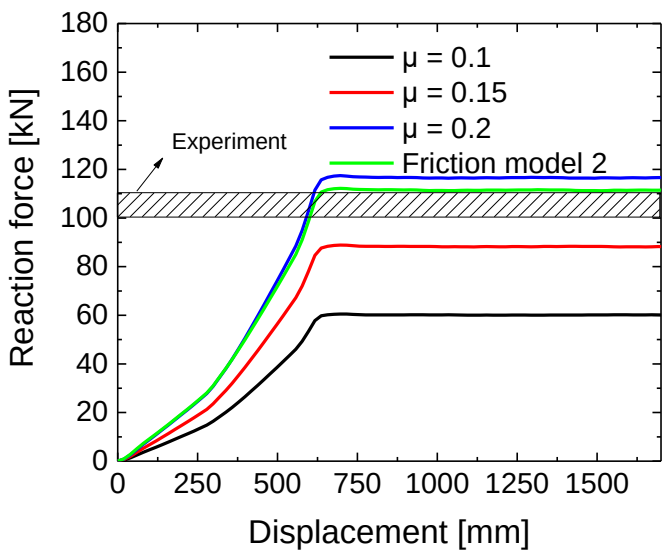

Fig. 4-22. Comparison of experimental and numerically predicted reaction force-displacement during the press-forming process

4.3. Application to sheet metal forming processes under lubrication conditions

FE model application of mixed-boundary lubrication friction model

Based on the prototype press-forming process introduced in the previous section, an industrial press forming process was developed to actually manufacture the sheet parts. As a triout, a side sill (shown in Fig. 4-23) for a vehicle body component was produced. The real equipment for the press forming is shown in Fig. 4-24 and the tools and sheet formed during the press-forming are shown in Fig. 4-25. Due to the complex deformation of the sheet material and contact state during forming, an appropriate lubrication was necessary to avoid forming defect. The forming oil with a kinematic viscosity of 162sCt and a specific gravity of 1.106 was applied to the press-forming tools. Like the previous case, the sheet material CP1470 with 1.2 mm thickness was used and the forming speed was 180 mm/s.

As in the section 4.2.2, the sheet blank and tool were modeled with the 4-node shell element with reduced integration (S4R) and the rigid body surface, respectively (Fig 4-26 (a)). Unlike the previous example, the press-forming process was implemented as a full finite element model due to the asymmetric geometry of side-sill component (Fig 4-26 (b)).

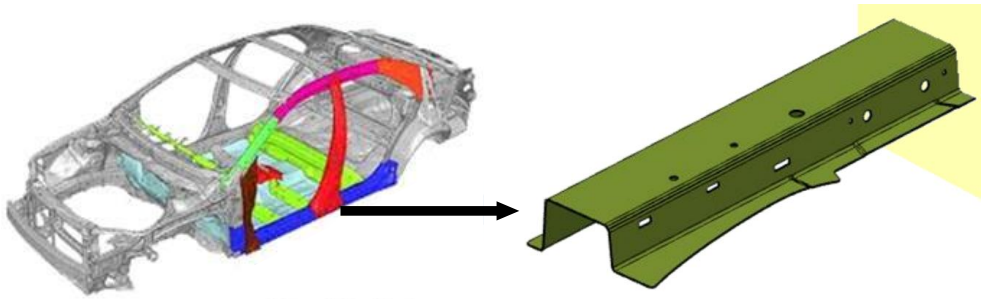

Fig. 4-23. The side-sill component in the frame structures of the vehicle

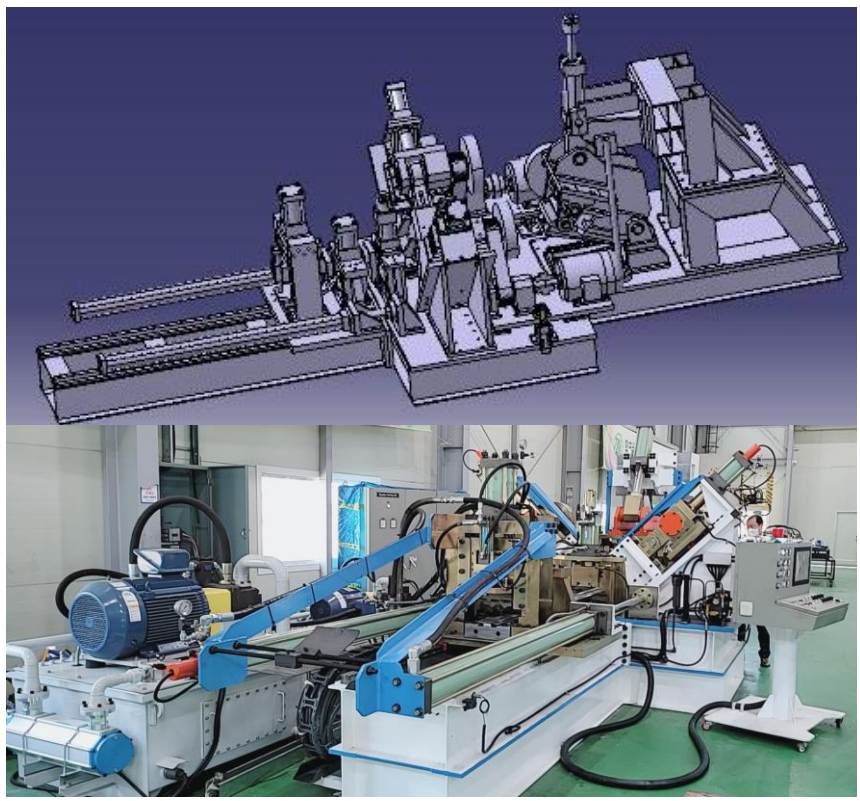

Fig. 4-24. Schematic and actual equipment of the newly developed press-forming process

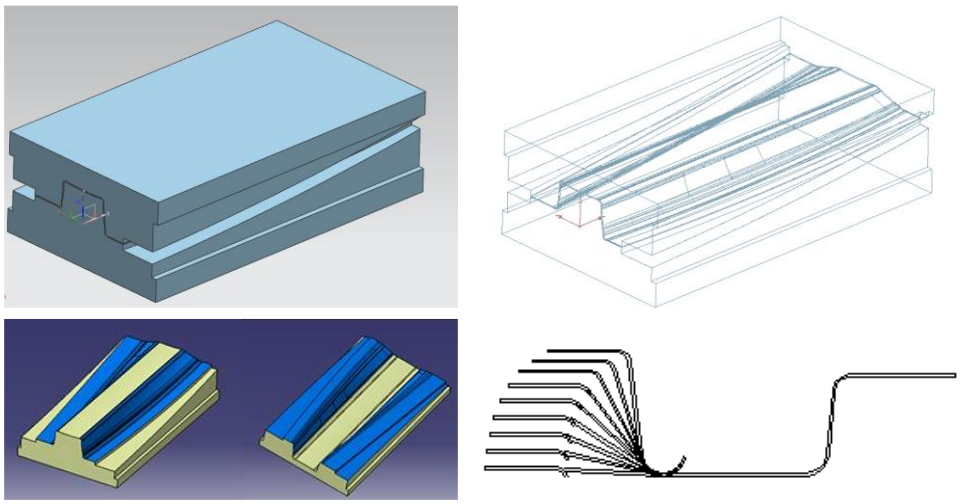

Fig. 4-25. The shape of the tools for the press-forming process and the deformation profiles of the sheet workpiece during forming

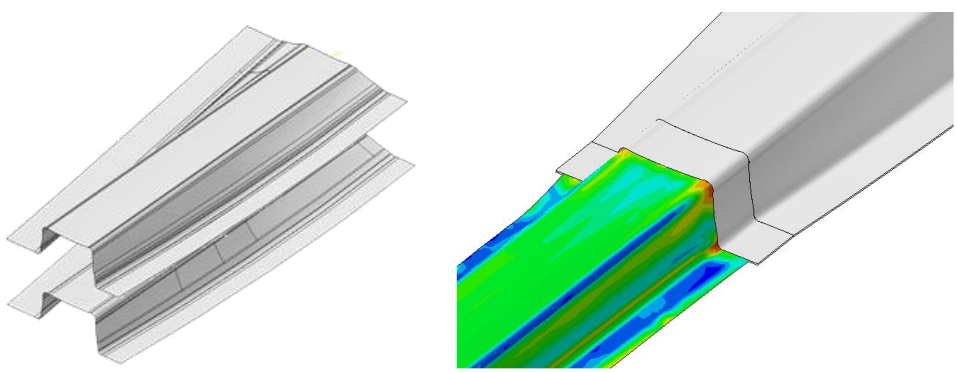

(a) (b)

Fig. 4-26. (a) The configurationshape of the toolss modeled with a rigid body element and (b) the forming of the sheet workpiece using in the FE simulation of model of the newly developed press-forming process

In the FE simulation, the mixed-boundary lubrication friction model (proposed by Hol [106]) described in Section 3.1 was applied by updating the friction coefficient at each time increment. This is because the contact condition changes with time increment during the general forming process.

In the press-forming process, contact conditions depend on the position of the tool, but not on forming time. That is, the friction coefficient between the tool and workpiece is spatially constant. Fig. 4-27 indicates that there is no obvious difference in contact conditions such as contact pressure and equivalent plastic strain at different forming times. Therefore, in this study the friction coefficients were calculated in advance as a function of position (or contact locations) outside the FE model and the friction coefficient was not updated at every time increment (see, Fig. 4-28).

The contact algorithm in the FE model for calculating the contact pressure was not directly built, but the contact pressure was calculated from FE software ABAQUS/Standard. The friction coefficient and nodal position calculated for each node were required as input data to the FE model of the press-forming process (Fig. 4-29). Since the nodes of workpiece in contact with tool are constantly changing, the friction coefficient should be applied appropriately. In this study, the input data closest to the workpiece node in contact with the tool was determined as shown in Fig. 4-29. This procedure was implemented in the user subroutine, UFILED in ABAQUS. In addition, the UFRIC subroutine was used to implement the mixed-boundary lubrication friction model.

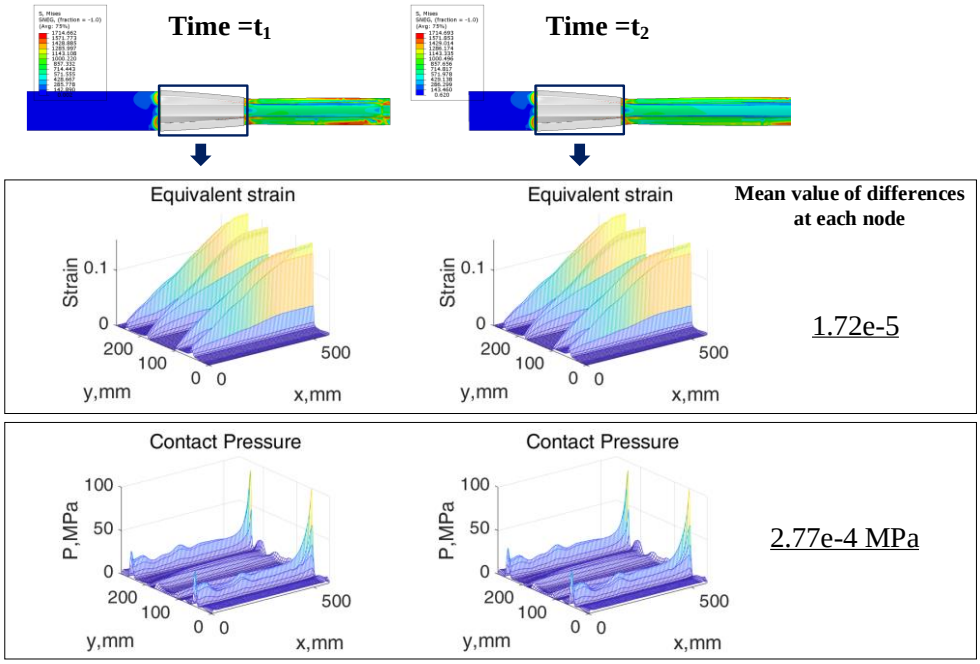

Fig. 4-27. Contact pressure and equivalent plastic strain of workpiece elements in contact with tool at two different time steps during press-forming process

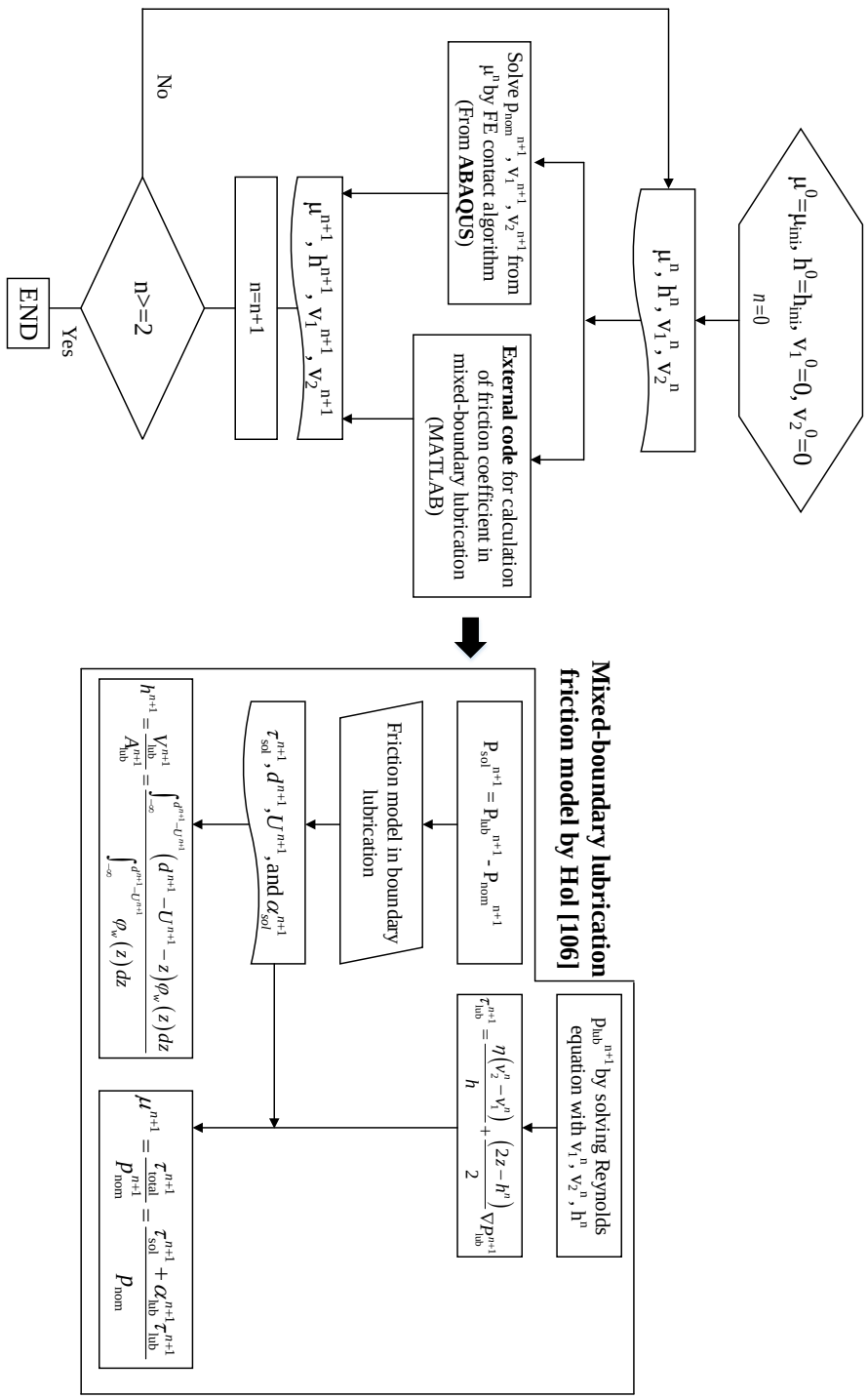

Fig. 4-28. Flow chart for the application of mixed-boundary lubrication friction model to the press forming process

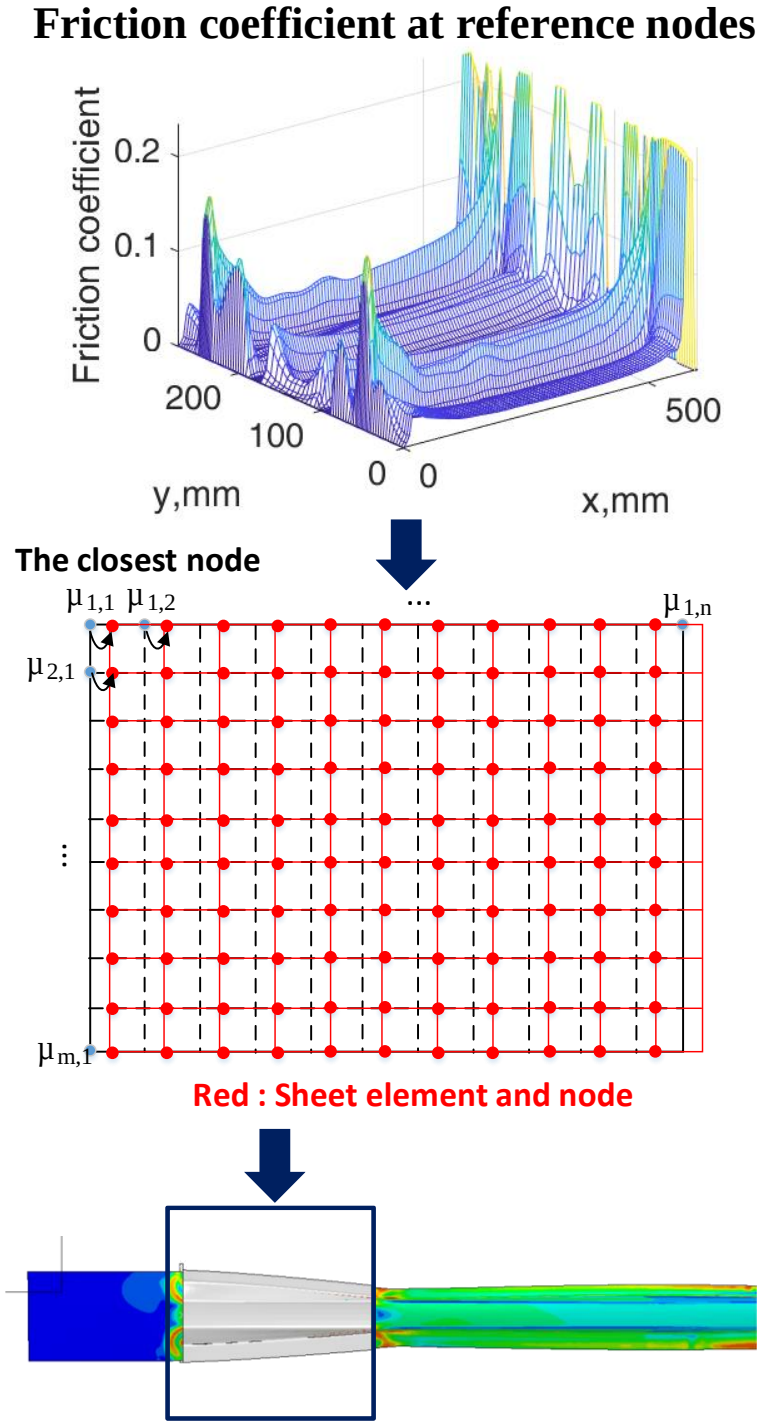

Fig. 4-29. Correlating the friction coefficient to the nearest nodal points for applying the pre-calculated friction coefficients to the FE model

In the proposed press forming process with lubrication, the hydrodynamic pressure is lower at the inlet and outlet of the forming tool because of the atmospheric pressure ($p_{lub} = 1atm \approx 0.1MPa$) and high nominal contact pressure. Therefore, the lubrication condition can be considered to be the boundary lubrication. The friction coefficient at the outlet shows a relatively high value ($\mu \approx 0.18$) from the calculation applying the boundary lubrication friction model (Fig. 4-30). In the blue colored rectangle of Fig. 4-30, higher lubrication pressure was calculated as the nominal contact pressure increased. Also, the film thickness decreased along the direction of forming process (Fig. 4-30 (b)). Therefore, it can be seen that the mixed-boundary lubrication friction model can represent the lubrication behavior well because of the low friction coefficient resulted from the significant lubrication effect ($\mu \approx 0.04$). Fig. 4-31 shows that the frictions of the bottom and top surfaces are properly applied to the friction coefficients of the FE model. As the boundary condition of the hydrodynamic pressure at the inlet and outlet, the surrounding hydrodynamic pressure is low and the friction coefficient is high. It is noted that the primary contact occurs only in the curved area where deformation of workpiece is concentrated.

In Fig. 4-32, the predicted springback profiles are compared with experiments and the enlarged views are shown at the coner regions in Fig. 4-32. The friction model in consideration with contact pressure, equivalent

plastic strain, sliding velocity, and lubrication effect was used for the simulation. For comparison the simuations with constant friction coefficients were also conducted and compared with the developed friction model. Table 4.4 lists the angle of each curvature predicted with different friction models. The result of the simulation with the variable friction coefficient calculated by the mixed boundary lubrication friction model gave more accurate springback profile than those with constant friction coefficients. See Figs 4-33 (c) and (d). In the constant friction model, the frictional force changes proportionally to the contact pressure, but the frictional force changes according to the contact conditions such as contact pressure, plastic strain, sliding velocity, and lubrication effect in the mixed boundary lubrication friction model. Therefore, the sophisticated friction behavior can be only accurately described by the variable friction model developed in this study.

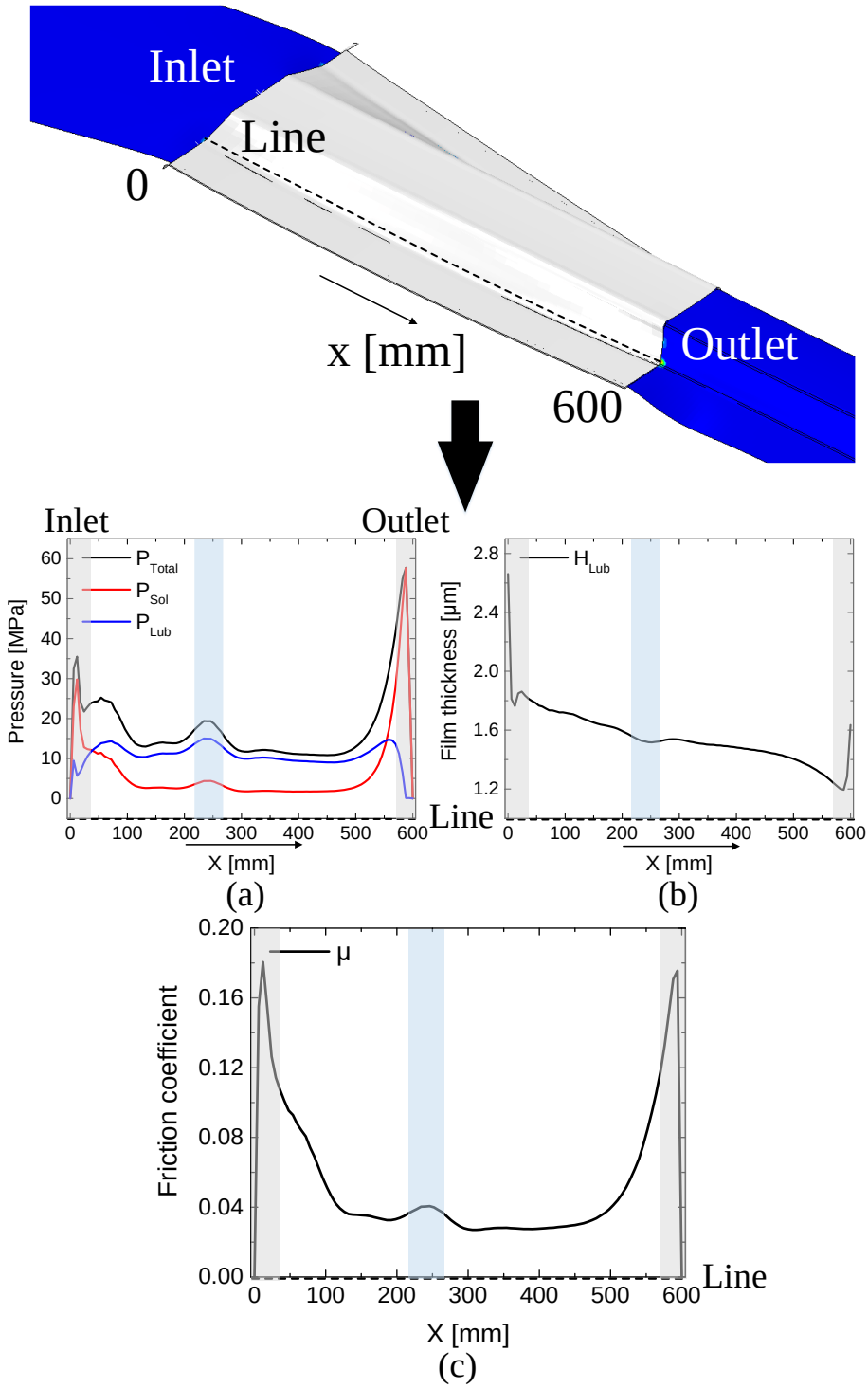

Fig. 4-30. Contact conditions calculated based on the line shown in the figure on the upper surface of the workpiece: (a) Total(nominal) contact

pressure, solid contact pressure, hydrodynamic pressure (b) film thickness, (c) friction coefficient

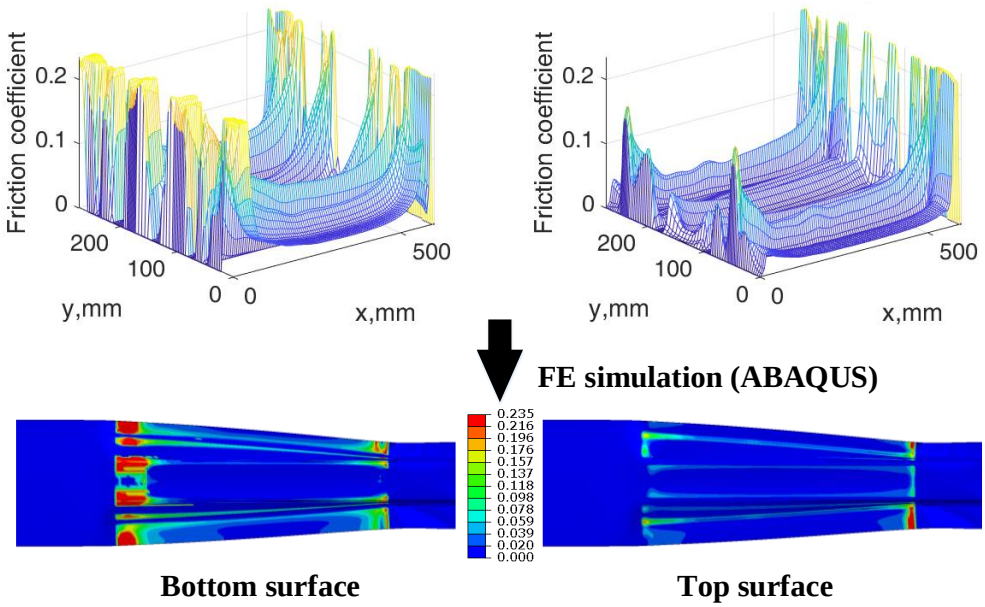

Fig. 4-31. The distribution of friction coefficient calculated from the mixed lubrication friction model on the top and bottom surfaces of the workpiece and its implementation to the FE model of press forming process

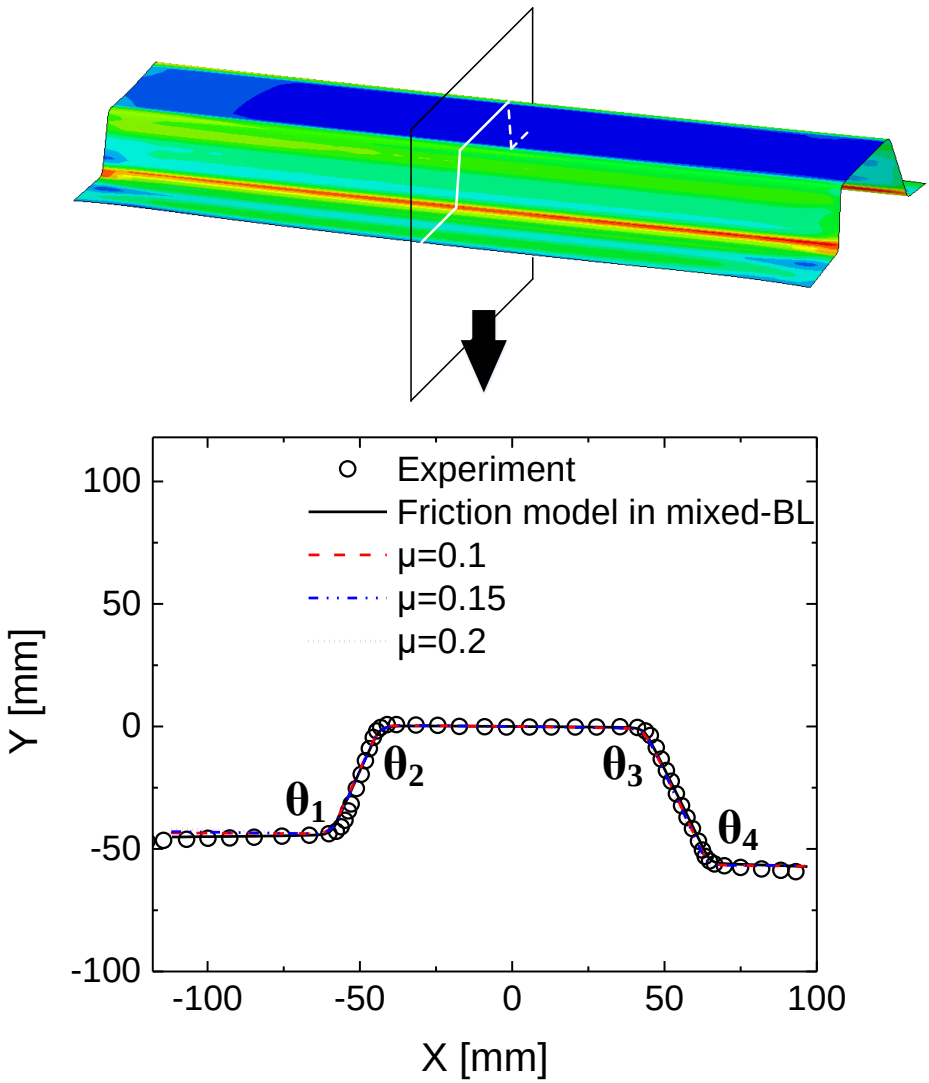

Fig. 4-32. Profiles after springback obtained experimentally and numerically in the developed press-forming process

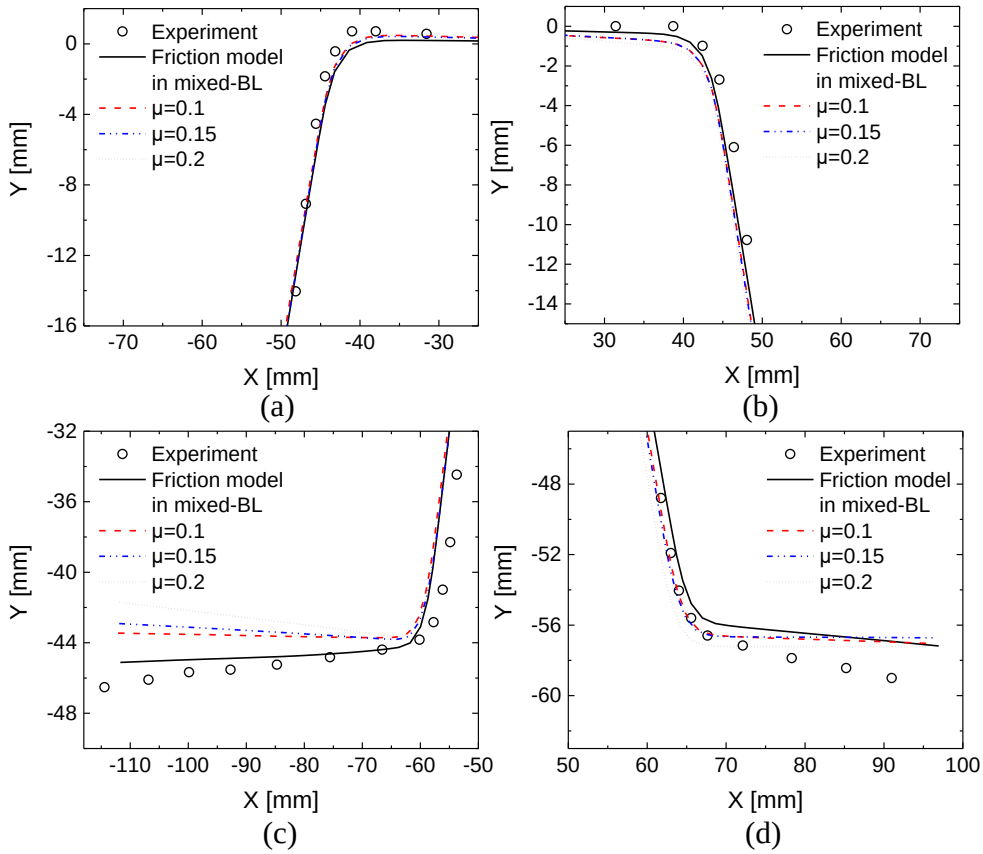

Fig. 4-33. Enlarged views around tool corner shown in Fig. 4-32

Table 4.4. Springback angles at four tool coners

	θ_1	θ_2	θ_3	θ_4
Experiment	113.50	106.76	111.05	116.91
Friction model	112.87	110.11	112.80	114.66
μ=0.1	110.47	110.02	112.67	112.40
μ=0.15	109.33	109.74	112.45	111.42
μ=0.2	107.88	109.32	112.13	110.60

5. Conclusions

Accurate prediction of formability and springback in sheet metal forming simulation requires reliable friction modeling, which represents the contact behavior between sheet metal and rigid tools. Therefore, the main purpose of this thesis is to develop a numerically efficient and robust computational model for considering the complex frictional behavior in metal forming process. To achieve this goal, a multi-scale friction model is proposed by formulating the friction in both the boundary lubrication and the mixed lubrication domains.

The boundary lubrication friction model is formulated based on the 3-dimensional tool and workpiece surfaces, the boundary layer shear strength, and other related model parameters. Changes in surface topography and evolution of friction are handled by the boundary lubrication friction model. The summary of the modeling for the boundary lubrication friction model is as follows.

- Larger real contact area is predicted by increasing the nominal contact pressure or increasing the bulk strain.
- The larger real contact area reduces the effective angle of attack. Also, for the reduced number of active contact patches, the friction coefficient is decreased.

- The proposed friction model can explain the orientation dependence of frictional behavior by accounting for the anisotropic surface texture.
- A numerically efficient finite element model is suggested by coupling the friction matrices which store the predefined nominal contact pressure and strain during the finite element simulation.

The boundary lubrication friction model is further extended to account for the mixed-boundary lubrication friction. The lubricating film thickness is determined from the volume of non-contact surface pockets obtained from the boundary lubrication friction model. The accuracy of the developed finite element model with the new friction model is verified by comparing the fluid (lubricant) behavior with the commercial program COMSOL® and by calculating the hydrodynamic pressure and film thickness in the elastohydrodynamic lubrication. The following conclusions are drawn regarding the boundary lubrication friction model.

- The hydrodynamic part of the mixed lubrication friction model depends only on the physical parameters such as the viscosity of lubricant applied to the surface and the roughness texture of workpiece surface.
- The load-sharing capacity of lubricant, which is equivalent to the reduced friction coefficient, increases by increasing the contact length, sliding speed and the nominal contact pressure.

- The surface roughness can significantly affect the load-bearing capacity of the lubricant, and increased surface roughness reduces the surface separation.
- The proposed mixed lubrication friction model can predict the reliable friction coefficient distribution.

Finally, the newly developed friction models for the boundary lubrication and mixed boundary lubrication are verified by applying them to the simulation of sheet metal forming process. First, the U-draw-bending process as a benchmark of the sheet metal forming is employed. Secondly, a newly developed press-forming process, both with a prototype or a real side-sill forming, is used for the validation.

- The decreased friction coefficient as a function of the contact pressure can be well predicted by the boundary lubrication friction model.
- In the finite element simulations with the boundary lubrication friction model for U-draw bending and the press-forming process, the reaction force and springback prifiles agree excellently well to the measured ones.

Under the steady-state condition of the press-forming process, the friction coefficient controlled by the mixed-boundary lubrication is pre-calculated outside the finite element simulation. This significantly reduces the

computational cost rather than the direct coupling between the friction model and finite element simulation. Good agreement of the side-sill profile with the experiment is obtained by using the developed friction model.

Appendix

Appendix A. Reference of journal pubilcations related to this thesis

Lee, K., Moon, C., and Lee, M. G. (2021). A Review on Friction and Lubrication in Automotive Metal Forming: Experiment and Modeling. International Journal of Automotive Technology, 22(6), 1743-1761.

Appendix B. Constitutive model parameters (TRIP780)

Table A. 1. Constitutive model parameters

Yld2000-2d	m	α_1	α_2	α_3	α_4	α_5	α_6	α_7	α_8
	6	1.005	0.887	0.815	0.961	0.984	0.847	0.964	1.085
HAH	q	k	k_1	k_2	k_3	k_4	k_5		
	2	30	16	90	0.5	0.8			
Chord	E_0 [GPa]	E_s [GPa]	ξ						
	198.5	159	40.5						

Reference

[1] Meinders, T., Burchitz, I. A., Bonté, M. H., and Lingbeek, R. A. (2008). Numerical product design: springback prediction, compensation and optimization. Int. J. Machine Tools and Manufacture, 48, 5, 499-514.

[2] Wiebenga, J. H., van den Boogaard, A. H. and Klaseboer, G. (2012). Sequential robust optimization of a V-bending process using numerical simulations. Structural and multidisciplinary optimization 46, 1, 137-153.

[3] Barlat, F., Brem, J. C., Yoon, J. W., Chung, K., Dick, R. E., Lege, D. J., Pourboghrat, F., Choi, S.H. and Chu, E. (2003). Plane stress yield function for aluminum alloy sheets—part 1: theory. Int. J. Plasticity 19, 9, 1297-1319.

[4] Barlat, F., Gracio, J. J., Lee, M. G., Rauch, E. F., and Vincze, G. (2011). An alternative to kinematic hardening in classical plasticity. Int. J. Plasticity 27, 9, 1309-1327.

[5] Lee, M. G., Kim, C., Pavlina, E. J. and Barlat, F. (2011). Advances in sheet forming—materials modeling, numerical simulation, and press technologies. J. Manufacturing Science and Engineering 133, 6, 061001.

[6] Resende, T. C., Bouvier, S., Abed-Meraim, F., Balan, T., and Sablin, S. S. (2013). Dislocation-based model for the prediction of the behavior of bcc materials–grain size and strain path effects. Int. J. Plasticity 47, 29–48.

[7] Hora, P., Heingärtner, J., Manopulo, N. and Tong, L. (2011). Zero failure production methods based on a process integrated virtual control. AIP Conf. Proc. 1383, 1, 35–47.

[8] Azushima, A. and Kudo, H. (1995). Direct observation of contact behaviour to interpret the pressure dependence of the coefficient of friction in sheet metal forming. CIRP Annals 44, 1, 209–212.

[9] Czichos, H. (2009). Tribology: a systems approach to the science and technology of friction, lubrication, and wear. 1st edn. Elsevier Scientific Publishing company. Amsterdam, Netherlands.

[10] Felder, E. and Samper, V. (1994). Experimental study and theoretical interpretation of the frictional mechanisms in steel sheet forming. Wear 178, 1-2, 85–94.

[11] Greenwood, J. A. and Williamson, J. P. (1966). Contact of nominally flat surfaces. Proc. Royal Society of London. Series A. Mathematical and Physical Sciences 295, 1442, 300–319.

[12] Han, S. S. and Kim, D. J. (2011). Contact pressure effect on frictional characteristics of steel sheet for autobody. AIP Conf. Proc. 1383, 1, 780–783.

[13] Bang, J., Park, N., Song, J., Kim, H. G., Bae, G. and Lee, M. G. (2021). Tool wear prediction in the forming of automotive DP980 steel sheet using statistical sensitivity analysis and accelerated U-bending based wear test. Metals 11, 2, 306.

[14] Lee, Y., Jung, S., Baek, H., Lee, J., Choi, M. S. and Lee, M. G. (2019). Effect of anisotropic plasticity on the prediction of formability of E-form magnesium alloy sheet. Int. J. Automotive Technology 20, 6, 1183–1193.

[15] Myung, D., Noh, W., Kim, J. H., Kong, J., Hong, S. T. and Lee, M. G. (2021). Probing the mechanism of friction stir welding with ALE based finite element simulations and its application to strength prediction of welded aluminum. Metals and Materials Int. 27, 4, 650–666.

[16] Bok, H. H., Lee, M. G., Kim, H. D. and Moon, M. B. (2010). Thermo-mechanical finite element analysis incorporating the temperature dependent stress-strain response of low alloy steel for practical application to the hot stamped part. Metals and Materials Int. 16, 2, 185–195.

[17] Bok, H. H., Choi, J., Barlat, F., Suh, D. W., and Lee, M. G. (2014). Thermo-mechanical-metallurgical modeling for hot-press forming in consideration of the prior austenite deformation effect. Int. J. Plasticity, 58, 154–183.

[18] Filzek, J. and Groche, P. (2001). Assessment of the tribological function of lubricants for sheet metal forming. Bench Testing of Industrial Fluid Lubrication and Wear Properties Used in Machinery Applications. ASTM International.

[19] Grüebler, R. and Hora, P. (2009). Temperature dependent friction modeling for sheet metal forming. Int. J. Material Forming 2, 1, 251–254.

[20] S. Kim, J. Lee, F. Barlat, M.-G. Lee, Formability prediction of advanced high strength steels using constitutive models characterized by uniaxial and biaxial experiments, Journal of Materials Processing Technology. 213 (2013).

[21] Schipper, D. J. and De Gee, A. W. J. (1995). Lubrication modes and the IRG transition diagram. Lubrication Science 8, 1, 27–35.

[22] Challen, J. M. and Oxley, P. L. B. (1984). A slip line field analysis of the transition from local asperity contact to full contact in metallic sliding friction. Wear 100, 1-3, 171193.

[23] Darendeliler, H., Akkök, M. and Yücesoy, C. A. (2002). Effect of variable friction coefficient on sheet metal drawing. Tribology Int. 35, 2, 97–104.

[24] Hol, J., Meinders, V. T., de Rooij, M. B. and Boogaard, A. H. (2015). Multi-scale friction modeling for sheet metal forming: The boundary lubrication regime. Tribology Int., 81, 112–128.

[25] Kim, C., Lee, J. U., Barlat, F. and Lee, M. G. (2014). Frictional behaviors of a mild steel and a TRIP780 steel under a wide range of contact stress and sliding speed. J. Tribology 136, 2, 021606.

[26] Stribeck, R. (1902). Die wesentlichen eigenschaften der gleit- und rollenlager. Zeitschrift des Vereins Deutscher Ingenieure, 46, 1341–1348

[27] Hersey, M. D. (1914). The laws of lubrication of horizontal journal bearings. J. Washington Academy of Sciences 4, 19, 542–552.

[28] Hersey, M. D. (1914). The laws of lubrication of horizontal journal bearings. J. Washington Academy of Sciences 4, 19, 542–552.

[29] Hardy, W. B. and Doubleday, I. (1922). Boundary lubrication.—The paraffin series. Proceedings of the Royal Society of London. Series A, Containing Papers of a Mathematical and Physical Character, 100, 707, 550-574.

[30] Holm, R. (1938). The friction force over the real area of contact. Wissenschaftliche Veröffentlichungen aus den Siemens-Werken 17, 4, 38–42.

[31] Ernst, H. E. M. E. and Merchant, M. E. (1940). Surface friction of clean metals: a basic factor in the metal cutting process. Proc. MIT Conf. Friction and Surface Finish. Cambridge, MA, USA.

[32] Bowden, F. P. and Tabor, D. (1939). The area of contact between stationary and moving surfaces. Proc. Royal Society of London. Series A. Mathematical and Physical Sciences 169, 938, 391–413.

[33] Bowden, F. P. and Tabor, D. (1942). Mechanism of metallic friction. Nature 150, 3798, 197–199.

[34] Bowden, F. P. and Tabor, D. (1943). The lubrication by thin metallic films and the action of bearing metals. J. Applied Physics 14, 3, 141–151.

[35] Bowden, F. P., Moore, A. J. W. and Tabor, D. (1943). The ploughing and adhesion of sliding metals. J. Applied Physics 14, 2, 80–91.

[36] Green, A. P. (1954). The plastic yielding of metal junctions due to combined shear and pressure. J. Mechanics and Physics of Solids 2, 3, 197–211.

[37] Green, A. P. (1955). Friction between unlubricated metals: a theoretical analysis of the junction model. Proc. Royal Society of London. Series A. Mathematical and Physical Sciences 228, 1173, 191–204.

[38] Tabor, D. (1959). Junction growth in metallic friction: the role of combined stresses and surface contamination. Proc. Royal Society of London. Series A. Mathematical and Physical Sciences 251, 1266, 378–393.

[39] Bowden, F. P. and Young, J. E. (1951). Friction of clean metals and the influence of adsorbed films. Proc. Royal Society of London. Series A. Mathematical and Physical Sciences 208, 1094, 311–325.

[40] Kayaba, T. and Kato, K. (1978). Experimental analysis of junction growth with a junction model. Wear 51, 1, 105116.

[41] McFarlane, J. S. and Tabor, D. (1950). Relation between friction and adhesion. Proc. Royal Society of London. Series A. Mathematical and Physical Sciences 202, 1069, 244–253.

[42] Parker, R. C. and Hatch, D. (1950). The static coefficient of friction and the area of contact. Proc. Physical Society. Section B 63, 3, 185.

[43] Lo, S. W. and Tsai, S. D. (2002). Real-time observation of the evolution of contact area under boundary lubrication in sliding contact. J. Tribology 124, 2, 229–238.

[44] Shaw, M. C., Ber, A. and Mamin, P. A. (1960). Friction characteristics of sliding surfaces undergoing subsurface plastic flow. J. Basic Engineering 82, 2, 342–345.

[45] Greenwood, J. A. and Tripp, J. H. (1967). The elastic contact of rough spheres. J. Applied Mechanics 34, 1, 153–159.

[46] Halling, J., Arnell, R. D. and Nuri, K. A. (1988). The elastic – plastic contact of rough surfaces and its relevance in the study of wear. Proc. Institution of Mechanical Engineers, Part C: J. Mechanical Engineering Science 202, 4, 269274.

[47] Halling, J. and Nuri, K. A. (1991). Elastic/plastic contact of surfaces considering ellipsoidal asperities of workhardening multi-phase materials. Tribology Int. 24, 5, 311–319.

[48] Hertz, H. (1881). On the contact of elastic solids. J. Reine und Angewandte Mathematik, 92, 156–171.

[49] Timoshenko, S. and Goodier, J. N. (1951). Theory of elasticity. 2nd edn. McGraw-Hill. New York, NY, USA.

[50] Greenwood, J. A. and Tripp, J. H. (1971). The contact of two nationally flat surfaces. Proc. Institution of Mechanical Engineers 28, 1, 91–96.

[51] Hisakado, T. (1974). Effect of surface roughness on contact between solid surfaces. Wear 28, 2, 217–234.

[52] Bush, A. W., Gibson, R. D. and Thomas, T. R. (1975). The elastic contact of a rough surface. Wear 35, 1, 87–111.

[53] McCool, J. I. (1986). Predicting microfracture in ceramics via a microcontact model. J. Tribology 108, 3, 380–385.

[54] Chang, W. R., Etsion, I. and Bogy, D. B. (1987). An elasticplastic model for the contact of rough surfaces. J. Tribology 109, 2, 257–263.

[55] Hisakado, T. (1970). On the mechanism of contact between solid surfaces: 4th report, surface roughness effects on dry friction. Bulletin of JSME 13, 55, 129–139.

[56] Nayak, P. R. (1971). Random process model of rough surfaces. J. Lubrication Technology 93, 3 398–407.

[57] Nayak, P. R. (1973). Some aspects of surface roughness measurement. Wear 26, 2, 165–174.

[58] Nayak, P. R. (1973b). Random process model of rough surfaces in plastic contact. Wear 26, 3, 305–333.

[59] Pullen, J. and Williamson, J. B. P. (1972). On the plastic contact of rough surfaces. Proc. Royal Society of London. A. Mathematical and Physical Sciences 327, 1569, 159173.

[60] Challen, J. M. and Oxley, P. L. B. (1979). An explanation of the different regimes of friction and wear using asperity deformation models. Wear 53, 2, 229–243.

[61] Black, A. J., Kopalinsky, E. M. and Oxley, P. L. B. (1990). Sliding metallic friction with boundary lubrication: an investigation of a simplified friction theory and of the nature of boundary lubrication. Wear 137, 2, 161–174.

[62] Greenwood, J. A. and Rowe, G. W. (1965). Deformation of surface asperities during bulk plastic flow. J. Applied Physics 36, 2, 667–668.

[63] Fogg, B. (1967). Preliminary study of the influence of stress and deformation in the substrate on junction growth and friction. Proc. Institution of Mechanical Engineers, Conf. Proc. 182, 11, 152–161.

[64] Wilson, W. R. D. and Sheu, S. (1988). Real area of contact and boundary friction in metal forming. Int. J. Mechanical Sciences 30, 7, 475–489.

[65] Sutcliffe, M. P. F. (1988). Surface asperity deformation in metal forming processes. Int. J. Mechanical Sciences 30, 11, 847–868.

[66] Atala, H. F. and Rowe, G. W. (1975). Surface roughness changes during rolling. Wear 32, 2, 249–268.

[67] Makinouchi, A., Ike, H., Murakawa, M. and Koga, N. (1988). A finite element analysis of flattening of surface asperities by perfectly lubricated rigid dies in metal working processes. Wear 128, 2, 109–122.

[68] Ike, H. and Makinouchi, A. (1990). Effect of lateral tension and compression on plane strain flattening processes of surface asperities lying over a plastically deformable bulk. Wear 140, 1, 17–38.

[69] Korzekwa, D. A., Dawson, P. R. and Wilson, W. R. D. (1992). Surface asperity deformation during sheet forming. Int. J. Mechanical Sciences 34, 7, 521–539.

[70] Wilson, W. R. D. (1991). Friction models for metal forming in the boundary lubrication regime. J. Engineering Materials and Technology 113, 1, 60–68.

[71] Zhao, Y., Maietta, D. M. and Chang, L. (2000). An asperity microcontact model incorporating the transition from elastic deformation to fully plastic flow. J. Tribology 122, 1, 86–93.

[72] Johnson, K. L. (1985). Contact mechanics. 1st edn. Cambridge University Press, Cambridge, UK.

[73] Handzel-Powierza, Z., Klimczak, T. and Polijaniuk, A. (1992). On the experimental verification of the Greenwood-Williamson model for the contact of rough surfaces. Wear 154, 1, 115–124.

[74] Jeng, Y. R. and Wang, P. Y. (2003). An elliptical microcontact model considering elastic, elastoplastic, and plastic deformation. J. Tribology 125, 2, 232–240.

[75] Ciulli, E., Ferreira, L. A., Pugliese, G. and Tavares, S. M. O. (2008). Rough contacts between actual engineering surfaces: Part I. Simple models for roughness description. Wear 264, 11-12, 1105–1115.

[76] Pugliese, G., Tavares, S. M. O., Ciulli, E. and Ferreira, L. A. (2008). Rough contacts between actual engineering surfaces: Part II. Contact mechanics. Wear 264, 11-12, 1116–1128.

[77] Westeneng, J. D. (2001). Modelling of contact and friction in deep drawing processes. Ph.D. dissertation. University of Twente. Enshede, Netherlans.

[78] Ma, X., De Rooij, M. and Schipper, D. (2010). A load dependent friction model for fully plastic contact conditions. Wear 269, 11-12, 790–796.

[79] Hol, J., Alfaro, M. C., de Rooij, M. B. and Meinders, T. (2012). Advanced friction modeling for sheet metal forming. Wear, 286, 66–78.

[80] Hol, J., Meinders, V. T., de Rooij, M. B. and Boogaard, A. H. (2015). Multi-scale friction modeling for sheet metal forming: The boundary lubrication regime. Tribology Int., 81, 112–128.

[81] Karupannasamy, D. K., de Rooij, M. B. and Schipper, D. J. (2013). Multi-scale friction modelling for rough contacts under sliding conditions. Wear 308, 1-2, 222–231.

[82] Masen, M. A., de Rooij, M. B. and Schipper, D. J. (2005). Micro-contact based modelling of abrasive wear. Wear 258, 1-4, 339–348.

[83] Karupannasamy, D. K., Hol, J., de Rooij, M. B., Meinders, T. and Schipper, D. J. (2014). A friction model for loading and reloading effects in deep drawing processes. Wear 318, 1-2, 27–39.

[84] Reynolds, O. (1886). IV. On the theory of lubrication and its application to Mr. Beauchamp tower's experiments, including an experimental determination of the viscosity of olive oil. Philosophical Trans. Royal Society of London, 177, 157–234.

[85] Patir, N. and Cheng, H. S. (1978). An average flow model for determining effects of three-dimensional roughness on partial hydrodynamic lubrication. J. Lubrication Technology 100, 1, 12–17.

[86] Patir, N. and Cheng, H. S. (1979). Application of average flow model to lubrication between rough sliding surfaces. J. Lubrication Technology, 101, 2, 220–229.

[87] Almqvist, A., Lukkassen, D., Meidell, A. and Wall, P. (2007). New concepts of homogenization applied in rough surface hydrodynamic lubrication. Int. J. Engineering Science 45, 1, 139–154.

[88] Bayada, G. and Faure, J. B. (1989). A double scale analysis approach of the Reynolds roughness comments and application to the journal bearing. J. Tribology 111, 2, 323–330.

[89] Elrod, H. G. (1973). Thin-film lubrication theory for Newtonian fluids with surfaces possessing striated roughness or grooving. J. Lubrication Technology 95, 4, 484–489.

[90] Hamrock, B. J., Schmid, B. J. and Jacobson, B. O. (2004). Fundamentals of fluid film lubrication. CRC Press. New York, NY, USA.

[91] Johnson, K. L., Greenwood, J. A. and Poon, S. Y. (1972). A simple theory of asperity contact in elastohydro-dynamic lubrication. Wear 19, 1, 91–108.

[92] Wilson, W. R. D. (1971). The temporary breakdown of hydrodynamic lubrication during the initiation of extrusion. Int. J. Mechanical Sciences 13, 1, 17–28.

[93] Wilson, W. R. D. (1978). Friction and lubrication in bulk metal-forming processes. J. Applied Metalworking, 1, 1, 7–19.

[94] Wilson, W. R. D. and Wang, J. J. (1984). Hydrodynamic lubrication in simple stretch forming processes. J. Tribology 106, 1, 70–77.

[95] Chen, K. K. and Sun, D. C. (1986). Hydrodynamic lubrication in hemispherical punch stretch forming. J. Applied Mechanics 53, 2, 440–449.

[96] Sun, D. C., Chen, K. K. and Nine, H. D. (1987). Hydrodynamic lubrication in hemispherical punch stretch forming—modified theory and experimental validation. Int. J. Mechanical Sciences 29, 10-11, 761–776.

[97] Wilson, W. R. D. and Hector Jr, L. G. (1991). Hydrodynamic lubrication in axisymmetric stretch forming—part 1: theoretical analysis. J. Tribology 113, 4, 659–666.

[98] Hsu, T. C. and Wilson, W. R. (1994). Refined models for hydrodynamic lubrication in axisymmetric stretch forming. J. Tribology 116, 1, 101–109.

[99] Sheu, S. and Wilson, W. R. (1994). Mixed lubrication of strip rolling. Tribology Trans. 37, 3, 483–493.

[100] Wilson, W. R. D., Hsu, T. C. and Huang, X. B. (1995). A realistic friction model for computer simulation of sheet metal forming processes. J. Engineering for Industry 117, 2, 202–209.

[101] Karupannasamy, D. K., Hol, J., de Rooij, M. B., Meinders, T. and Schipper, D. J. (2012). Modelling mixed lubrication for deep drawing processes. Wear, 294, 296–304.

[102] Booker, J. F. and Huebner, K. H. (1972). Application of finite element methods to lubrication: an engineering approach. J. Lubrication Technology 94, 4, 313–323.

[103] Hu, Y. K. and Liu, W. K. (1993). An ALE hydrodynamic lubrication finite element method with application to strip rolling. Int. J. Numerical Methods in Engineering 36, 5, 855–880.

[104] Yang, T. S. and Lo, S. W. (2004). A finite element analysis of full film lubricated metal forming process. Tribology Int. 37, 8, 591–598.

[105] Boman, R. and Ponthot, J. P. (2004). Finite element simulation of lubricated contact in rolling using the arbitrary Lagrangian–Eulerian formulation. Computer Methods in Applied Mechanics and Engineering 193, 3941, 4323–4353.

[106] Hol, J., Meinders, V. T., Geijselaers, H. J. and van den Boogaard, A. H. (2015). Multi-scale friction modeling for sheet metal forming: The mixed lubrication regime. Tribology Int., 85, 10–25.

[107] Sigvant, M., Pilthammar, J., Hol, J., Wiebenga, J. H., Chezan, T., Carleer, B. and van den Boogaard, A. H. (2016). Friction and lubrication modeling in sheet metal forming simulations of a Volvo XC90 inner door. IOP Conf. Series: Materials Science and Engineering, 159, 012021.

[108] Hokkirigawa, K. and Kato, K. (1988). An experimental and theoretical investigation of ploughing, cutting and wedge formation during abrasive wear. Tribology international, 21(1), 51-57.

[109] Hu, M. K. (1962). Visual pattern recognition by moment invariants. IRE transactions on information theory, 8(2), 179-187.

[110] Habchi, W. (2018). Finite element modeling of elastohydrodynamic lubrication problems. John Wiley & Sons.

[111] Lim, J. S. (1990). Two-dimensional signal and image processing. Englewood Cliffs.

[112] Lee, J. Y., Barlat, F. and Lee, M. G. (2015). Constitutive and friction modeling for accurate springback analysis of advanced high strength steel sheets. Int. J. Plasticity, 71, 113–135.

[113] Thibaud, S., Boudeau, N. and Gelin, J. C. (2004). Coupling effects of hardening and damage on necking and bursting conditions in sheet metal forming. International Journal of Damage Mechanics, 13(2), 107-122.

[114] Yoshida, F., Uemori, T. and Fujiwara, K. (2002). Elastic–plastic behavior of steel sheets under in-plane cyclic tension–compression at large strain. International journal of plasticity, 18(5-6), 633-659.

[115] Lee, J. W., Lee, M. G. and Barlat, F. (2012). Finite element modeling using homogeneous anisotropic hardening and application to spring-back prediction. International Journal of plasticity, 29, 13-41.

[116] Chaboche, J. L. (1986). Time-independent constitutive theories for cyclic plasticity. International Journal of plasticity, 2(2), 149-188.

[117] Chaboche, J. L. (1989). Constitutive equations for cyclic plasticity and cyclic viscoplasticity. International journal of plasticity, 5(3), 247-302.

Korean abstract

AHSS(고장력강판)의 판금 성형은 경량화에 의한 연비 향상과 고강도화에 의한 승객 안전으로 자동차 산업에서 큰 주목을 받고 있습니다. 그러나 AHSS를 이용한 자동차 부품 제조는 기존의 저강도 강재에 비해 스프링백 및 성형성이 좋지않기에 툴 설계 단계에서 시행착오가 더 많이 발생하게 됩니다.

자동차 부품에 AHSS를 적용할 때 이러한 문제를 극복하기 위해 유한 요소 시뮬레이션은 실제 시험 전에 판재 성형 부품의 스프링백 및 성형성을 예측하기 위한 수치해석적 도구로 일반적으로 사용되었습니다. 판재 성형 공정에서 유한 요소 시뮬레이션의 정확한 모델링은 신뢰할 수 있는 수치해석적 기술, 구성 방정식, 정확한 경계 조건 등이 필요합니다. 이 중 마찰은 시뮬레이션의 정확도를 결정하는 중요한 요소 중 하나이지만 대부분의 시뮬레이션에서 간과되어 왔습니다. 판재 성형에서 마찰 거동은 매우 복잡하고 표면 거칠기, 접촉 압력, 미끄럼 속도, 윤활 조건 등과 같은 다양한 매개변수에 따라 달라지는 것으로 알려져 있습니다. 그러나, 대부분의 유한 요소 해석에서 가장 간단한 쿨롱 마찰 법칙을 사용하는 것이 일반적입니다.

본 연구에서는 접촉면 사이의 힘 평형을 만족시키기 위해 새로운 모델 매개변수를 부과하여 마이크로 스케일 돌기 기반 마찰 모델을 추가로 수정했습니다. 또한 마찰의 쟁기질 효과를 결정하기 위해 툴 표면의 기하학적 형상 모델이 새로 제안되었습니다. 툴 형상은 표면 측정 장비의 분해능에 의존하는 정점이 아니라 측정된 파장에 의해 결정되는 툴표면 높이 조도의

서밋을 기반으로 모델링됩니다.

마찰모델은 경계윤활조건뿐만 아니라 충분한 윤활이 존재하는 혼합경계윤활조건에서도 필요하다. 유체역학적 마찰 모델은 윤활 영역과 금속 대 금속 접촉을 별도로 고려하는 하중 공유 개념을 사용합니다. 본 연구에서는 유체역학적 마찰 모델을 경계 윤활 마찰 모델과 결합하여 혼합 윤활 영역의 마찰을 설명합니다. 비접촉 표면 밸리의 부피로 계산된 윤활유 필름 두께는 커플링을 구현하는 데 사용됩니다. 필름 윤활 거동은 유체역학적 압력의 계산을 가능하게 하는 Reynolds 방정식의 유한 요소 방법을 사용해 구현됩니다.

경계 윤활 마찰 모델을 검증하기 위해 경계 윤활 조건에서 접촉 압력에 따라 계산된 마찰 계수와 측정된 마찰 계수를 비교합니다. 또한 경계 윤활 마찰 모델은 U-draw/bending 과정에 적용된 유한 요소 시뮬레이션을 통해 검증되었습니다. 마지막으로 경계 윤활 마찰 모델과 혼합 경계 윤활 마찰 모델을 새로 개발된 프레스 성형 공정의 유한 요소 시뮬레이션에 적용했는데, 이는 접촉 압력, 미끄럼 속도 및 윤활과 같은 다양한 변수의 영향을 나타냅니다. 검증 결과는 개발된 다중 스케일 마찰 모델과 그 구현이 마찰 거동이 자동차 부품 품질에 중요한 판재 성형 시뮬레이션에 효율적으로 사용될 수 있음을 보여줍니다.

감사의 글

2015년 9월 학부연구생으로 시작해서 벌써 6년이 넘는 시간동안 연구를 하면서 학교도 옮기고 결혼도 하는 동안 큰일 없이 박사를 취득할 수 있게 해주신 교수님께 먼저 감사드립니다. 제 결혼 주례 해주신 것도 많이 귀찮으시고 부담 되셨을텐데 신경 써주셔서 감사드리고 연구적으로도 제가 워낙 엄살이 심해 많이 불평했는데도 매번 방향을 계속 잡아주셔서 우여곡절은 있었지만 잘 마칠 수 있었습니다.

연구적인 관점이나 연구가 어떻게 활용되고 적용될지를 많이 지도해주신 최인석 교수님께도 감사드립니다. 매번 다른 방향으로 생각하게 해주셔서 우물 안 개구리가 되지 않게 사고를 넓히게 되었습니다. 그리고, 저는 기회가 없어서 크게 접점은 없었지만 박사 학위 심사에서 여러 코멘트를 주신 한흥남 교수님께도 감사드립니다.

매번 실험으로 귀찮게 해드렸지만 정말 감사하게도 잘해주신 이진우 박사님과 해외학외에서 잠깐 인사드렸지만 교수님과의 연으로 박사학위 심사에 참여해주신 송정한 박사님과 이진우 박사님과 더불어 매번 실험에 큰 도움을 주신 봉혁종 박사님께도 감사드립니다.

현대자동차 과제뿐 아니라 여러 다른 방면으로 도움 많이 주셔서 사회생활을 시작하게 될 저에서 큰 도움을 주신 권순우 책임님께도 감사드립니다.

이 글을 보지는 못하겠지만 맨 처음 들어와서 연구적으로나 생활습관을

보고 존경했던 정연누나와 방이 멀어 아쉬웠지만 매번 세심하게 알려주신 우람이형과 약간은 무서웠지만 친절하게 알려주신 원재형도 감사드립니다. 연구실에서 가장 든든했던 우진이형, 나랑 가장 많이 싸웠지만 연구적으로 도움을 가장 많이 받은 찬양이형, 생기원에서 실험으로 도움많은 준호형과 같이 아이디어 내주신 형림형님, 이런 감사인사하기에는 오글거리는 홍진, 취업에 큰 도움받고 있는 유미, 엘지과제로 고생많은 동준이, 뭘해도 잘하는 경문이, 졸업해 지금은 없지만 계속 연락하고 싶고 좋은 친구들인 재민, 정환, 수현이도 모두 감사합니다. 정말 열심히하고 같이 연구할때마다 선배지만 여러 도움을 많이 받고 같이 고생한 진흥이와 영어로 고생한 나에게 큰 도움이 되고 새벽에 말동무가 된 유러피언 찬미, 고생했던 재승이도 모두와 같이해서 좋았습니다. 쌍둥이 육아와 연구를 같이하는 대단한 서연누나, 워낙 똑똑한 성환이, 내가 술을 못해 많이는 친해지지 못한 서준, 정윤, 영민이, 그리고 너무 착한 건진, 회사일과 학업 병행하고 마찰실험에 도움 주신 지영누님과 혜진누나 모두 감사드리며 남은 학업 무사히 잘 마치길 바랍니다.

매번 감사하다고 말씀은 못드리지만 공부하는데 다른 걱정없이 나름 편하게 공부할 수 있게 해주신 우리 부모님께 학생 신분에 경제적 능력도 부족한 상태에서 결혼도 큰 걱정없이 하게 되었고 이렇게 무사히 박사학위도 잘 받았습니다. 워낙 무뚝뚝해서 속으로만 감사드렸지만 항상 감사하고 사랑합니다. 그리고 어렸을때는 정말 많이 싸웠지만 커서는 많이 의지한 우리누나, 항상 고생이 많은 매형, 우리집 귀염둥이 하진이도 사랑해요. 아직 학생신분의 사위로 말씀은 안 하셨지만 많은 걱정하셨을 장인 장모님 이쁜 딸

잘 키워주시고 결혼도 허락해주셔서 감사드립니다. 살갑게 매번 못해드려 정말 죄송하고 더 친근한 사위가 되도록 노력하겠습니다. 얼굴 보기 워낙 힘든 성주랑 이미 친동생 같은 현희도 가족이니깐 도움이나 필요한거 있으면 언제든 말해

마지막으로, 이렇게 편지로만 매번 표현해서 미안하지만 거의 대학원 시작부터 연애 시작해서 결혼할때도 많이 신경 못쓰고 신혼 초에도 연구한다고 거의 주말부부처럼 지내느라 너무 미안하고 고생 많았어. 말은 많이 안했지만 대학원 동안에 정말 많이 의지했고 도움도 많이 받았어. 그리고, 연구 외에는 신경 안쓰게 해려고 매번 부모님들께 잘해주고 새벽에 나간다고 아침밥도 챙겨주느라 너무너무 고마워. 남편 박사 만든다고 고생했어. 나에게는 최고의 행운인 당신 많이 사랑해 앞으로도 항상 행복하자.

이 기 정 드림